Summer 7-14-2017

Development of epitaxial strategies towards the growth of novel semiconductor saturable absorber mirrors (SESAMs) for passively mode-locked optically pumped Vertical-external-cavity surface-emitting lasers (VECSELs)

Sadhvikas J. Addamane
University of New Mexico - Main Campus

Sadhvikas J. Addamane
Candidate

Electrical & Computer Engineering
Department

This dissertation is approved, and it is acceptable in quality and form for publication:

Approved by the Dissertation Committee:

Dr. Ganesh Balakrishnan, Chairperson

Dr. Adam Hecht

Dr. Alexandre Laurain

Dr. Ashwani Kumar Sharma

Development of epitaxial strategies towards the growth of novel semiconductor saturable absorber mirrors (SESAMs) for passively mode-locked optically pumped Vertical-external-cavity surface-emitting lasers (VECSELs)

by

SADHVIKAS J. ADDAMANE

B.S in Electrical Engineering, The University of New Mexico, 2013

DISSERTATION

Submitted in Partial Fulfillment of the
Requirements for the Degree of

Doctor of Philosophy
Engineering

The University of New Mexico
Albuquerque, New Mexico

July 2017

DEDICATION

To my parents, Jayachandra and Kalpana, who've sacrificed a lot for me and continue to support me even when I keep letting them down.

ACKNOWLEDGEMENTS

I would like to thank my advisor, Dr. Ganesh Balakrishnan for his dedicated guidance and unwavering support. His ever-optimistic approach towards solving problems has made most of this work possible. I have not only benefited from his vast knowledge of crystal growth and semiconductor science, but have also learnt many life lessons from him.

I would also like to thank my other committee members, Dr. Adam Hecht, Dr. Alexandre Laurain and Dr. Ashwani Sharma for their time and their constructive inputs throughout the process.

Many thanks to Dr. Thomas Rotter for introducing me to the art and science of molecular beam epitaxy (MBE). On the same note, I would like to acknowledge Dr. Rotter, Dr. Ralph Dawson and Mr. Chris Hains for teaching me everything I know and for patiently answering all of my questions on MBE and VECSELs for the past few years. I would also like to thank Dr. Jerry Moloney's group at the University of Arizona, Tucson for graciously allowing me to use their labs for characterization of my devices. I would especially like to thank Dr. Alexandre Laurain and Mr. Caleb Baker who took the time to help me understand the intricate working principles of SESAMs and letting me use their experimental setups. To Dr. Darryl Shima, thank you for facilitating all the transmission electron microscopy (TEM) work for this thesis. I would also like to thank the rest of Gunny's group (past and present) and office-mates at CHTM: Pankaj Ahirwar, Steve Clarke, Emma Renteria, Ahmad Mansoori, Orlando Romero, Brianna Klein, Ted Schuler-Sandy, Lilian Casias, Andrew Aragon, Vinita Dahiya, Stephen Myers, Sen Mathews and Noel Dawson for passing on their expertise, helping me with various aspects of this work and for engaging discussions on pretty much everything.

I am also indebted to all of the support staff (front office, machine shop, IT support) at CHTM and the ECE graduate advisors (Elmyra and Yvone) who have helped me navigate this process.

Last but not the least, I would like to thank my parents, my sister Sankalpa, my brother Isaac Edwards, my wife Karissa and her family for their unconditional love and support. I would also like to express my gratitude towards all of my friends and family who have helped me get to this point in many ways.

Development of epitaxial strategies towards the growth of novel semiconductor saturable absorber mirrors (SESAMs) for passively mode-locked optically pumped vertical external cavity surface emitting lasers (VECSELs)

SADHVIKAS J. ADDAMANE

B.S in Electrical Engineering, The University of New Mexico, 2013

PhD, Electrical Engineering, The University of New Mexico, 2017

Abstract

Mode-locked VECSEL systems using SESAMs are a relatively less complex and cost-effective alternative to state-of-the-art ultrafast lasers based on solid-state or fiber lasers. This system has seen considerable progress in device performance in terms of pulse width and peak power in the recent years. However, these device characteristics still have to be improved greatly and this system has to become more reliable to become commercially relevant. The realization of femtosecond pulses over long periods of time is non-trivial due to the high sensitivity of SESAM characteristics to minor drifts in growth or cavity conditions. This work focuses on developing novel epitaxial strategies for the growth and optimization of SESAMs towards obtaining sub-100fs pulse durations and increasing the damage threshold for these devices.

As part of this work, we have described in detail a comprehensive growth strategy for InGaAs quantum well (QW) -based SESAMs that are capable of supporting femtosecond pulses. These SESAMs are characterized for reflectivity, temperature-dependence, dispersion control and lifetimes. Through this process, we were able to achieve pulse durations as short as 128fs from InGaAs QW-based SESAMs. This is one of the shortest pulse durations reported to date from mode-locked VECSEL systems. However, it is found that the QW-based SESAMs exhibit poor temporal performance. As an alternative to this system, the latter part of the thesis explores the possibility of using InAs/GaAs submonolayer (SML) quantum dots (QDots) as the saturable absorber for SESAMs around 1μm. Along with higher output power, we were able to realize mode-locking of VECSELs using SML QDot-based SESAMs with pulses as short as 185 fs. To the best of our knowledge, this is the first time SML QDots are used as saturable absorbers for SESAMs in the femtosecond regime. We also found that QDot-based SESAMs have substantially longer lifetimes compared to QW-based SESAMs.

Table of Contents

List of figures

List of tables

Chapter 1 : Introduction to ultrafast lasers

Ultrafast lasers – lasers generating short pulses with pulse durations in the pico and femtosecond ranges – have progressed rapidly in the recent years and have made significant impact in the fields of both fundamental science and industrial research [1,2]. Their impact on scientific research is reflected in the fact that the field of ultrafast lasers has enabled two Nobel-prize awarded research topics including femtochemistry [3] and optical frequency combs [4,5] since 1999. Here, we have highlighted some of the numerous applications of ultrafast lasers classified based on four of their key features [1]:

a) **Ultra-short pulse duration**: This is probably the most significant feature of ultrafast lasers. Ultra-short pulse durations enable high-resolution measurements in the time domain. This allows for improved temporal resolution in observation of high-speed phenomena such as chemical reactions (as shown in figure 1.1 below) [2,6], carrier relaxation in semiconductors [7] and electro-optical sampling of high-speed electronics [8,9].

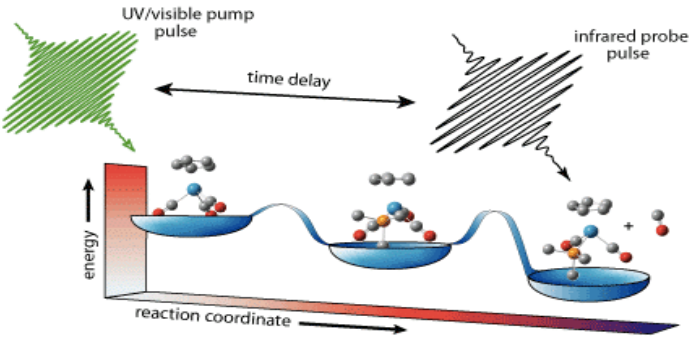

Figure 1.1 Femtosecond spectroscopy to access fast chemical dynamics (taken from [10])

b) **High pulse repetition rate**: Lasers with high repetition rates (in the multi-gigahertz range) are essential components in optical interconnects [11], high-capacity telecommunication systems [12] and clocks [13]. In the field of telecommunication, development of a mode-locked laser with a high repetition rate and a tunable emission wavelength around 1.55μm is significant to keep up with the increase in data transmission rates. In the lower wavelength range (around 1μm), sources with high average power and high repetition rates (upto 100GHz) can be used for optical clocks in integrated circuits.

c) **Broad spectrum**: Pulses with high peak powers focused on nonlinear fibers create a broad optical spectrum, which in turn supports good spatial resolution for techniques like Optical Coherence Tomography (OCT- figure 1.2) [14,15]. OCT exploits the fact that mode-locked lasers offer considerably higher average output power when compared to other broadband sources and a broad spatial resolution of a few microns. Pulse trains produced by mode-locked lasers also provide a comb-shaped optical spectrum which can be used as stable multi-wavelength sources [16], all-optical atomic clocks [17] and in highly non-linear processes such as photoionization [18].

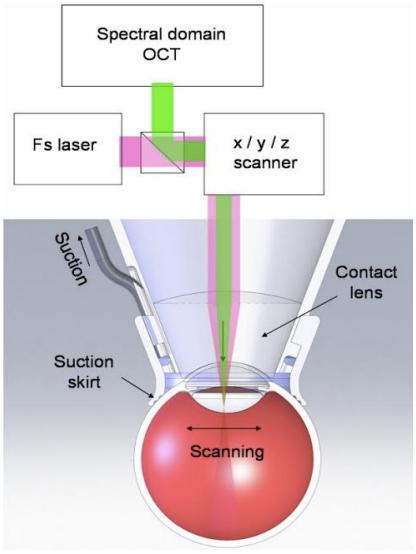

Figure 1.2 OCT used in Cataract surgery [taken from 19]

d) **High peak power:** The enhancement in peak power compared to average power in ultrafast lasers is a consequence of the laser energy being compressed into ultra-short pulse durations. Therefore, mode-locked lasers are capable of producing a record combination of short pulse, high peak power and high average power (Pulse energy > 1μJ at 30MHz repetition rate [20,21]). These high peak powers can be used in a variety of applications, from multi-photon absorption technologies [22] to processing microstructures in solid targets without a corresponding increase in temperature [23] (non-thermal ablation). In the medical field, these pulses can be used for increased precision in surgical cutting especially for corneal [24] and brain tumor surgeries [25]. The threshold for an optical breakdown decreases with the pulse duration and so, when used for surgical procedures, these mode-locked lasers reduce secondary damage effects in tissues [26].

It is to be noted that the description above covers only a few of the numerous applications of ultrafast lasers.

1.1 Ultrafast semiconductor lasers

At present, applications requiring stable ultra-short pulses are dominated by Kerr-lens mode-locked Ti:sapphire laser and directly diode-pumped solid-state lasers (DPSSL) mode-locked using SESAMs [27,28].These two systems have enabled the realization of high average powers [29,30], pulse energies [20,21] and repetition rates [31] with pulses in the femtosecond range. However, despite the high-performance of solid state lasers, they are expensive and invariably have complex designs. On the other hand, semiconductor lasers are cost-effective for mass production and offer a high level of integration to realize compact devices. Furthermore, the characteristics of semiconductor lasers can be easily tailored using band gap engineering. With regard to mode-locking, semiconductor lasers can be classified into edge-emitters and semiconductor disk lasers (SDLs).

Edge-emitting mode-locked lasers typically have the same epitaxial layer acting as both the gain and the saturable absorber. While the gain region is essentially a forward-biased p-i-n diode, the absorber section is reverse-biased. This takes away the ability to optimize both sections independent of each other. On the other hand, it also makes this system extremely compact and enables their direct integration into optical circuits. To date, edge-emitting QDot lasers at 1550nm have been able to achieve pulse durations of 312 fs with a 92 GHz repetition rate and 13.2 mW of average power [32]. However, in terms of high average power, most mode-locked edge-emitters have been able to operate

in the picosecond pulse duration range with only ~250mW average power [33,34]. In order to increase the output power of mode-locked edge emitters, external elements [35] or pulse compression have been employed and this increases the complexity of these systems. Moreover, it is not trivial to increase the output power levels in this system. Edge emitters have a long interaction length and this leads to an increase the noise levels and limits mode-locking stability. It is also important to note that edge-emitters are prone to end facet damage at high peak powers in the watt-levels [36]. Edge-emitting semiconductor lasers also inherently have strongly asymmetric beam profiles which has been typically corrected using lenses.

SDLs or vertical-external-cavity surface-emitting lasers (VECSELs) are the ideal choice for mode-locking applications as they merge the positive aspects of DPSSLs and edge-emitting semiconductor lasers. Like edge-emitter semiconductor lasers, the design can easily be optimized using band gap engineering. However, unlike edge-emitters, VECSELs have a short cavity interaction length, which reduces the noise level and makes it easier to achieve higher output powers with a symmetric circular beam profile. On the other hand, power scaling in VECSELs can be achieved by simply increasing the mode size (very similar to DPSSLs). Also, like DPSSLs, a VECSEL chip coupled with a SESAM can be used to achieve a self-starting, stable mode-locking state. Moreover, VECSELs open up the possibility of integrating the SESAM within the gain region (explained in chapter 5) which is referred to as a mode-locked-integrated external cavity surface emitting laser. (MIXSEL)

1.2 Motivation and organization of thesis

The first demonstration of a mode-locked VECSEL was published in 2000 by Hoogland et. al [37]. Since then, there has been considerable progress made in all characteristics of a mode-locked VECSEL system – pulse duration (107 fs), average power (6.4W) and peak power (4.35kW) [38-40]. However, there is still a lot of work to be done in order to make mode-locked VECSEL systems competitive with mode-locked DPSSLs. For instance, Kerr-lens mode-locked Ti:sapphire lasers can generate pulses as short as 5 fs and peak powers of close to 80W. [29,41]. In addition, SESAM-modelocked VECSEL systems also suffer degradation of output power over time and this needs to be investigated and alleviated in order to achieve stable mode-locking over long periods of time [42]. Therefore, this thesis focuses on optimizing SESAM characteristics for a mode-locked VECSEL system using a comprehensive epitaxial strategy mainly focusing on shortening pulse durations and increasing the lifetime of SESAMs.

This thesis is organized in the following way:

Chapter 2 reviews fundamental design aspects for a VECSEL and a SESAM in a mode-locked system. It discusses the design considerations for the gain chip and explains the exact gain structure used for this thesis. We also explore designing the different components of a SESAM and describe the measurement of macroscopic properties of a SESAM. Finally, we describe the different cavity designs used to characterize the SESAMs.

Chapter 3 focuses on obtaining high-performance InGaAs QW-based SESAMs with sub-100 fs pulse durations. This includes design considerations, process flow used for optimization of devices, various characterizations for the SESAM device and potential drawbacks.

Chapter 4 elaborates on the drawbacks of the InGaAs QW-based SESAMS, especially focusing on their damage threshold. Different design parameters and their effect on the degradation of SESAMs is studied in detail.

Chapter 5 explores the use of InAs submonolayer (SML) QDot-based SESAMs as a solution to the issues faced with the QW-based SESAMs. All the SESAM macroscopic properties are compared between the QW and the SML QDot-based SESAMs including SESAM lifetime.

Chapter 6 discusses conclusions and future work.

References:

[1] Keller, Ursula. "Recent developments in compact ultrafast lasers." *Nature* 424, no. 6950 (2003): 831-838.

[2] Okhotnikov, Oleg G., ed. *Semiconductor disk lasers: physics and technology*. John Wiley & Sons, 2010.

[3] Zewail, Ahmed H. "Laser femtochemistry." *Science* 242, no. 4886 (1988): 1645.

[4] Jones, David J., Scott A. Diddams, Jinendra K. Ranka, Andrew Stentz, Robert S. Windeler, John L. Hall, and Steven T. Cundiff. "Carrier-envelope phase control of femtosecond mode-locked lasers and direct optical frequency synthesis." *Science* 288, no. 5466 (2000): 635-639.

[5] Apolonski, A., A. Poppe, G. Tempea, Ch Spielmann, Th Udem, R. H. T. W. Holzwarth, Theodor W. Hänsch, and Ferenc Krausz. "Controlling the phase evolution of few-cycle light pulses." *Physical Review Letters* 85, no. 4 (2000): 740.

[6] Zewail, Ahmed H. "Femtochemistry: Atomic-scale dynamics of the chemical bond." *The Journal of Physical Chemistry A* 104, no. 24 (2000): 5660-5694.

[7] Shah, Jagdeep. *Ultrafast spectroscopy of semiconductors and semiconductor nanostructures*. Vol. 115. Springer Science & Business Media, 2013.

[8] Valdmanis, J., and G. Mourou. "Subpicosecond electrooptic sampling: Principles and applications." *IEEE Journal of Quantum Electronics* 22, no. 1 (1986): 69-78.

[9] Weingarten, Kurt J., M. J. W. Rodwel, and David M. Bloom. "Picosecond optical sampling of GaAs integrated circuits." *IEEE Journal of Quantum electronics* 24, no. 2 (1988): 198-220.

[10] Harris, Charles. "Ultrafast vibrational spectroscopy on chemical reaction dynamics in liquids". the C.B. Harris group. http://www.cchem.berkeley.edu/cbhgrp/research.html (06/10/2017)

[11] Miller, David AB. "Optical interconnects to silicon." *IEEE Journal of Selected Topics in Quantum Electronics* 6, no. 6 (2000): 1312-1317.

[12] Mollenauer, L. F., P. V. Mamyshev, J. Gripp, M. J. Neubelt, N. Mamysheva, Lars Grüner-Nielsen, and Torben Veng. "Demonstration of massive wavelength-division multiplexing over transoceanic distances by use of dispersion-managed solitons." *Optics letters* 25, no. 10 (2000): 704-706.

[13] Krishnamoorthy, Ashok V., and David AB Miller. "Scaling optoelectronic-VLSI circuits into the 21st century: A technology roadmap." *IEEE Journal of selected topics in quantum electronics* 2, no. 1 (1996): 55-76.

[14] Huang, David, Eric A. Swanson, Charles P. Lin, Joel S. Schuman, William G. Stinson, Warren Chang, Michael R. Hee et al. "Optical coherence tomography." *Science (New York, NY)* 254, no. 5035 (1991): 1178.

[15] Fujimoto, James G. "Optical coherence tomography." *Comptes Rendus de l'Académie des Sciences-Series IV-Physics* 2, no. 8 (2001): 1099-1111.

[16] Boivin, L., M. Wegmueller, M. C. Nuss, and W. H. Knox. "110 Channels x 2.35 Gb/s from a single femtosecond laser." *IEEE Photonics Technology Letters* 11, no. 4 (1999): 466-468.

[17] Udem, Th, Ronald Holzwarth, and Theodor W. Hänsch. "Optical frequency metrology." *Nature* 416, no. 6877 (2002): 233-237.

[18] Paulus, G. G., F. Grasbon, H. Walther, P. Villoresi, M. Nisoli, S. Stagira, E. Priori, and S. De Silvestri. "Absolute-phase phenomena in photoionization with few-cycle laser pulses." *Nature* 414, no. 6860 (2001): 182-184.

[19] Medical physics (Science/AAAS)

[20] Marchese, S. V., C. R. E. Baer, A. G. Engqvist, S. Hashimoto, D. J. H. C. Maas, M. Golling, T. Südmeyer, and U. Keller. "Femtosecond thin disk laser oscillator with pulse energy beyond the 10-microjoule level." *Optics express* 16, no. 9 (2008): 6397-6407.

[21] Neuhaus, Joerg, Dominik Bauer, Jing Zhang, Alexander Killi, Jochen Kleinbauer, Malte Kumkar, Sascha Weiler, Mircea Guina, Dirk H. Sutter, and Thomas Dekorsy. "Subpicosecond thin-disk laser oscillator with pulse energies of up to 25.9 microjoules by use of an active multipass geometry." *Optics express* 16, no. 25 (2008): 20530-20539.

[22] Rafailov, Edik U., ed. *The physics and engineering of compact quantum dot-based lasers for biophotonics*. John Wiley & Sons, 2013.

[23] Liu, X., D. Du, and G. Mourou. "Laser ablation and micromachining with ultrashort laser pulses." *IEEE journal of quantum electronics* 33, no. 10 (1997): 1706-1716.

[24] Juhasz, Tibor, Frieder H. Loesel, Ron M. Kurtz, Christopher Horvath, Josef F. Bille, and Gerard Mourou. "Corneal refractive surgery with femtosecond lasers." *IEEE Journal of Selected Topics in Quantum Electronics* 5, no. 4 (1999): 902-910.

[25] Hammer, Daniel X., Robert J. Thomas, Gary D. Noojin, Benjamin A. Rockwell, Paul K. Kennedy, and William P. Roach. "Experimental investigation of ultrashort pulse laser-

induced breakdown thresholds in aqueous media." *IEEE Journal of quantum electronics* 32, no. 4 (1996): 670-678.

[26] Loesel, Frieder H., Markolf H. Niemz, J. F. Bille, and T. Juhasz. "Laser-induced optical breakdown on hard and soft tissues and its dependence on the pulse duration: experiment and model." *IEEE Journal of Quantum Electronics* 32, no. 10 (1996): 1717-1722.

[27] Keller, Ursula, Kurt J. Weingarten, Franz X. Kartner, Daniel Kopf, Bernd Braun, Isabella D. Jung, Regula Fluck, Clements Honninger, Nicolai Matuschek, and J. Aus Der Au. "Semiconductor saturable absorber mirrors (SESAM's) for femtosecond to nanosecond pulse generation in solid-state lasers." *IEEE Journal of selected topics in QUANTUM ELECTRONICS* 2, no. 3 (1996): 435-453.

[28] Keller, U., D. A. B. Miller, G. D. Boyd, T. H. Chiu, J. F. Ferguson, and M. T. Asom. "Solid-state low-loss intracavity saturable absorber for Nd: YLF lasers: an antiresonant semiconductor Fabry–Perot saturable absorber." *Optics letters* 17, no. 7 (1992): 505-507.

[29] Innerhofer, E., T. Südmeyer, F. Brunner, R. Häring, A. Aschwanden, R. Paschotta, C. Hönninger, M. Kumkar, and U. Keller. "60-W average power in 810-fs pulses from a thin-disk Yb: YAG laser." *Optics letters* 28, no. 5 (2003): 367-369.

[30] Brunner, Felix, Edith Innerhofer, Sergio V. Marchese, Thomas Südmeyer, Rüdiger Paschotta, Takeshi Usami, Hiromasa Ito et al. "Powerful red-green-blue laser source pumped with a mode-locked thin disk laser." *Optics letters* 29, no. 16 (2004): 1921-1923.

[31] Hartl, Ingmar, H. A. McKay, R. Thapa, B. K. Thomas, A. Ruehl, L. Dong, and M. E. Fermann. "Fully stabilized GHz Yb-fiber laser frequency comb." In *Advanced Solid-State Photonics*, p. MF9. Optical Society of America, 2009.

[32] Lu, Z. G., J. R. Liu, S. Raymond, P. J. Poole, P. J. Barrios, and Daniel Poitras. "312-fs pulse generation from a passive C-band InAs/InP quantum dot mode-locked laser." *Optics Express* 16, no. 14 (2008): 10835-10840.

[33] Plant, Jason J., Juliet T. Gopinath, Bien Chann, Daniel J. Ripin, Robin K. Huang, and Paul W. Juodawlkis. "250 mW, 1.5 μm monolithic passively mode-locked slab-coupled optical waveguide laser." *Optics letters* 31, no. 2 (2006): 223-225.

[34] Rosales, R., V. P. Kalosha, K. Posilović, M. J. Miah, D. Bimberg, J. Pohl, and M. Weyers. "High brightness photonic band crystal semiconductor lasers in the passive mode locking regime." *Applied Physics Letters* 105, no. 16 (2014): 161101.

[35] Balzer, J. C., T. Schlauch, A. Klehr, G. Erbert, G. Tränkle, and M. R. Hofmann. "High peak power pulses from dispersion optimised modelocked semiconductor laser." *Electronics Letters* 49, no. 13 (2013): 838-839.

[36] Puchert, R., A. Bärwolff, U. Menzel, A. Lau, M. Voss, and T. Elsaesser. "Facet and bulk heating of GaAs/AlGaAs high-power laser arrays studied in spatially resolved emission and micro-Raman experiments." *Journal of applied physics* 80, no. 10 (1996): 5559-5563.

[37] Hoogland, S., S. Dhanjal, A. C. Tropper, J. S. Roberts, R. Haring, R. Paschotta, F. Morier-Genoud, and U. Keller. "Passively mode-locked diode-pumped surface-emitting semiconductor laser." *IEEE Photonics Technology Letters* 12, no. 9 (2000): 1135-1137.

[38] Klopp, P., U. Griebner, M. Zorn, and M. Weyers. "Pulse repetition rate up to 92 GHz or pulse duration shorter than 110 fs from a mode-locked semiconductor disk laser." *Applied Physics Letters* 98, no. 7 (2011): 071103.

[39] Rudin, B., V. J. Wittwer, D. J. H. C. Maas, M. Hoffmann, O. D. Sieber, Y. Barbarin, M. Golling, T. Südmeyer, and U. Keller. "High-power MIXSEL: an integrated ultrafast semiconductor laser with 6.4 W average power." *Optics express* 18, no. 26 (2010): 27582-27588.

[40] Wilcox, Keith G., Anne C. Tropper, Harvey E. Beere, David A. Ritchie, Bernardette Kunert, Bernd Heinen, and Wolfgang Stolz. "4.35 kW peak power femtosecond pulse mode-locked VECSEL for supercontinuum generation." *Optics express* 21, no. 2 (2013): 1599-1605.

[41] Sutter, Dirk H., Günter Steinmeyer, Lukas Gallmann, Nicolai Matuschek, François Morier-Genoud, Ursula Keller, V. Scheuer, Gregor Angelow, and Theo Tschudi. "Semiconductor saturable-absorber mirror–assisted Kerr-lens mode-locked Ti: sapphire laser producing pulses in the two-cycle regime." *Optics letters* 24, no. 9 (1999): 631-633.

Chapter 2 : Design considerations for mode-locked VECSELs

2.1 Vertical-external-cavity surface emitting laser

Semiconductor lasers can broadly be classified into two categories based on the orientation from which emission of light occurs: edge-emitting and surface-emitting lasers. In the case of edge-emitters, the cavity where the light is confined is in the plane of the semiconductor and the laser emission occurs from the edge of the chip with the cleaved facets used as mirrors. On the other hand, in surface-emitting lasers the laser emission occurs in a plane perpendicular to the semiconductor wafer. This difference between the two classes of semiconductor lasers is shown in Figure 2.1 below.

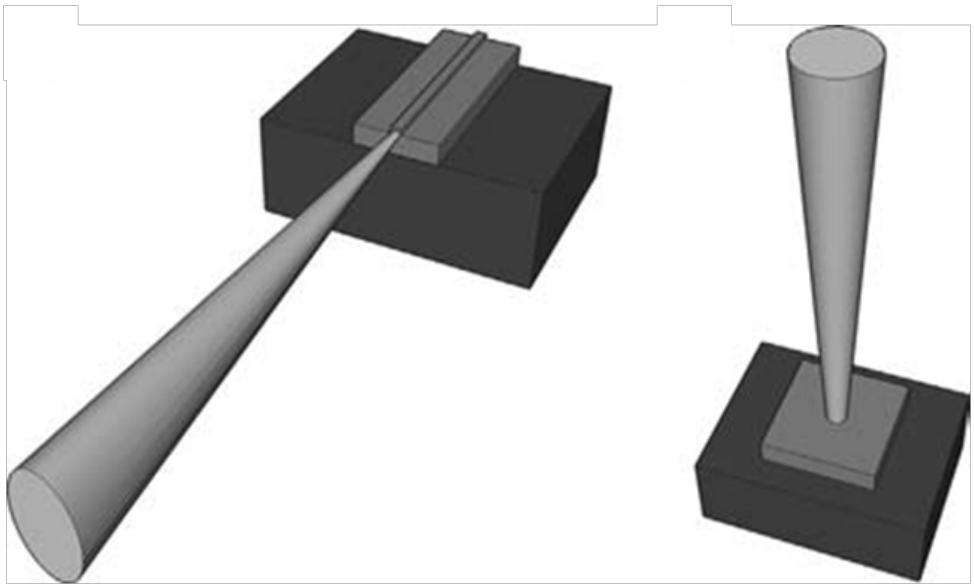

(a) (b)

Figure 2.1: Two categories of semiconductor lasers : (a) Edge-emitting laser (taken from [1])

In edge-emitting lasers, a near TEM_{00} mode can only be realized at low output power levels (<1W). [2,3] Surface emitting lasers are great candidates for realizing lasers with both high optical power and a good beam quality. Figure 2.2 below shows a schematic of a vertical-cavity surface emitting laser (VCSEL). VCSELs are comprised of a gain region (typically QDots or QWs) sandwiched between top and bottom Distributed Bragg Reflectors (DBRs). The DBRs (design considerations explained in later section) are formed by alternating two layers with different refractive indices to obtain reflectivities of >99.9% and are doped for electrical injection. The laser emission propagates normal to the semiconductor surface from the top DBR which has lower reflectivity (~96-99%). Although VCSELs exhibit nearly circular TEM_{00} output mode, the output power is limited to tens of mWs as a virtue of their limited lateral dimension. [4]

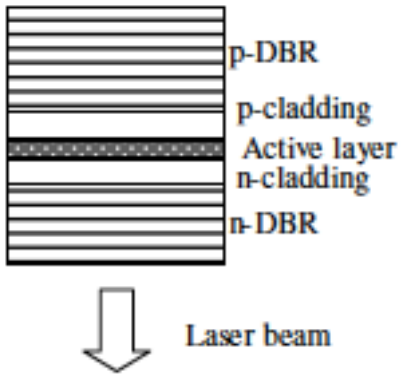

Figure 2.2: Schematic of a VCSEL (taken from [5])

In a VCSEL, if the top DBR is replaced by an external mirror, this formulates a VECSEL. [6] Therefore, a VECSEL is essentially a semiconductor laser that comprises a highly reflective mirror and a gain region with the cavity being completed by an external coupler. Figure 2.3 shows a typical linear VECSEL cavity. The properties of the external

mirror (radius of curvature and distance from semiconductor surface) play a significant role in controlling the lateral mode size. This makes it fairly straightforward to realize high output powers along with a nearly circular beam output by optimizing the cavity dimensions and having a similar pump spot size. To obtain uniform pumping in large area, optical pumping is best suited. This also makes the power scaling in VECSELs more straightforward by simply increasing the diameter of the pump spot while keeping the pump density constant. In addition to the ease in control over mode size, the external cavity design allows for the integration of intracavity elements such as frequency doubling crystals and SESAMs for passive mode-locking. This is particularly critical to the work done in this thesis.

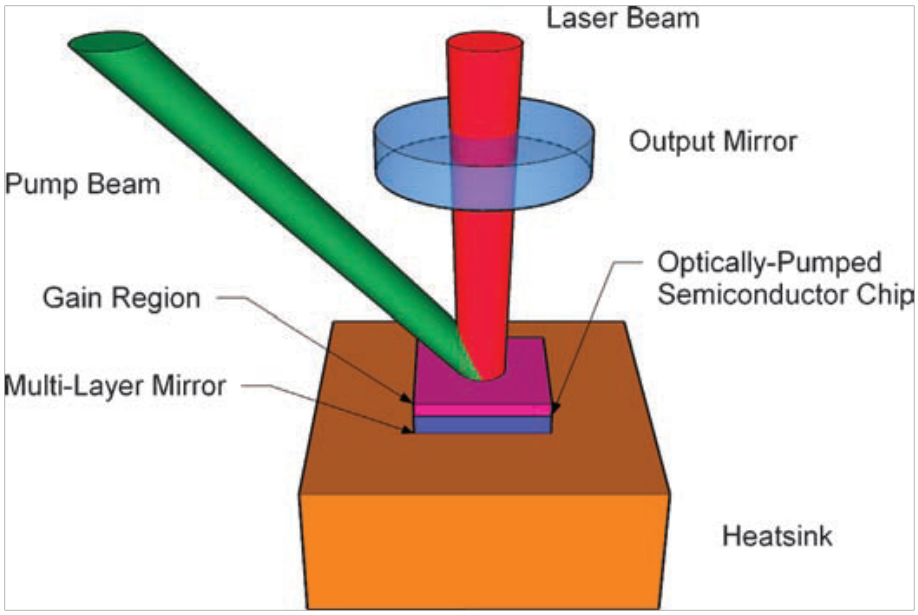

Figure 2.3: A typical optically-pumped VECSEL cavity

2.2 Design of VECSEL structure

A typical semiconductor VECSEL structure is shown in figure 2.4 below. It is comprised of a DBR mirror, a gain section (active media embedded within barriers) and anti-reflection (AR) coating to optimize pump absorption and dispersion control. This structure coupled with an external mirror completes the laser cavity. Figure 2.5 shows a band gap structure of a typical QW-based VECSEL with the specific layers in the gain section and explains the operating principle. Assuming optical pumping, the pump absorbing barriers - which confine the QWs - absorb the incident pump photons with higher photon energy. The carriers formed here diffuse into the QWs (which have a smaller band gap) and result in photons emitted with lower energy (corresponding to the band gap of the QW). The window layer offers better carrier confinement and prevents the carriers from being diffused and recombined non-radiatively at the air-semiconductor interface. The following section explains the design considerations for the gain region in a VECSEL. The design considerations for the DBR, which is also a part of the SESAM, is discussed later in this chapter.

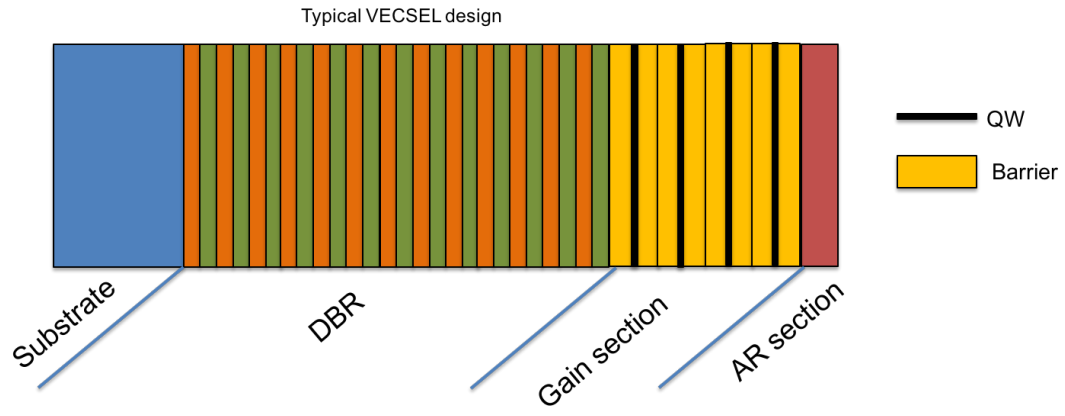

Figure 2.4: Schematic of a typical VECSEL semiconductor structure

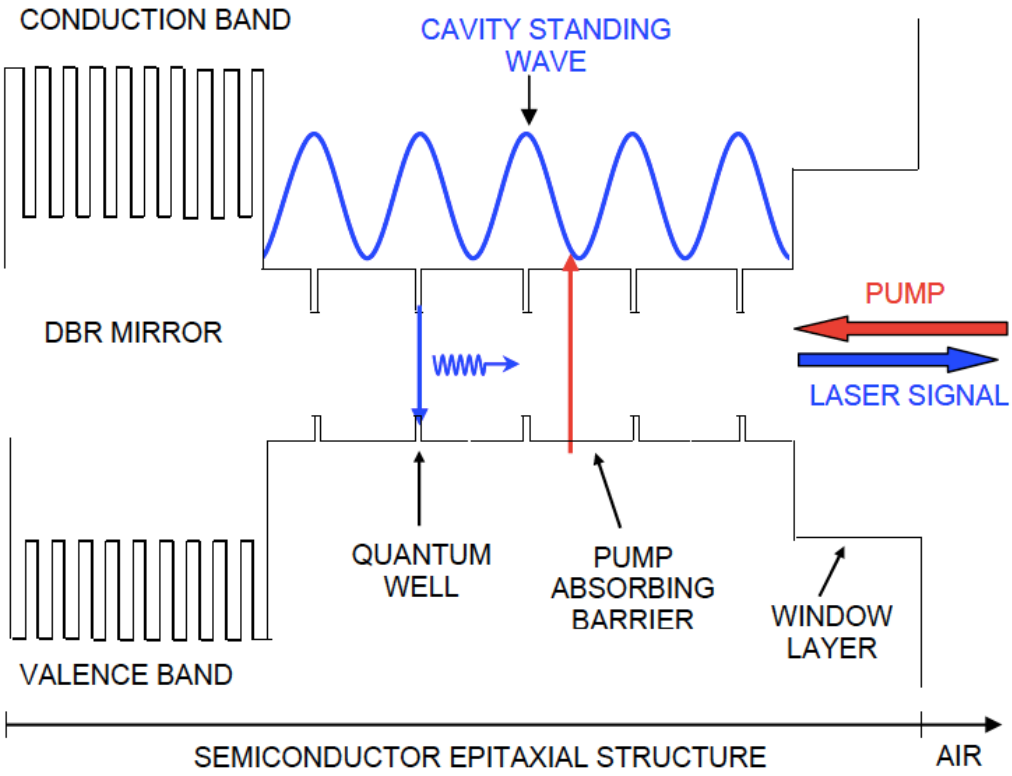

Figure 2.5: Schematic band-gap diagram for an optically pumped VECSEL chip showing its operating principles. (taken from [1])

There are two different configurations in which a VECSEL can be assembled. In a "top-emitter" configuration as shown in figure 2.6(a), the DBR is grown first on the substrate followed by the active region, onto which the heat spreader is capillary bonded. Therefore, as the figure shows, the heat spreader in this configuration is placed inside the optical cavity and therefore it has to be of optical grade and has to be capillary bonded. However, the interaction of the emission with intra-cavity heat spreaders introduces losses into the system and limits the performance of these lasers. The highest power CW VECSELs based on InGaAs QWs using a top-emitting geometry is ~ 20 Watts CW [7]. On the other hand, in the "bottom-emitter" configuration, the active region is grown first on the substrate

and is followed by the growth of the DBR as shown in figure 2.6(b) below. This puts the heat spreader outside the optical cavity and therefore, there is no need for a complex bonding process and it could simply be soldered to the top of the DBR. However, a requirement of such an approach is that the substrate has to be removed post-growth with no etch damage to the active region. Thus only materials with very high etch contrast and consequently excellent etch stop layers can make use of such an approach [8]. In the case of VECSEL structures used in this study (InGaAs QW VECSELs grown on GaAs) such an etch stop layer exists and thus in the bottom emitting geometry, the same gain medium allows for the scale of power by almost an order of magnitude compared to the top-emitter. This has been evidenced by the demonstration of a 106-Watt CW VECSEL by Stolz et al [9].

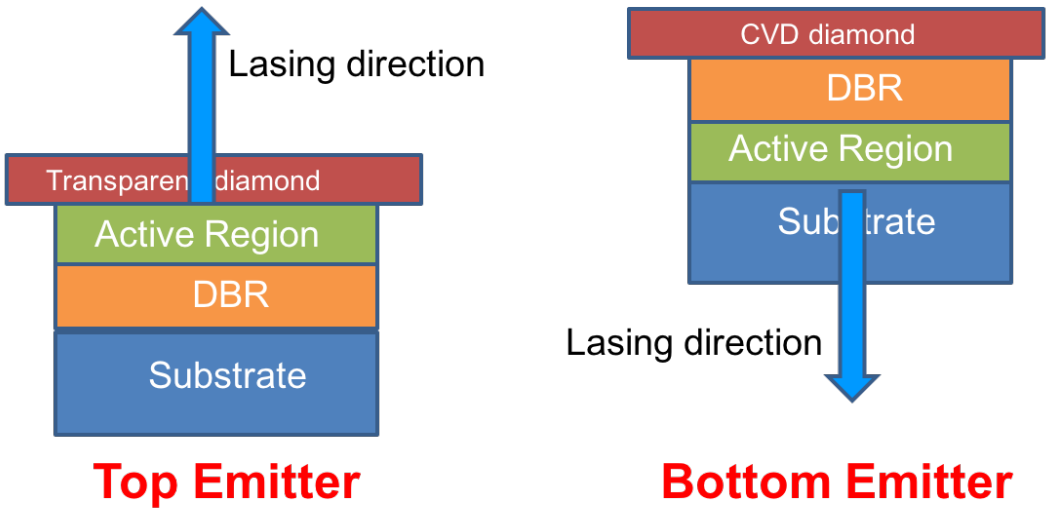

(a) (b)

Figure 2.6: Two configurations in which a VECSEL can be formulated: Top emitter (a) and Bottom emitter (b). The lasing direction and the placement of the heat spreader differentiates the two configurations.

2.2.1 Design of VECSEL gain region

The design of the gain region is crucial to the lasing characteristics and the formation of ultra-short pulses. The lasing threshold condition for a VESCEL requires that the intracavity optical field is duplicated in one round-trip inside the cavity:

$$R_{DBR}R_{OC}T_{loss}e^{(2\Gamma_z g_{th}N_w L_w)} = 1 \qquad (2.1)$$

where,

R_{DBR} & R_{OC} are the reflectivities of the DBR and the output coupler, respectively, T_{loss} corresponds to the transmission factor due to round-trip cavity loss, g_{th} is the threshold cavity gain, N_w and L_w are the number and length of the quantum wells, Γ_z is the longitudinal confinement factor.

The number of quantum wells (N_w) determines the total gain of the active region. Since L_w is on the order of ~8-12nm, the gain to an optical wave propagating in a VECSEL cavity normal to the plane of the quantum wells is small. Therefore, more than one QW is required to obtain enough gain for lasing. The longitudinal confinement factor Γ_z is a measure of the overlap between the standing optical wave in the cavity and quantum well placement. As shown in figure 2.5 in the previous section explaining VECSEL operating principles, typically a QW (or any active media) is placed at an antinode of the standing wave to achieve maximum gain (i.e. maximize Γ_z). This configuration leads to a strong coupling between the quantum confined carriers and the intracavity standing wave in the active region and is called the Resonant Periodic Gain (RPG) arrangement [10,11]. It is

important to note that multiple QWs could be placed at the same antinode. Along with the placement of the QW, it is also significant to align the air-semiconductor interface with the standing electric field. This determines if the structure is in resonant or anti-resonant configuration. Along with other benefits such as high selective gain and relative immunity to cavity losses, the resonant structure is better suited for integration of intra-cavity elements such as SESAMs. This thesis primarily focuses on improving the performance of a mode-locked VECSEL system by exploring novel epitaxial strategies for the growth of SESAMs. A standard VECSEL structure (described below) is used and is not optimized as part of this study. Therefore, an in-depth discussion on the growth optimization of VECSELs in general is not included here.

2.3 Description of VECSEL structure used for study

The designed emission wavelength used for the study is 1030nm. As mentioned above, the major building blocks in a VECSEL structure (refer to schematic in figure 2.4) are the DBR, the gain region and the AR coating. The DBR section of the VECSEL structure used for this study consists of a hybrid metal-semiconductor mirror. The semiconductor part of the mirror comprises of 12 pairs of AlAs/GaAs 1/4 λ layers. The rest of the reflectivity needed is obtained by a pure gold reflector with the procedure followed in [12]. The use of a hybrid mirror is advantageous as it provides high reflectivity at both the pumping and the lasing wavelength and therefore helps with recycling the pump without having a separate DBR [10]. With the integration of the metal DBR, we also need fewer AlAs/GaAs pairs (12

instead of 23 or 30) in the semiconductor part of the DBR to obtain the reflectivity needed. In addition, it also offers lower thermal impedance and a broader bandwidth [13].

The active region consists of 12 layers of strain-compensated InGaAs QWs placed non-uniformly at different antinodes of the standing electric field as shown in figure 2.7[14]. The $In_xGa_{1-x}As$ composition is adjusted so that the emission wavelength is lined up at ~1030nm. Based on Photoluminescence(PL) results, this composition turns out to be ~ $In_{0.19}Ga_{0.81}As$. The QWs are pumped through GaAsP barriers with a 808nm fiber-coupled pump diode. This non-uniform distribution of QWs is critical to the system being able to support ultra-short pulses. It leads to a flat field intensity enhancement spectrum which, in turn gives a broader modal gain and increases the saturation fluence for the gain region. The semiconductor structure is coated with a bi-layer dielectric coating of Ta_2O_5/SiO_2 with thicknesses optimized to obtain a flat group delay dispersion (GDD). The significance of GDD to being able to obtain shorter pulses is discussed later in this chapter along with SESAM properties.

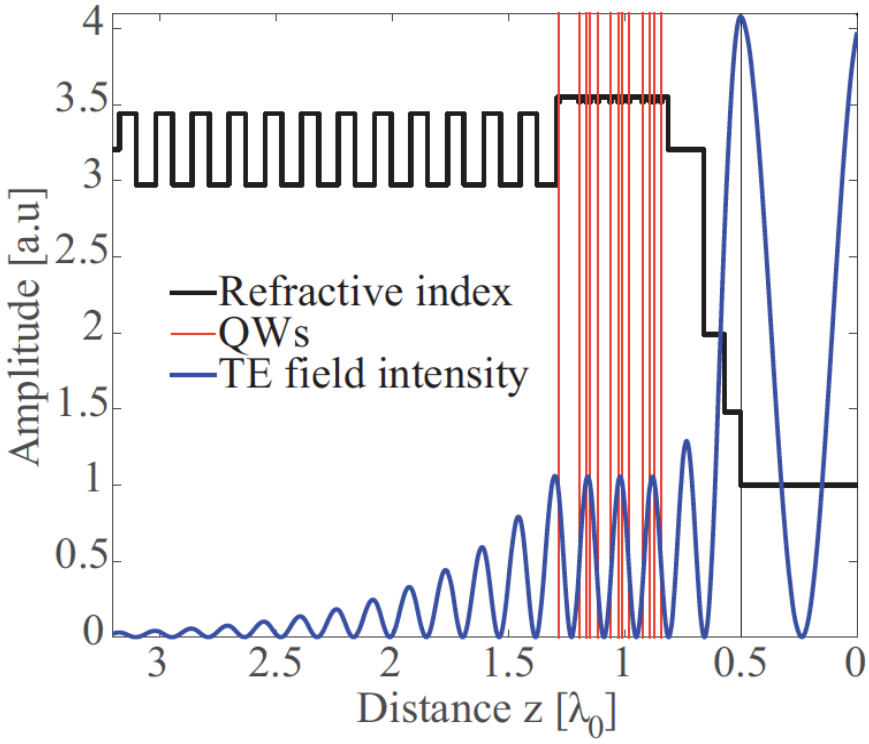

Figure 2.7: Design of the VECSEL structure used in this thesis [14]

For better thermal management, the structure discussed in this study (Figure 2.7 above) is grown as a bottom-emitter and is bonded to diamond [15]. The VECSEL structures described in this study are grown at the Phillips Universitat in Marburg, Germany. It is to be noted that the VECSEL structures described in this study are not grown or characterized as part of this study. They are, however, used in conjunction with the SESAMs grown for this thesis in a mode-locked cavity to characterize properties of the SESAM and the mode-locked system in general.

2.4 Design considerations for SESAMs

A typical SESAM design consists of one or more absorber layers (bulk, QW or QDot) grown on top of a highly reflective Distributed Bragg Reflector (DBR) mirror. It also includes a spacer layer between the DBR and the absorber and a cap on top of the absorber (as shown in figure 2.8).

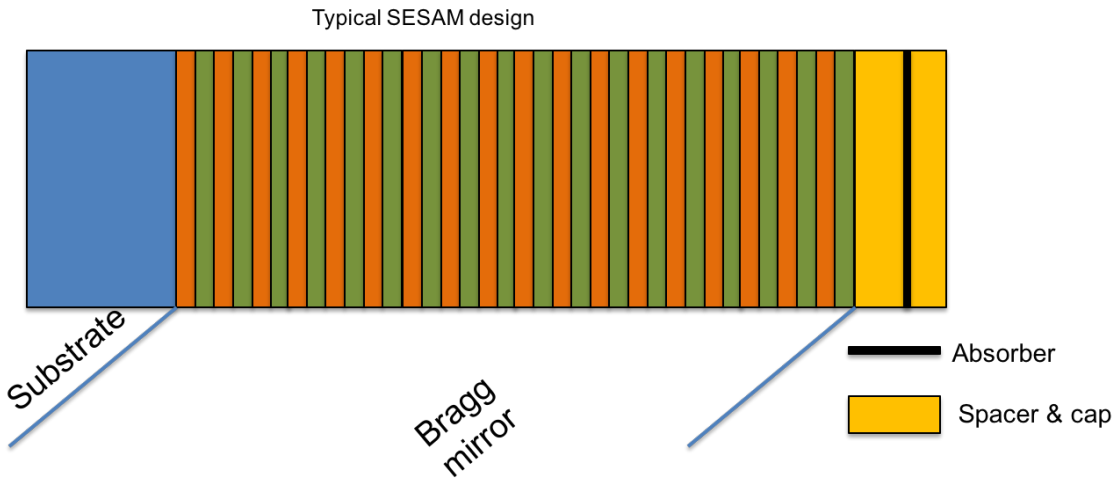

Figure 2.8: Schematic illustrating a typical SESAM design consisting of the Bragg mirror and the absorber.

2.4.1 Design of DBR region (for VECSELs and SESAMs)

A DBR mirror is composed of alternating high and low index layers that are each grown in a way that their thicknesses are equal to quarter of the design wavelength. This causes the Fresnel reflections from each interface of the two constituting materials to interfere constructively leading to a high reflectivity at the design wavelength. The width of the DBR stopband and the magnitude of reflectivity are determined by the contrast in the

refractive indices of the two constituting materials. The reflectivity intensity (R) and frequency bandwidth (Δf) can be estimated using [16] :

$$R = \left[\frac{(n_2{}^{2N} - n_1{}^{2N})}{(n_2{}^{2N} + n_1{}^{2N})} \right]^2 \quad (2.2)$$

$$\frac{\Delta f}{f} = \frac{4}{\pi} \times arcsin\left(\frac{n_2 - n_1}{n_2 + n_1}\right) \quad (2.3)$$

where n_1 and n_2 are the refractive indices of the two alternating materials of the DBR and N is the number of periods.

For a design wavelength of around 1μm, GaAs and AlAs provide a high enough refractive index contrast (Δn = 0.25) that 25-30 pairs are sufficient to result in a theoretical reflectivity >99.99%. Figure 2.9 in the following page shows the reflectivity spectrum for a DBR designed for 1030nm using 25-pairs of GaAs/AlAs simulated using VERTICAL [17].

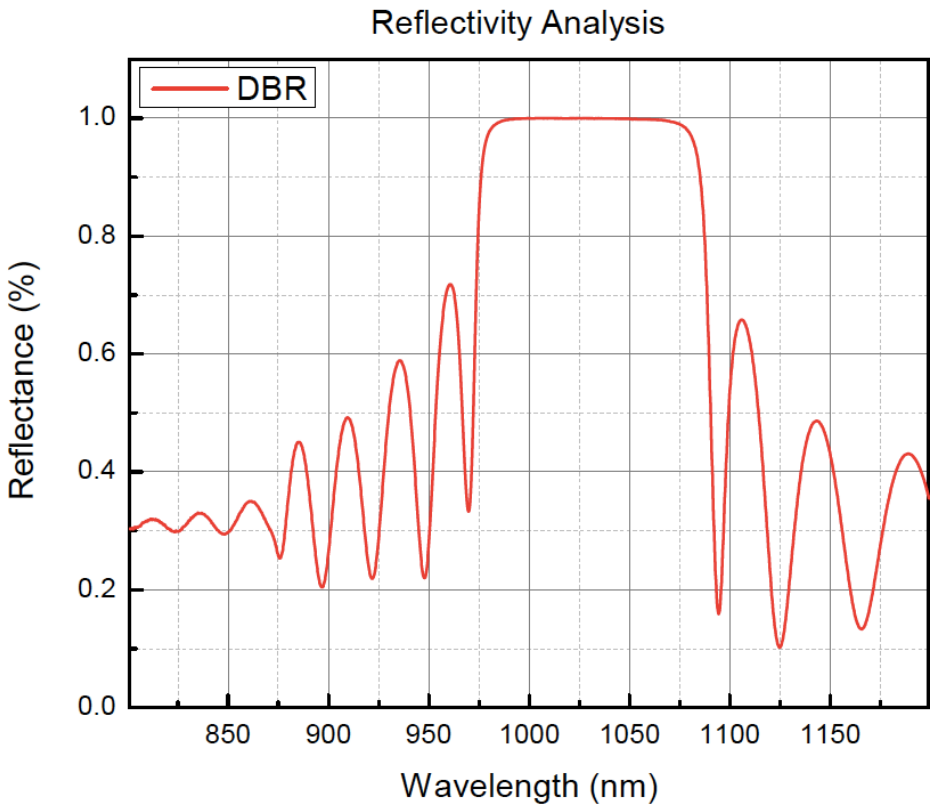

Figure 2.9: Reflectivity spectrum for a 25-pair GaAs/AlAs DBR mirror designed for 1030nm simulated using VERTICAL [17].

2.4.2 Design of SESAM absorber region

The electric field pattern in a SESAM structure can be predicted using a well-known transfer matrix algorithm for multilayer structures with an incident plane wave [18]. At a distance 'z' (measured from the substrate side), the electric field intensity is given by:

$$I(z) = n(z) \,.\, |\varepsilon(z)|^2 \,.\, I_{inc} \qquad (2.4)$$

where n is the refractive index, ε is the electric field (normalized to 1), I_{inc} is the incident intensity and the term $|\varepsilon(z)|^2$ is defined as the field enhancement.

At the absorber position, the strength of the standing electric field pattern determines some of the macroscopic parameters of the SESAM. Figure 2.10 below shows the refractive

index and field enhancement profiles in a standard SESAM. As the figure shows, the absorber region can be designed to operate either in an antiresonant or a resonant regime in terms of field enhancement. In both cases, the spacer layer between the absorber and the DBR is designed such that the absorber is positioned at the antinode of the standing wave pattern of the electric field. On the other hand, the cap layer controls the field enhancement at the absorber position and essentially controls the SESAM being resonant or anti-resonant. If the round-trip phase change is π (2n-1), it is in the anti-resonant regime and if it is $2\pi n$, the structure is resonant. In case of SESAMs based on nanostructure absorbers, the spacer and the cap layers also provide effective optical confinement for the QWs or the QDots.

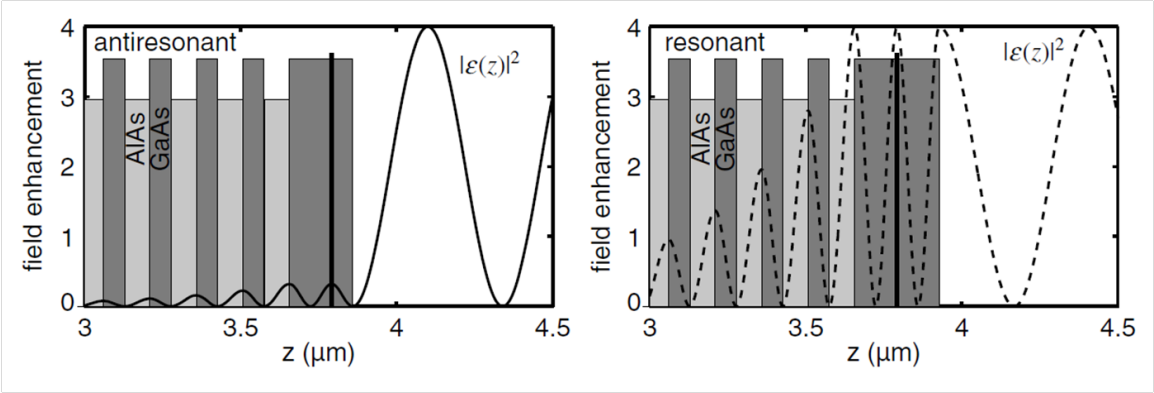

(a) (b)

Figure 2.10: Difference in field enhancement between a resonant and anti-resonant design [taken from 1]

The strategies worked on as part of this thesis for SESAM development mainly focus on anti-resonant SESAM structures. Anti-resonant structures offer a broad spectral range of operational stability (resonant designs are highly wavelength-selective) with almost constant saturable absorber parameters. They also show a higher damage threshold for lasers

with high pulse energies as the field intensity is minimized inside the structure, thus reducing non-saturable losses.

2.5 SESAM characterization

As mentioned earlier, this thesis focuses on optimizing the characteristics of a mode-locked VECSEL system by developing novel epitaxial strategies for the growth of SESAMs. In order to quantify this optimization process, characterization of macroscopic parameters of the SESAM is indispensable. In the following subsections, the different parameters characterized as part of the thesis are described along with the corresponding setups used:

Spectral Reflectivity: The reflectivity spectrum for a SESAM can be used to determine the central wavelength of the DBR stop-band and the spectral position of the absorber. For our designs, in order to obtain maximum reflectivity and better dispersion control (explained in a later subsection), the central wavelength for the DBR is to be aligned at the emission wavelength of the laser. The absorption wavelength of the QWs (or QDots) can be observed as a dip in the reflectivity spectrum and is typically at the center of the DBR stopband (shown in figure 2.11 below). The magnitude of the dip in reflectivity depends on the position of the absorber in the standing electric field. The spectral alignment of the DBR and the absorber is extremely critical to achieving a mode-locked state. The reflectivity spectrum for SESAMs described in this thesis are measured using a typical Fourier-transform infrared spectrometer setup with a white light source and an InGaAs detector, using a gold-mirror as a reference.

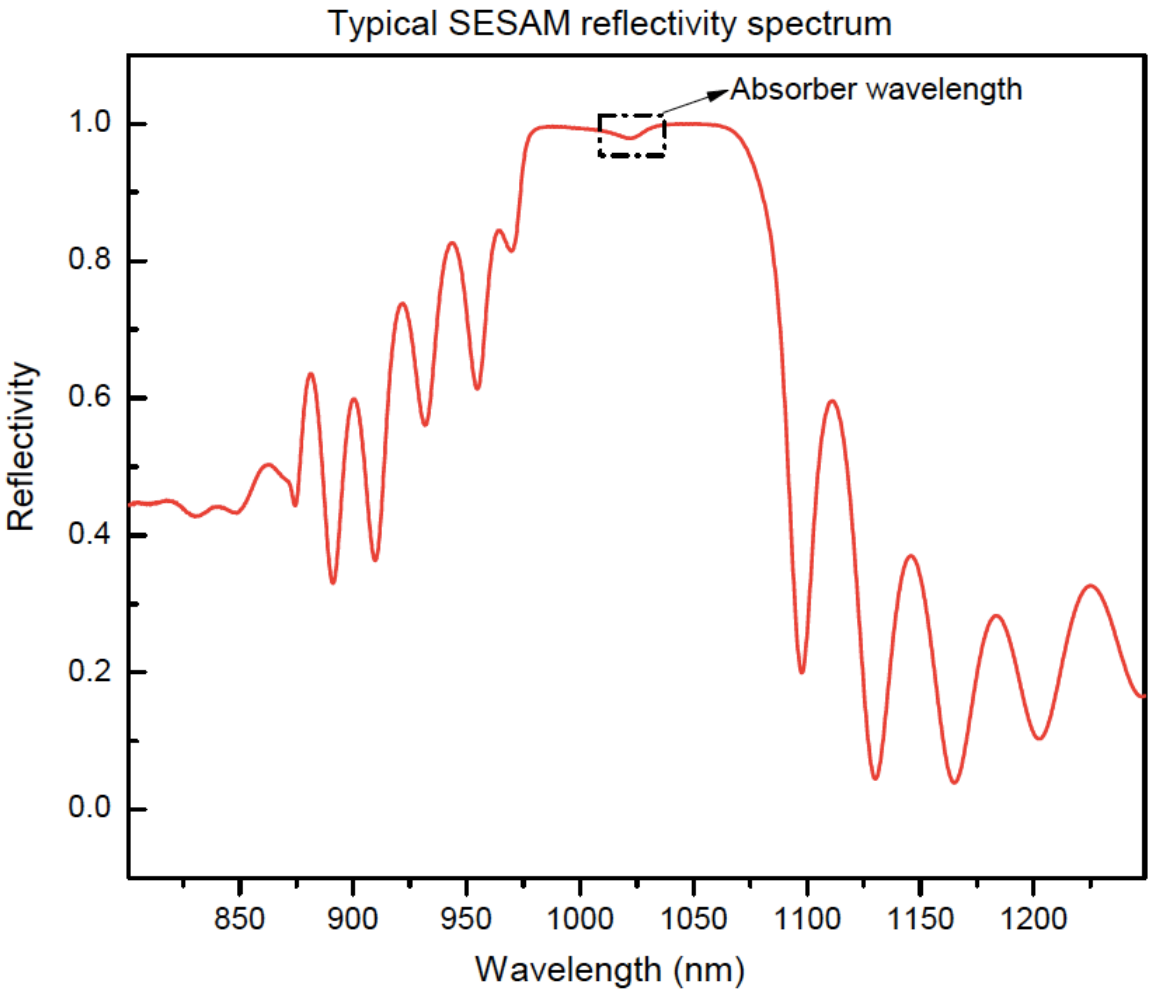

Figure 2.11: Typical reflectivity spectrum for a 1030nm SESAM with a dip in reflectivity labeled at the absorber wavelength.

Group Delay Dispersion (GDD): GDD has a strong influence on the pulse duration obtained from a mode-locked VECSEL [19]. The strong saturation observed in mode-locked VECSELs within both the gain and the absorber sections leads to a total temporal phase change. Matching this phase change with an appropriate positive GDD leads to the formation of pulses. [18] An asymmetric dependence exists between the pulse duration and GDD as shown in figure 2.12(a) (from [1]). It has been shown that a positive GDD leads to

the formation of substantially shorter pulses and that the effect of a higher positive GDD on the pulse duration is lower compared to a higher negative GDD. [20] GDD measurements are made using a Chromatis™ – Dispersion measurement setup from KMLabs. Figure 2.12(b) below shows a typical GDD measurement for a QW-based SESAM.

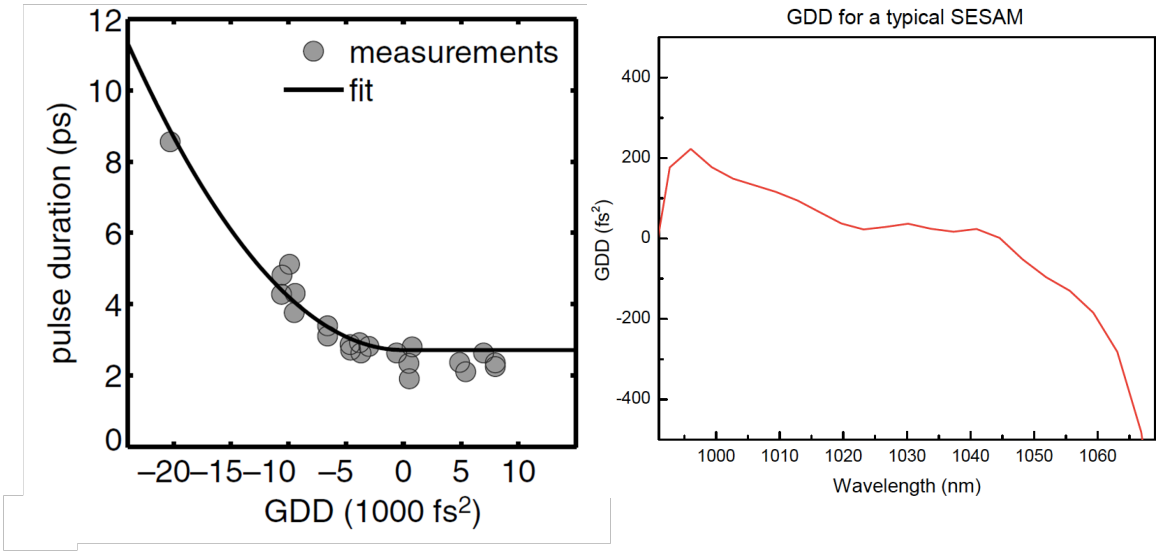

(a) (b)

Figure 2.12: (a) Dependence of pulse width on GDD (from [1]) (b) Typical GDD measured on a QW SESAM. The goal is to obtain a flat GDD profile on the positive side at the lasing wavelength.

Recovery time: The temporal response of SESAMs is also an important characteristic that determines the minimum achievable pulse duration. The recovery dynamics of SESAMs are measured using a standard pump-probe setup as shown in figure 2.13(a) below [21]. A pump-probe setup first splits the beam from a mode-locked laser at the design wavelength in two parts: a pump beam and a probe beam. The pump beam is of relatively high energy sufficient enough to saturate the absorber and the probe beam is of lower power (at least 10

times lesser than pump beam) to make sure that it does not affect the measurement. A controlled time delay is introduced to the probe pulses with respect to the pump pulses by using an optical delay line. Both beams spatially overlap on the SESAM. For each different time delay introduced in the probe beam, the changes in the probe pulse introduced by the pump pulse is measured. This technique allows resolution in the time scale shorter than the resolution of the photodiode and other elements used in the experiment (which usually operate in the micro or nano-second range). The pump and probe beams are chopped at different frequencies and lock-in detection is used to achieve better resolution and good signal-to-noise ratio.

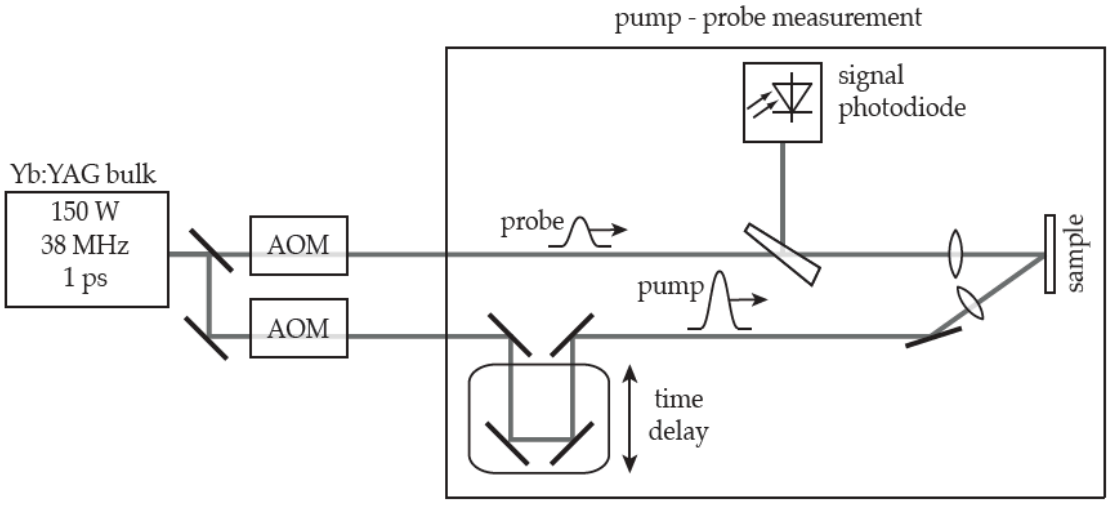

Figure 2.13: Non-linear Pump-probe setup used to quantify the temporal response of SESAMs.[taken from 21]

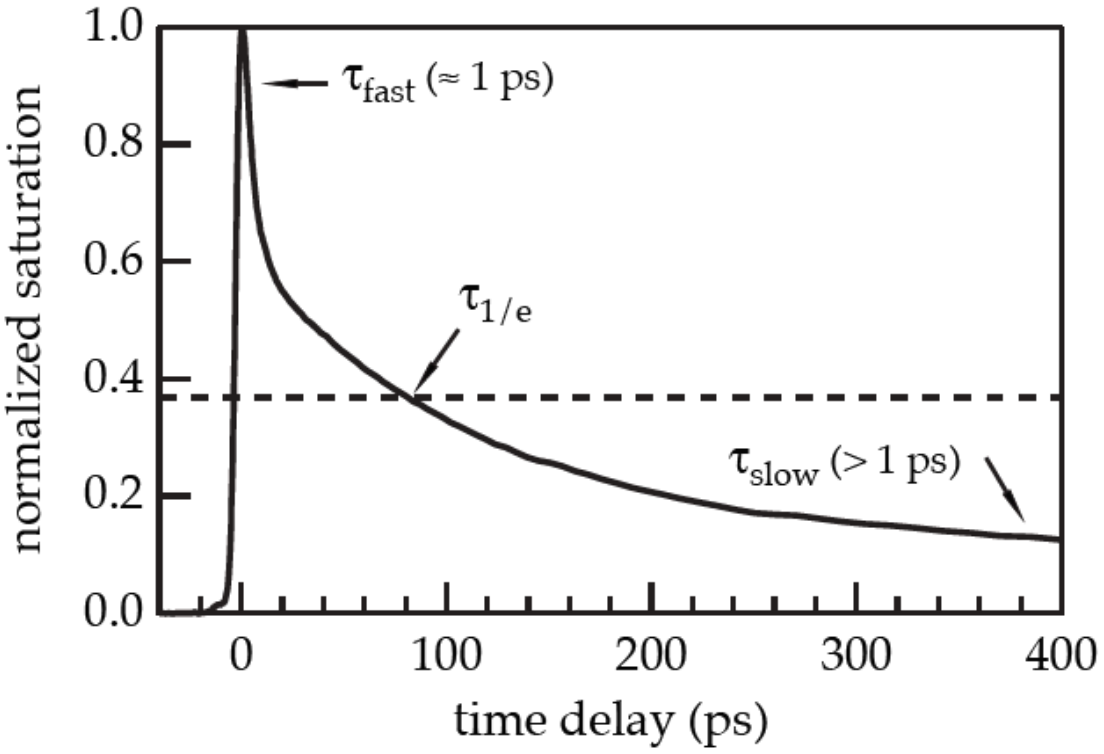

Figure 2.14 : Pump-probe measurements showing recovery dynamics for a typical SESAM(taken from [21])

.

Figure 2.14 shows the recovery dynamics for a typical QW SESAM at 1030nm [from 21]. This curve from most SESAMs can be fit to a bitemporal impulse response with two time constants given by:

$$\Delta R_{pp}(\tau) = Ae^{\frac{-\tau}{\tau_{slow}}} + (1-A)e^{\frac{-\tau}{\tau_{fast}}} \qquad (2.5)$$

where τ_{slow} is the slow component of the decay with an amplitude of A and τ_{fast} is the fast component of the recovery dynamics with an amplitude of (1-A). The fast recovery component is usually attributed to intraband "carrier-carrier scattering processes that lead to thermalization within the bands" [1]. This component is usually in the range of 100s of

femtoseconds. On the other hand, the slow recovery time is due to recombination or interband trapping. This usually is in the order of 1-100 picoseconds. Mid-gap states formed due to defects can usually serve as traps to improve the slow recovery time. This advantage is exploited in QW SESAMs where the QW is grown at a low-temperature (as low as 250^0C) to improve the temporal response. However, it is to be noted that this faster recovery time comes at the expense of higher non-saturable losses due to the defects.

2.6 Cavity design

The SESAMs characterized as part of this thesis are tested for mode-locking in a symmetric ring cavity:

Ring cavity:

The design of the ring cavity used is shown in figure 2.15 [14]. The VECSEL chip (gain wafer) is placed at ¼ of the total cavity length L = 92mm from the SESAM. This offers a symmetrical amplification of the two pulses traveling in the two different directions and makes sure that the pumping duration and gain recovery are equal for both pulses. A highly reflective concave mirror with r = 50mm and a flat output coupler with a reflectivity of 99.2% complete the cavity. This design provides a mode radius of 127µm on the gain chip and 67µm on the saturable absorber. The angle of incidence on both the VECSEL and the SESAM is adjusted to ~7^o.

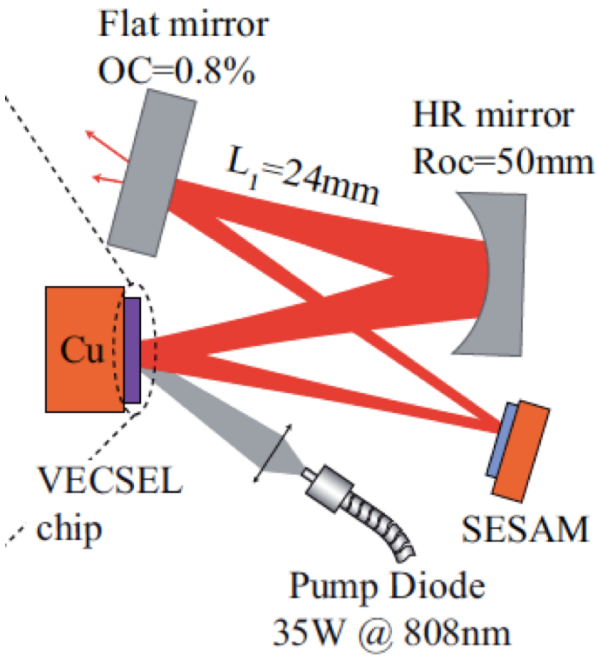

Figure 2.15: Ring cavity setup used to characterize SESAMs grown in this thesis(from [14])

References:

[1] Okhotnikov, Oleg G., ed. *Semiconductor disk lasers: physics and technology*. John Wiley & Sons, 2010.

[2] Zakharian, A. R., J. Hader, J. V. Moloney, S. W. Koch, P. Brick, and S. Lutgen. "Experimental and theoretical analysis of optically pumped semiconductor disk lasers." *Applied Physics Letters* 83, no. 7 (2003): 1313-1315.

[3] Rösener, B., N. Schulz, M. Rattunde, C. Manz, K. Köhler, and J. Wagner. "GaSb-based VECSEL exhibiting multiple-Watt output power and high beam quality at a lasing wavelength of 2.25 μm." In *Proc. of SPIE Vol*, vol. 6997, pp. 699702-1. 2008.

[4] Wilmsen, Carl W., Larry A. Coldren, and Henryk Temkin, eds. *Vertical-cavity surface-emitting lasers: design, fabrication, characterization, and applications*. Vol. 24. Cambridge university press, 2001.

[5] Safaisini, Rashid. "Impact of thermal management on vertical-cavity surface-emitting laser (VCSEL) power and speed." PhD diss., Colorado State University, 2011.

[6] Ahirwar, Pankaj. "Design, growth and optimization of 2-μm InGaSb/AlGaSb quantum well based VECSELs on GaAs/AlGaAs DBRs." PhD diss., 2013.

7] Leinonen, T., S. Ranta, M. Tavast, R. Epstein, G. Fetzer, N. Van Lieu, and M. Guina. "High power (23W) vertical external cavity surface emitting laser emitting at 1180 nm." In *SPIE LASE*, pp. 860604-860604. International Society for Optics and Photonics, 2013.

[8] Addamane, S. J., A. Mansoori, E. J. Renteria, N. Dawson, D. M. Shima, T. J. Rotter, C. P. Hains, L. R. Dawson, and G. Balakrishnan. "Development of III-Sb metamorphic DBR membranes on InP for vertical cavity laser applications." *Journal of Crystal Growth* 439 (2016): 104-109.

[9] Heinen, B., T-L. Wang, M. Sparenberg, A. Weber, B. Kunert, Jorg Hader, Stephan W. Koch, Jerome V. Moloney, M. Koch, and W. Stolz. "106 W continuous-wave output power from vertical-external-cavity surface-emitting laser." *Electronics letters* 48, no. 9 (2012): 516-517.

[10] Corzine, Scott W., Randall S. Geels, Jeff W. Scott, R-H. Yan, and Larry A. Coldren. "Design of Fabry-Perot surface-emitting lasers with a periodic gain structure." *IEEE Journal of Quantum Electronics* 25, no. 6 (1989): 1513-1524.

[11] Raja, MOHAMMAD YASIN A., Steven RJ Brueck, Marek Osinski, CHRISTIAN F. Schaus, John G. McInerney, T. M. Brennan, and B. E. Hammons. "Resonant periodic gain

surface-emitting semiconductor lasers." *IEEE Journal of Quantum Electronics* 25,no. 6 (1989): 1500-1512.

[12] Gbele, K., A. Laurain, Jorg Hader, W. Stolz, and Jerome V. Moloney. "Design and fabrication of hybrid metal semiconductor mirror for high-power VECSEL." *IEEE Photonics Technology Letters* 28, no. 7 (2016): 732-735.

[13] Laurain, Alexandre, Declan Marah, Robert Rockmore, John McInerney, Jorg Hader, Antje Ruiz Perez, Wolfgang Stolz, and Jerome V. Moloney. "Colliding pulse mode locking of vertical-external-cavity surface-emitting laser." *Optica* 3, no. 7 (2016): 781-784.

[14] Laurain, Alexandre, Robert Rockmore, Hsiu-Ting Chan, Jorg Hader, Stephan W. Koch, Antje Ruiz Perez, Wolfgang Stolz, and Jerome V. Moloney. "Pulse interactions in a colliding pulse mode-locked vertical external cavity surface emitting laser." *JOSA B* 34, no. 2 (2017): 329-337.

[15] Laurain, Alexandre, Cody Mart, Jorg Hader, Jerome V. Moloney, Bernardette Kunert, and Wolfgang Stolz. "15 W single frequency optically pumped semiconductor laser with sub-megahertz linewidth." *IEEE Photonics Technology Letters* 26, no. 2 (2014): 131-133

[16] Sheppard, C. J. R. "Approximate calculation of the reflection coefficient from a stratified medium." *Pure and Applied Optics: Journal of the European Optical Society Part A* 4, no. 5 (1995): 665.

[17] Frank H. Peters and W.L. Gore and Associates. Vertical Version 1.1 Beta, 1996

[18] Chilwell, John, and Ian Hodgkinson. "Thin-films field-transfer matrix theory of planar multilayer waveguides and reflection from prism-loaded waveguides." *JOSA A* 1, no. 7 (1984): 742-753.

[19] Paschotta, R., R. Häring, A. Garnache, S. Hoogland, A. C. Tropper, and U. Keller. "Soliton-like pulse-shaping mechanism in passively mode-locked surface-emitting semiconductor lasers." *Applied Physics B: Lasers and Optics* 75, no. 4 (2002): 445-451.

[20] Hoffmann, Martin, Oliver D. Sieber, Deran JHC Maas, Valentin J. Wittwer, Matthias Golling, Thomas Südmeyer, and Ursula Keller. "Experimental verification of soliton-like pulse-shaping mechanisms in passively mode-locked VECSELs." *Optics express* 18, no. 10 (2010): 10143-10153.

[21] Schriber, Cinia. "Towards high average power sesam-modelocked thin-disk lasers with short pulse durations." PhD diss., 2015

Chapter 3 : Development of InGaAs QW-based SESAMs

3.1 State-of-the-art QW-based SESAMs around 1μm

Most SESAMs used for mode locking of various laser types in the 1μm wavelength range consist of InGaAs QWs as the saturable absorber [1-5]. The indium content (x) in the $In_xGa_{1-x}As$ QWs and the composition of the barrier material can be adjusted to tailor the absorption wavelength for different pumping and lasing wavelengths. A tunable range of over 80nm has been demonstrated with emission wavelength of QW laser structures using QWs of different widths. [6] The low gain saturation fluence of the QWs allows passive mode-locking at several GHz repetition rates with little or no propensity towards Q-switching. Also, QWs exhibit a sufficiently wide gain bandwidth of ~30nm to be able to support subpicosecond pulses. [7]

The first optically-pumped passively mode-locked VECSEL was demonstrated in 2000 using an InGaAs QW gain and absorber region with the generation of 22ps pulses at 1μm [7]. This result was improved to obtain femtosecond pulses by 2002 [8]. In terms of pulse duration, pulses as short as 107fs (100mW power) and 60fs pulse bursts have been achieved to date. [9,10] The power levels with QW-modelocked VECSELs have been pushed as far as 6.4W (average output power) with 682 fs pulses leading to a peak power of 4.35kW. In addition, repetition rates as high as 50GHz has been achieved with

QW-modelocked VECSELs at 960nm. Table 3.1 summarizes record results obtained in the recent years from QW-modelocked VECSELs.[11]

	Record Value	Gain Medium	Wavelength
Pulse duration	107 fs	4 InGaAs QWs	1030nm
Average power	5.1W	10 InGaAs QWs	1030nm
Rep. rate	Highest: 50GHz Lowest: 85.7MHz	7 InGaAs QWs 16 InGaAs QWs	958nm 989nm
Peak power	4.35kW	10 InGaAs QWs	1013nm

Table 3.1: Summary of device characteristics of state-of-the-art QW-based SESAMs

From the literature survey presented above, it is apparent that the InGaAs QW-based SESAM is a well-established system for mode-locking VECSELs around 1µm. However, to the best of our knowledge, there hasn't been a study carried out to optimize SESAM properties (modulation depth, recovery time & GDD) based on a comprehensive growth strategy. Therefore, the following sections of this chapter focuses on epitaxial strategies for growth of SESAMs in general, leading to optimization of device properties for InGaAs QW-based SESAMs.

3.2 Epitaxial growth of SESAMs

The epitaxial growth process of SESAMs and its appropriate optimization is critical for the realization of high-performing SESAMs. This section introduces the epitaxial growth process using molecular beam epitaxy (MBE) and elaborates on a few aspects of growth that are relevant to this study.

All structures described in this thesis are grown using MBE in a VG V80H Semicon reactor. MBE is a technique for growing thin, epitaxial films of compound semiconductors with a highly precise control of composition and interfaces during growth. Over the years, this capability of MBE has been exploited to realize a wide range of extremely complicated structures including superlattice (SLS) devices, solar cells, VECSELs and SESAMs [12-16]. It uses localized ultra-high purity beams of atoms or molecules - produced from effusion cells - incident on a heated substrate in ultra-high vacuum (UHV) conditions (background pressures between 10^{-10} and 10^{-11} mbar). The UHV conditions avoid contamination of the growth and also ensure a collision-free path for the atomic or molecular beams. The reactor used for this study is equipped with group III (Ga, Al, and In), group-V (As and Sb) and dopant (Be as p-dopant; GaTe as n-dopant) sources. Shutters present in front of each source control the arrival of a flux of certain atoms or molecules on the heated substrate. The substrate is loaded in a wafer holder which is in close proximity to a substrate heater. The entire assembly can then be rotated during growth to reduce the effects of a non-uniform flux profile on the substrate due to the sources being at different incident angles. The substrate has sufficient thermal energy

for the arriving flux of atoms to migrate over the surface and locate their specific lattice site, thus forming a crystalline layer in registry with the substrate i.e. an epitaxial film. The flux of atoms from a given source is a function of the cell temperature which in turn depends on the amount of material in the cell. Figure 3.1 below shows a schematic [17] of a typical MBE growth chamber.

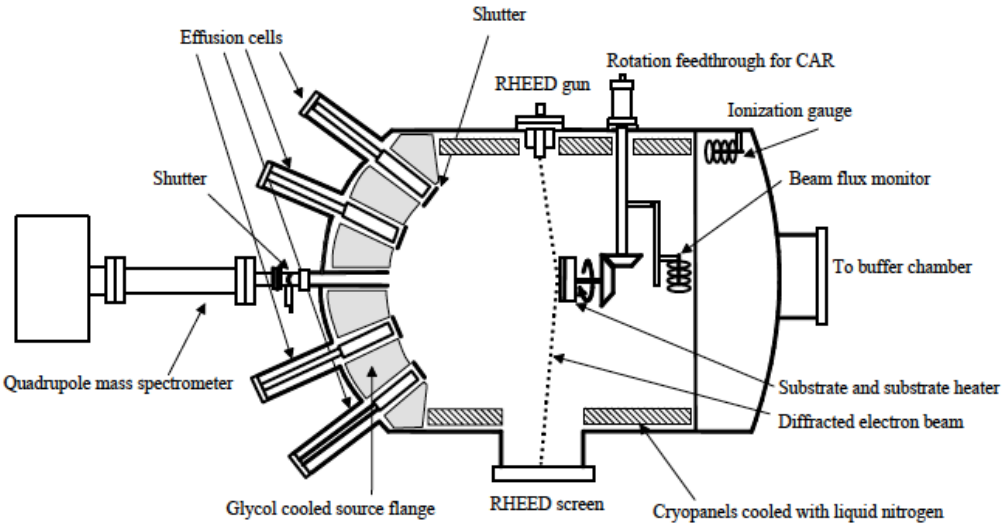

Figure 3.1 : Schematic of a typical MBE growth chamber (taken from [17])

MBE growth of SESAM structures described in this thesis is done on (100) epi-ready GaAs substrates. The substrates do not undergo any pre-treatment before being loaded into the machine. They are first introduced into the MBE-load lock chamber which is a small chamber completely isolated from the preparation and growth chambers and can be exposed to atmosphere to load samples and can quickly be evacuated to moderately high vacuums. Once the load-lock is evacuated, the substrates are transferred to a

preparation chamber (under high-vacuum) where they are outgassed at ~400^{0}C for 30 minutes to remove water vapor and other contaminants. This also ensures that consequently when the substrate is transferred into the growth chamber, heating it will not contaminate the UHV conditions. In the growth chamber, the substrate is first heated up to ~620^{0}C (specifically for GaAs) for thermal desorption of the surface oxide. The oxide desorption is carried out for 30 min with the substrate kept under a constant As-supply. An optical pyrometer looking directly at the substrate through a view-port mounted on the source flange is used to measure its temperature. Additionally, a technique (explained in detail in the following sections) called Reflection high energy electron diffraction (RHEED) is used to monitor the surface of the substrate during oxide desorption and during growth. At the oxide desorption temperature, the RHEED pattern changes from a diffuse scatter showing oxide rings to a distinct 3-D spotty pattern. Oxide desorption is carried out for ~30 min to ensure the removal of oxide layer over the entire wafer area and then, the substrate temperature is brought down to 580^{0}C for the growth of the structure. The structures for the different SESAMs and the specific growth process will be discussed in the relevant chapters. This thesis does not include an in-depth discussion on the process of MBE growth and its different components such as pumps, sources and gauges. General references for this are available from multiple sources. However, we have identified (based on our results), two aspects of growth using MBE that are relevant to the realization of SESAMs described in this thesis – RHEED oscillations and pyrometry. The following sections discuss in detail these two techniques and their significance towards the growth of SESAMs.

3.2.1 RHEED oscillations

RHEED is a tool used for in-situ surface characterization of epitaxial growth and is extensively used in MBE. It offers real-time detailed information regarding the growth surface such as growth modes, roughness, crystal quality and even surface temperatures. [18]. The RHEED setup, as shown in figure 3.2(a), consists of an electron gun, the wafer surface and a phosphorescent screen. The electron gun produces a small and highly-collimated electron beam that is accelerated at high voltages (operated at ~12kV on our reactor) incident on the epitaxial sample at a grazing angle. The diffraction pattern from the sample is analyzed on the phosphorescent screen. Our setup also includes a camera to capture different diffraction patterns during growth and to record the time dependence of these diffraction features.

The wavelength of high-energy electrons is much smaller than the lattice spacing and the grazing incidence angle on the surface is sufficient to create diffraction conditions. “The diffracted electrons interfere constructively at specific angles according to the crystal structure and spacing of the atoms at the sample surface and the wavelength of the incident electrons” [19]. Some of the electron waves created by constructive interference collide with the phosphorescent screen, creating specific diffraction patterns according to the surface features of the sample (as shown in figure 3.2(b)). The resulting

diffraction patterns can be analyzed to determine crystallographic information such as growth modes or roughness of the sample surface. However, by far, the most practical application of RHEED is the ability to calibrate growth rates based on time-resolved analysis of the intensity of the diffraction features.

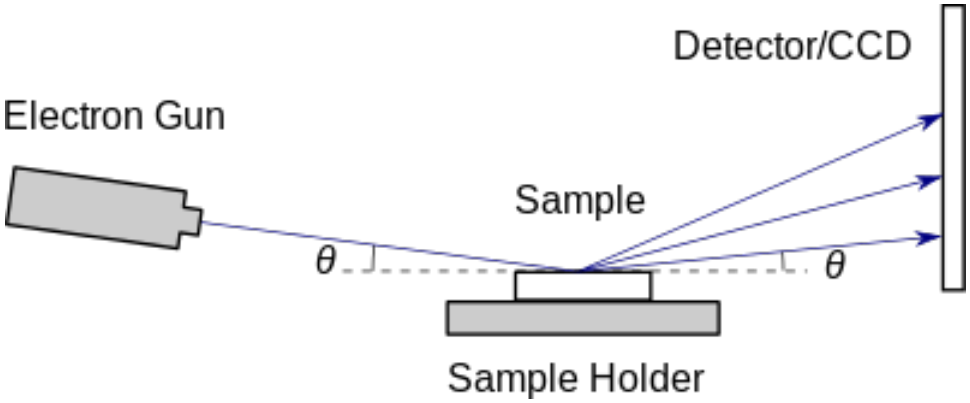

(a)

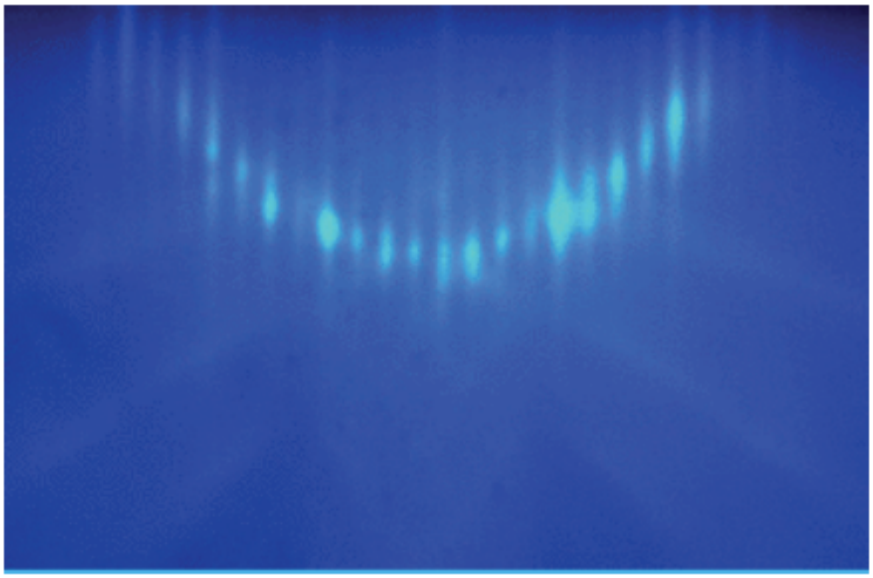

(b)

Figure 3.2 : (a)Schematic of a typical RHEED setup in MBE (b) typical RHEED pattern - this shows a 4 X GaAs pattern (taken from [20])

The number of atoms (or molecules) that incorporate into an epitaxial layer depends on the number of atoms arriving at the surface (i.e. growth rate) and the sticking coefficient of the species. Group V species such as As and Sb do not have a unity sticking coefficient i.e. not all the atoms (or molecules) arriving at the surface actually incorporate into the epitaxial layer. On the other hand, group III species such as Ga, In and Al have a unity sticking coefficient and so, the growth rate for typical III-V growth is group-III limited and the growth is carried out with an overpressure of Group-V. The growth rate can be calibrated for each Group-III based on their temperatures and this can be done using RHEED oscillations. In the Frank-van der Merwe growth mode (layer-by-layer growth), the intensity of a bright spot on RHEED oscillated as the growth occurs and the period of these oscillations correspond to the growth of a complete monolayer. For an atomically flat surface, the intensity of the RHEED spot is maximum. As the atoms arrive at the surface, they first start nucleating as 2-dimensional islands and the resulting roughening of the surface causes the intensity of the RHEED spot to decrease as it causes more diffuse scattering of the electron beam. At the deposition of exactly half a monolayer, the intensity of the RHEED beam is minimum. However, as the growth progresses, the atoms arriving now can migrate to the existing step edges to complete the growth of a complete monolayer and restore the intensity of the RHEED beam. Figure 3.3 (a) shows this trend in the RHEED spot intensity corresponding to the state of the surface being analyzed. This variation in RHEED spot intensity can be recorded using a

camera and analyzed to determine the growth rate. Each oscillation in the intensity corresponds to one monolayer and by averaging over 30-40 oscillations the growth rate can be determined. As shown in figure 3.3(b), a computer program can be used (ksa 400 used here) to fit the oscillation data to either a Fast Fourier transform or a damped sine – wave (shown here) to accurately calculate the growth rate of a given Group-III in monolayers/sec.

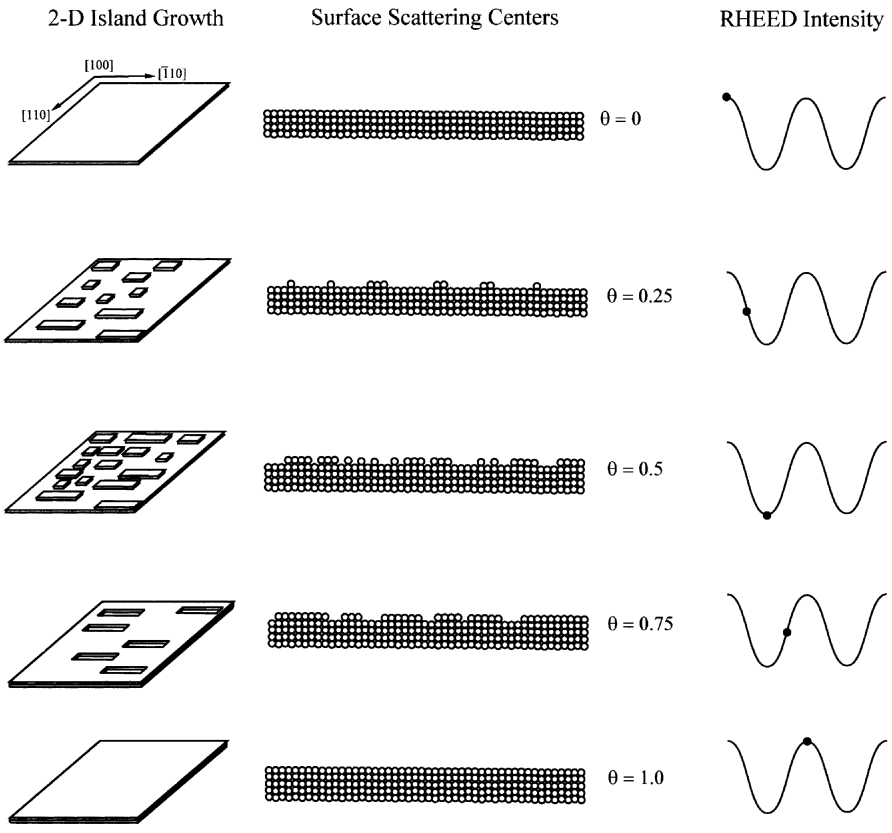

(a)

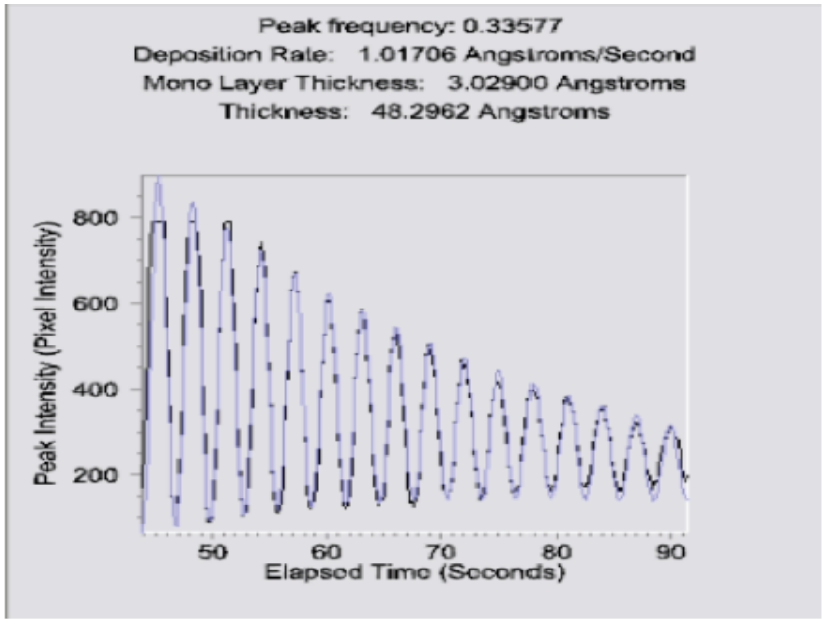

(b)

Figure 3.3 : (a) Trend in idealized RHEED intensity corresponding to the state of the surface being analyzed during the growth of a complete monolayer [taken from 12]. (b) Using the ksa400 program, RHEED oscillations data for a Group-III species is fit to a damped sine-wave to determine exact growth rates [taken from 20]

As the upcoming sections will illustrate in more detail, growth rate calibrations are critical to the growth of SESAMs. The device properties of SESAMs are highly sensitive to variation in intended thicknesses and therefore there is a need to be able to accurately determine growth rates. The devices discussed in this study are grown on GaAs and mostly contain either GaAs or AlAs layers. Therefore, RHEED calibrations for Ga and Al sources are performed before each growth on a 0.4 X 0.4 cm piece of GaAs mounted on a Molybdenum plate at typical growth temperatures for GaAs. (580-600^{0}C)

3.2.2 Pyrometry

In the MBE setup described above, the temperature of the substrate is measured using an optical pyrometer. Apart from determining oxide desorption temperature, the pyrometer is extensively used to adjust the growth temperature of different materials. In the context of growth of SESAMs, pyrometry is especially significant for the growth of the absorber. The optical properties and the temporal response of carrier dynamics in the absorber are highly dependent on the growth temperature of the absorber region.

A pyrometer essentially measures thermal radiation intensity of a target in a given wavelength range which depends on the target temperature. From the intensity, the temperature is calculated using Planck's black body radiation formula. It is important to note that the measured emission spectrum depends on the substrate material and transmissivity of the port window that the pyrometer is mounted on. Also, a pyrometer is only useful in a given wavelength range which translates to a given temperature range. We have used a pyrometer with a response above the band gap of the substrate as it allows the measurement of radiation from the substrate, not radiation being transmitted through the substrate from the heater assembly behind the substrate. For the SESAMs discussed in this study, we use a Ircon Modline 3 pyrometer with a wavelength range of 0.91-0.97μm which is well-suited for the growth temperatures of the SESAM. However, we have also attempted to grow the absorber layers at lower temperatures ($< 400^0$C) and it is to be noted that the sensitivity of the pyrometer considerably drops at these temperatures. We have used an emissivity of 0.687 for growths on GaAs substrates.

In general, the growth temperature of all of the sections of the SESAM are critical for optimum optical properties. In addition, as explained in the section regarding recovery dynamics of SESAMs in the previous chapter, the growth temperature of the QW itself is highly significant to the temporal response of the SESAM.

3.3 DBR growth optimization

A significant challenge for optimization of the SESAM growth involves the development of epitaxial strategies for the growth the DBR. The optical quality of the DBR is critical to the SESAM device characteristics such as the modulation depth and saturation fluence. Moreover, the position of the DBR stopband with respect to the lasing wavelength determines the effective GDD in the cavity.

3.3.1 Epitaxial growth process for the DBR

The typical growth process for a GaAs/AlAs DBR (and SESAMs in general) is as follows. Prior to epitaxial growth, the native oxide on the GaAs substrate is removed by thermal desorption of the substrate at ~620^0C for 30 min under an As_2 overpressure. This is followed by the growth of a 200nm thick GaAs smoothing layer at 580^0C. Once the GaAs is smoothened out, (confirmed by RHEED transforming to a 2X4 pattern) the growth of the DBR layers consisting of 0.25λ thick AlAs/GaAs is initiated. For a design wavelength of 1030nm, the GaAs and AlAs thicknesses turn out to be 88.2 and 74.4nm, respectively. Although 24-25 pairs would yield sufficient reflectivity, for the SESAMs described in this thesis, we have used a 29-pair DBR to minimize the non-saturable losses. This makes the DBR layer ~5-6μm thick and for moderate growth rates of 0.3-0.5ML/sec,

it becomes critical to control the growth rates of GaAs and AlAs over long periods of time.

3.3.2 Growth rate stability over time

The growth rates for Ga and Al are calibrated pre-growth using RHEED oscillations. To quantify the stability of the growth rates over long periods of time, the RHEED oscillations are repeated over a period of ~16 hours which would be the typical growth time for a SESAM. As seen in figure 3.4, while the Ga growth rate stays fairly stable over the 14 hours, the Al growth rate decreases at a rate of ~0.43%/hour and effectively decreases by ~3.5% over a period of 14 hours. This anomalous behavior of the Aluminum effusion cell, as compared to Ga can be explained on the basis of difference in behavior of the source material. As the source material melts, while Ga ($T_{melting}$ = ~30^0C) and In ($T_{melting}$ = ~150^0C) form a puddle of liquid at the bottom of the crucible, Al ($T_{melting}$ = ~660^0C) is known to wet the surface of the crucible [21,22]. This makes the geometry of the crucible critical and complicates the process of stable evaporation of source material over a long period of time. The effect of the crucible geometry is discussed later in this chapter.

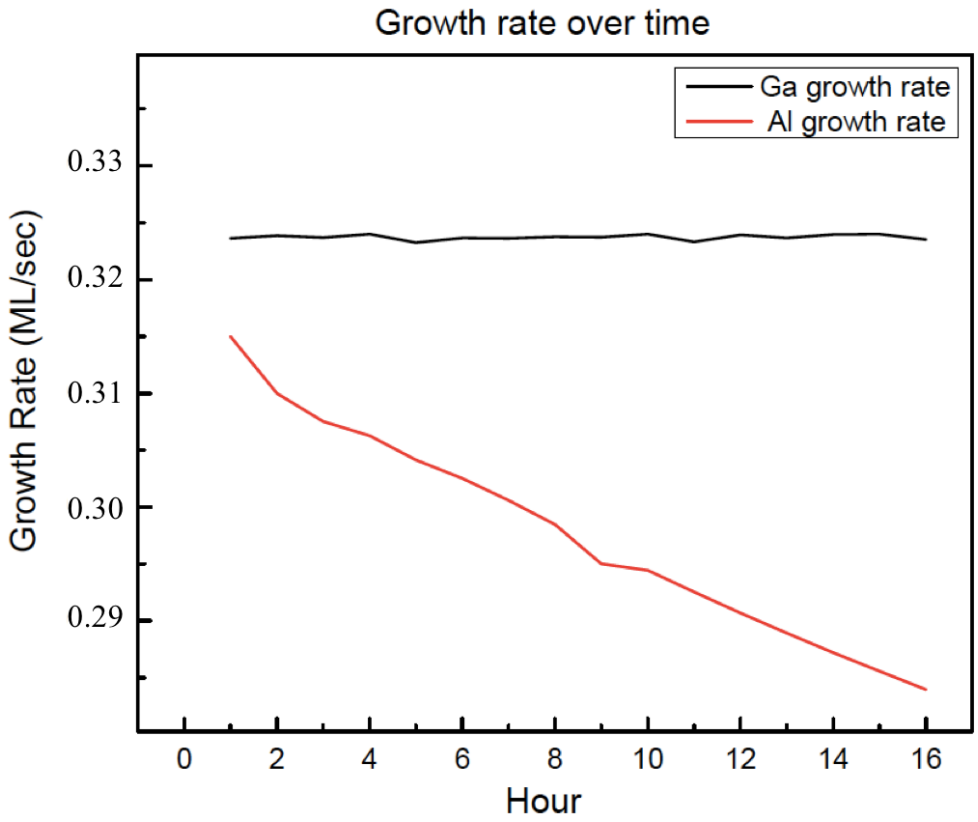

Figure 3.4 : Growth rate stability for Ga and Al effusion cells used to grow a 29-pair DBR over a period of 14-16 hours.

In order to overcome the slow decrease in growth rate of Aluminum, the temperature of the source is ramped up slowly during the growth. The data collected for the growth rate over 16 hours is fitted to a straight line and based on the slope of this line, the ramp rate for Al over the course of a DBR growth is determined. Figure 3.5 shows the reflectivity spectra for a 29-pair GaAs/AlAs DBR. The black curve shows the reflectivity spectrum with no correction for the drift in Al growth rate. As the growth proceeds, the AlAs layers get progressively thinner for each stack and this leads to an effective blue shift of the DBR stop-band (~8%) and skews the interference fringes in the lower wavelength range.(This effect is verified by VERTICAL simulations.) The red

curve in the figure below is the DBR stop-band with the Aluminum source temperature being ramped up over the course of the growth at an extremely (0.01^{0}C/min) small ramp rate. Although the interference fringes on the lower wavelength side are still slightly skewed, the DBR stop-band is now centered at 1030nm. Aside from ramping up the Al source temperature over time, we also investigated the possibility of using a different Al source geometry. The source used for the measurements discussed above is an Al effusion cell with a conical shaped crucible. A new generation of Al effusion cells named "SUMO" ® cells with a different crucible geometry (explained in the following section) have been shown to have a better growth rate stability over time [23]. Therefore, instead of having to ramp up the Al source to correct for the drift in growth rate, we attempted the use of SUMO® cells. The following section of this chapter describes the results from this change and the challenges we faced.

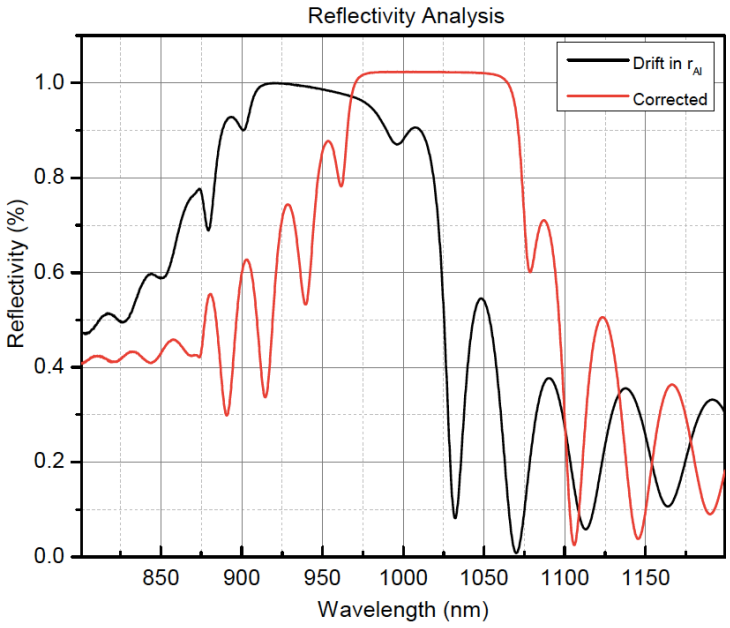

Figure 3.5 : Comparison of reflectivity spectra for a 29-pair GaAs/AlAs DBR mirror (at 1030nm) for a drift in Al growth rate uncorrected (black) and corrected (red).

3.3.3 Growth rate stability over wafer area

As mentioned in the previous section, in order to obtain better growth rate stability over time, we installed a state-of-the-art Al effusion cell with a novel design ("SUMO"® cell) instead of our conventional Al conical cell. Figure 3.6 illustrates the difference between effusion cells using conical and SUMO® crucibles. While the geometry of the conical crucible is exactly what the name suggests (a cone), the SUMO® crucible "incorporates a constricted orifice and an exit cone that extends beyond the front heat shielding of the cell"[24]. The SUMO® crucibles were designed as an upgrade to the existing conical crucibles and are supposed to result in:

- Relatively larger thermal gradient between base and tip to reduce Al creeping along walls of the crucible.
- Increased capacity to load a larger charge of Aluminum for increased operating time.
- High growth rate stability over time

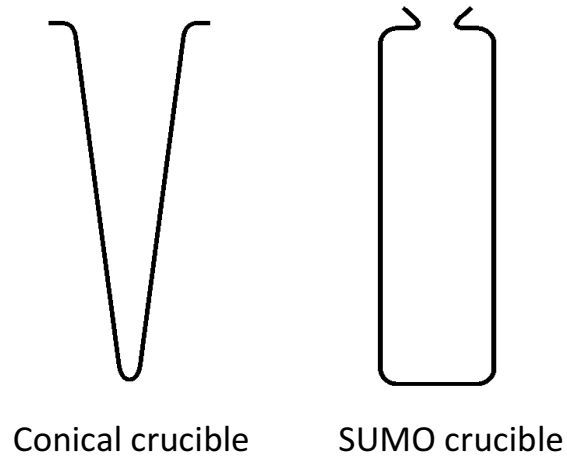

Figure 3.6 : Schematic showing geometrical differences between a conical and "SUMO" crucibles

The use of the SUMO® effusion cells certainly helped with the growth rate stability over time. The growth rate drift over 14-16 hours was measured using RHEED oscillations to be a mere ~0.9% (compared to 3.5% with conical cells) and the DBR stop-band could be aligned to be centered at 1030nm without ramping up the Al cell temperature during the growth of the mirror. However, the SUMO® cell posed a different challenge for optimized growth of the SESAM. This cell was found to have extremely poor uniformity of the Al flux over the entire area of the wafer (2" diameter). Figure 3.7 shows the variation of the reflectivity spectra for a 1030nm DBR over a 2" wafer. The DBR stop-band blueshifts by ~11% at a distance of 3 cm (1inch) from the center of the wafer. This indicates that the Al flux decreases pretty quickly as we move from the center of the wafer towards the edges. This leads to thinner (than 0.25λ) AlAs layers at the edges, which in turn leads to the blueshift of the DBR stop-band. In order to verify this, RHEED oscillations are performed across a 2" GaAs wafer moving from center to edge and the

growth rate is found to decrease by 10.3%. This drift in growth rate and consequently a drift in the DBR stop-band essentially leads to an enormous decrease in the yield of usable devices that can be realized over a 2" wafer.

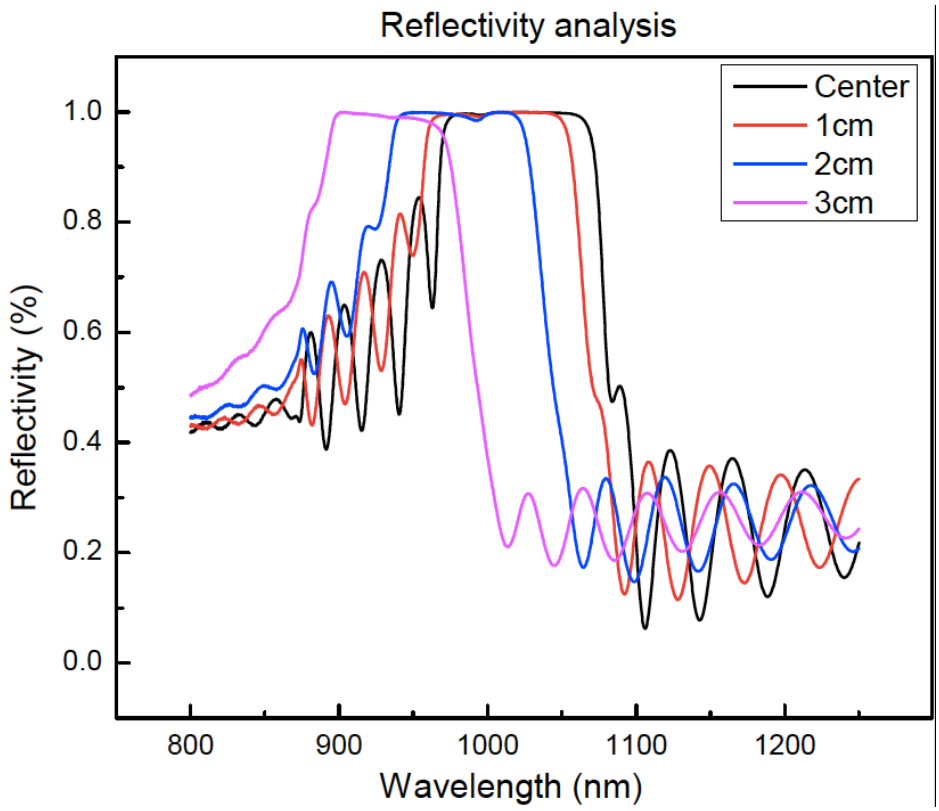

Figure 3.7 :Reflectivity spectra showing the variation of DBR stop-band over a 2" diameter wafer. The drift in Al growth rate causes a corresponding blueshift of the DBR stop-band

Various approaches including varying the growth rate and varying the temperature gradient between the base/tip of the cell were attempted to alleviate this drift in growth rate over the area of the wafer. However, none of these methods seemed to be making a difference to the poor uniformity of the Al flux. Finally, on careful analysis of the specifications of the SUMO effusion cell, we realized that the design of the cell was

calibrated for a newer generation of reactors where the substrate-source distance is larger than the substrate-source distance on the VG V80H MBE reactor that is being used for this study. Assuming a conical profile for the source flux, it is apparent from figure 3.8 that if the source designed for a source-substrate distance of "L" is operated at a lower source-substrate distance, the uniformity of the flux is going to be affected. The width of the flux profile cone determines the extent of uniform flux over the wafer and at smaller distances, the uniformity is lower. This explains the significantly lower Al growth rates at the edges of the wafer.

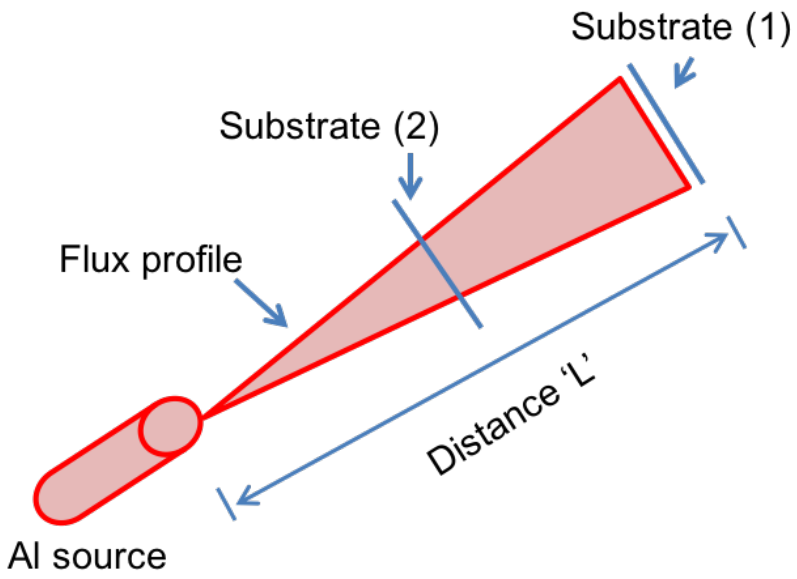

Figure 3.8 : Schematic showing the effect of the substrate-source distance on the flux profile. The source is designed for a distance equivalent to "Substrate (1)" (which is L) and the distance in our reactors is at "Substrate (2)"

To correct for this, we measured the exact distance between the source and the substrate for our reactor and added a spacer of appropriate length to pull the source back

and effectively increase the source-substrate distance to as close to "L" as possible. Figure 3.9 shows the effect of the retracted Al cell on the variation of DBR stop-band between the center and edge of a 2" wafer. The drift in the center of the stop-band is brought down to ~3% from the previous 11% with a smaller substrate-source distance. With the issue of growth rate stability over time and over the wafer solved, we were now able to grow precise DBRs for the SESAM designs.

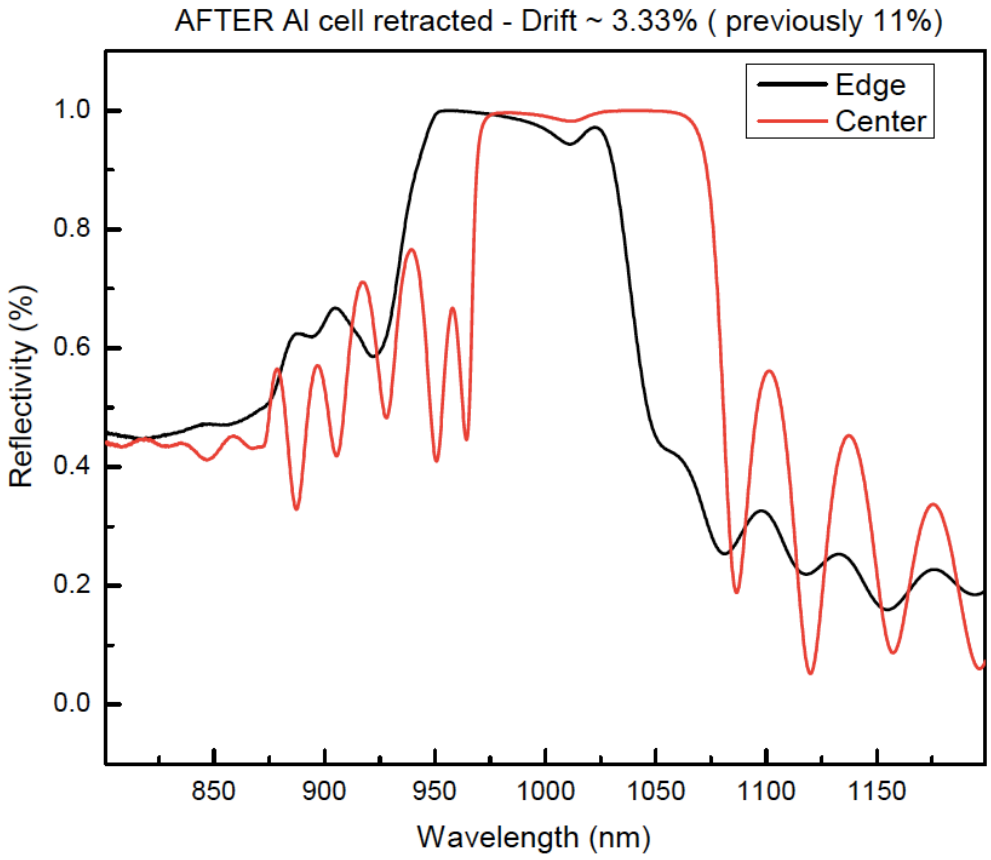

Figure 3.9 : Reflectivity spectra showing the variation of DBR stopband over a 2" diameter wafer between the center and the edge. The drift is brought down to ~3% by adding a spacer.

3.4 Epitaxial growth process for the absorber region

Once the growth of the DBR is optimized, the growth structure and process for the rest of the SESAM is fairly straightforward. Following the growth of the 29-pair GaAs/AlAs DBR, a 22nm GaAs spacer layer is grown at the DBR growth temperature (580^0C). As mentioned before in this chapter, this spacer layer controls the position of the QW with respect to the standing wave pattern of the electric field. The substrate temperature is then brought down to 475^0C for the growth of the QW. The composition and thickness of the QW are $In_{0.18}Ga_{0.82}As$ and 8.35nm respectively. After the growth of the QW, a 1.5nm thick cold GaAs cap is grown to protect the QW. For the growth of the rest of the GaAs cap, the substrate temperature is brought back up to 580^0C. The total thickness of the cap is kept at 7nm. This thin GaAs cap, along with ensuring optical confinement for the QW, also leads to a faster recovery time as the carriers have access to surface states through tunneling. Figure 3.10 shows the structure used for the InGaAs QW SESAM. The growth rates of In and Ga (calibrated by RHEED oscillations) were 0.06ML/sec and 0.3ML/sec respectively (in a ratio of r_{In} / r_{Ga} = 0.18/0.82 for the composition of the QW) and a constant As: Ga flux ratio of 13 is maintained. As mentioned before, this structure is used as a baseline for the rest of the structures discussed in this thesis.

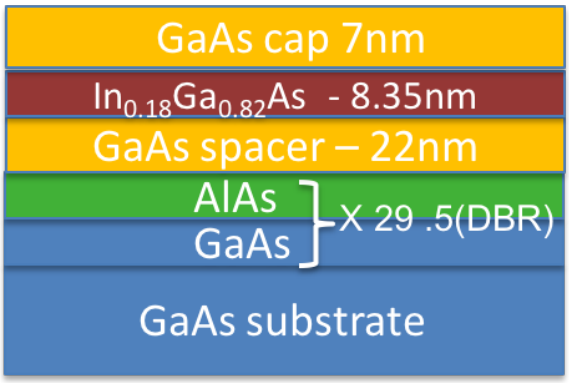

Figure 3.10: Schematic of the exact structure used for growth of the InGaAs QW SESAM at 1030nm.

3.5 Alignment of absorber wavelength using Photoluminescence (PL)

Before growing the rest of the SESAM structure on a DBR, the InGaAs QW layer (8.35nm) is grown on a GaAs substrate with a 7nm GaAs cap on top (typical procedure used for oxide desorption and smoothing layer before QW growth as explained in previous section). This is done in order to verify the composition of the $In_xGa_{1-x}As$ QW which in turn determines the absorption wavelength. Figure 3.11 shows the room-temperature PL measurement for the nominal $In_{0.18}Ga_{0.82}As$ QW grown on GaAs with a 7nm GaAs cap. The peak wavelength is at ~1015nm and is perfectly aligned for the SESAM. The FWHM of the PL peak can be calculated to be 20.24nm. It is to be noted that the absorption wavelength of the QW is intentionally blueshifted vs the emission wavelength of the VECSEL (1015 vs 1030nm) to help align the cavity. Once the cavity is lined up, the SESAM wafer can be heated up to ~40-50^{0}C and the QW absorption wavelength can be lined up at the laser emission wavelength.

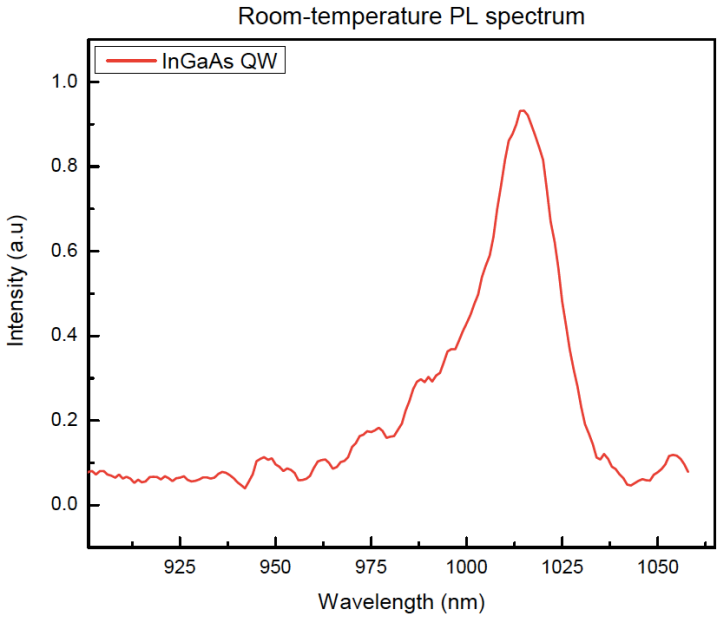

Figure 3.11 : Room-temperature PL spectrum from InGaAs QWs with emission wavelength aligned at ~1015nm.

3.6 Spectral reflectivity measurements

With the DBR growth process optimized and the QW absorption wavelength aligned, the InGaAs QW-based SESAM structure shown in figure 3.10 in the previous section is grown and characterized. Figure 3.12 shows the room-temperature reflectivity spectrum for this SESAM. The DBR stop-band extends from 975nm to 1080nm and is centered at ~1020nm. Although this is slightly blueshifted (~1%), the reflectivity is sufficiently high at 1030nm. The dip in reflectivity at ~1025nm can be attributed to absorption from the InGaAs QW.

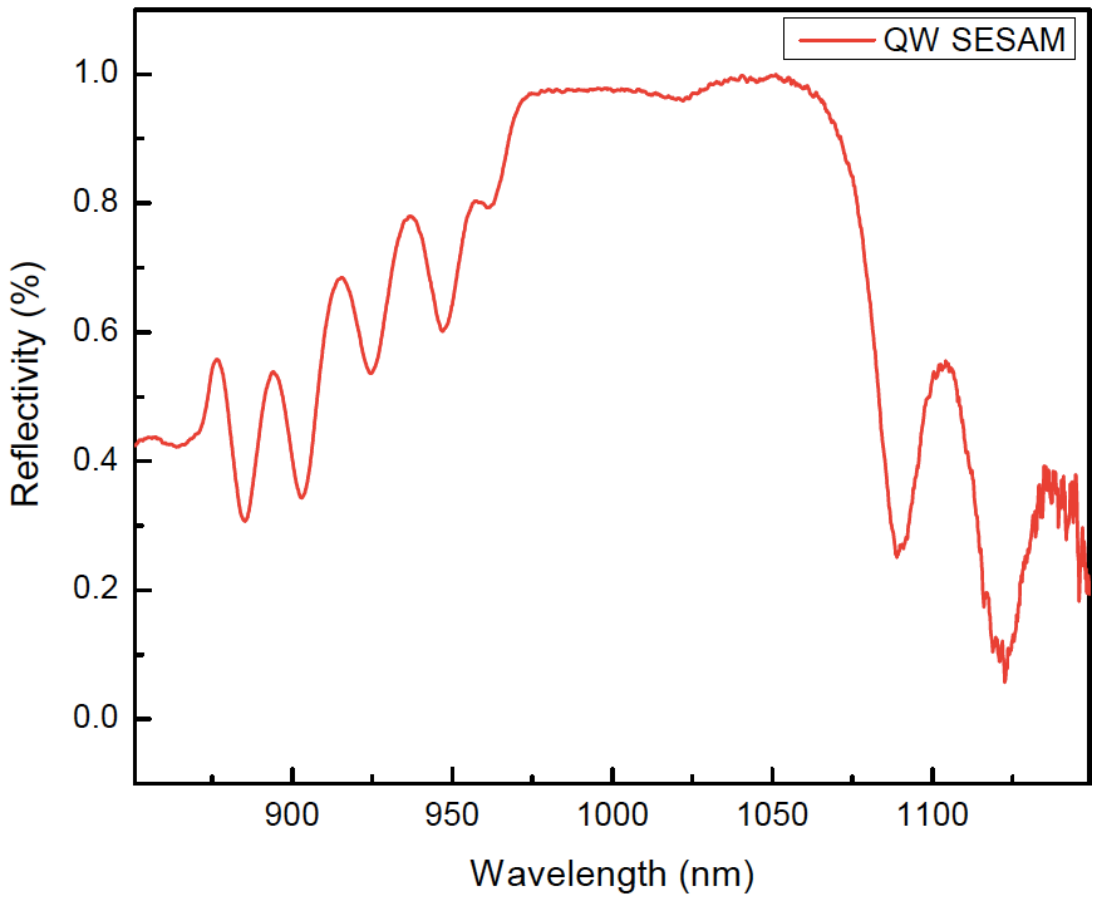

Figure 3.12 : Room-temperature reflectivity spectrum from InGaAs QW-based SESAM with the stoopband wavelength centered at ~1020nm and InGaAs QW absorption dip at 1025nm.

In order to align the QW absorption with the VECSEL emission wavelength, the SESAM chip might have to be heated or cooled accordingly. Therefore, it is important to understand the trend in QW absorption wavelength with temperature. Figure 3.13 shows a magnified view of figure 3.12 around 1025nm measured at different temperatures. The dip in reflectivity observed in figure 3.13 can be attributed to the QW absorption. As the temperature increases, the dip redshifts corresponding to shift in emission wavelength of the QW due to band shrinkage. The shift in absorption wavelength with temperature can be approximated to a linear fit to determine the temperature stability of the QW. The slope

of this linear fit was found to be 0.303nm/^{0}C. In addition to the shift in the absorption, a redshift in the DBR stop-band is observed. This redshift is due to the slight variation of the refractive indices with temperature of the materials comprising the DBR (GaAs and AlAs). Based on the reflectivity spectra, the anti-reflection coating (TaO_2/SiO_2) is designed and deposited to enhance absorption. The results discussed from this point onwards for the rest of this chapter refer to coated QW SESAMs.

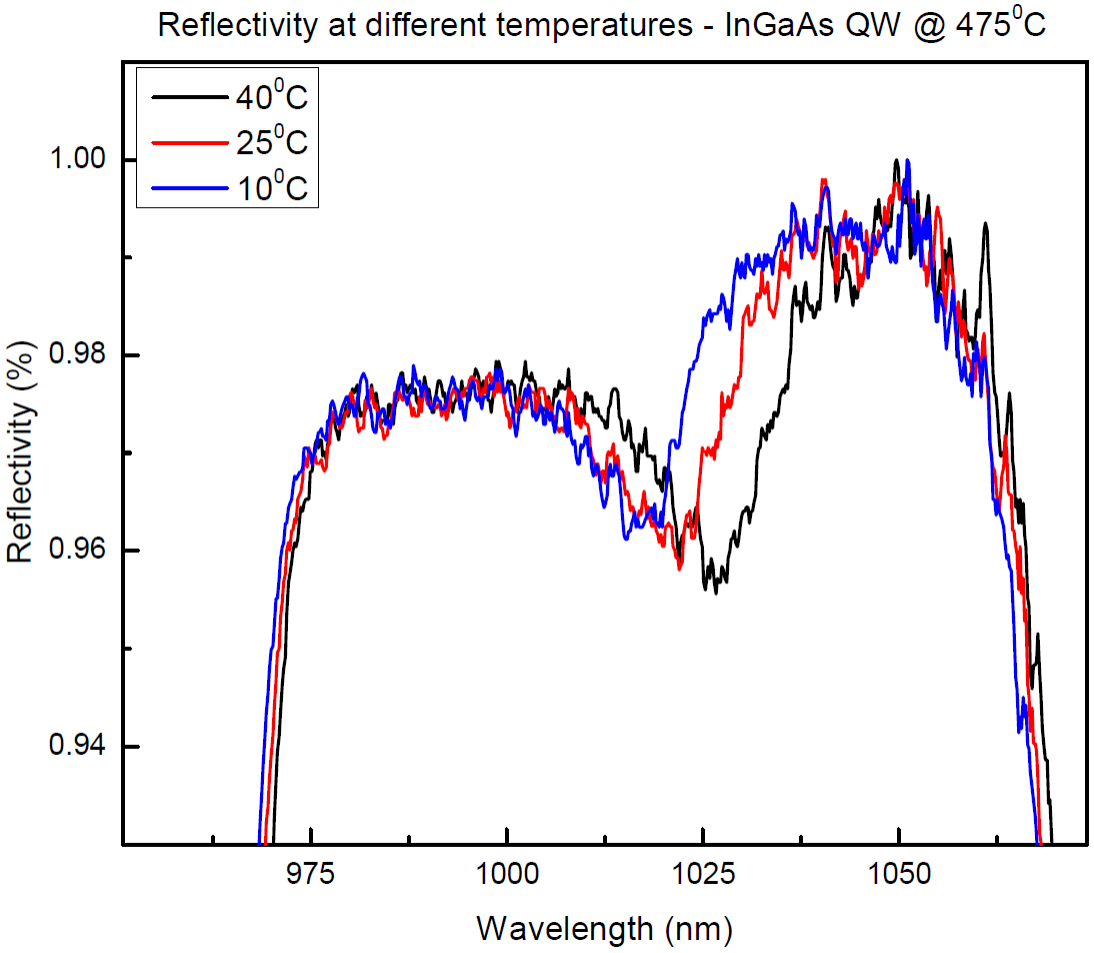

Figure 3.13 : Variation in reflectivity spectra with temperature. Along with the slight shift in stop-band, the QW absorption dip moves by ~0.303nm/^{0}C.

3.7 Recovery time measurements

To understand carrier recovery dynamics of the SESAM, the transient change in reflectivity is measured using a pump probe setup and is shown in figure 3.14 [25]. The carrier recovery dynamics measured can be fit to a slow and a fast time constant using as described in Chapter 2.

$$\Delta R_{pp}(\tau) = Ae^{\frac{-\tau}{\tau_{slow}}} + (1-A)e^{\frac{-\tau}{\tau_{fast}}} \qquad (3.1)$$

The time constants deduced from the fit are shown in table 3.2

Time constant (τ)	
τ_{fast}	400 fs
τ_{slow}	20 ps

Table 3.2: Fast and slow components of recovery time for InGaAs QW-based SESAMs

The fast decay can be attributed to intraband electron-electron and electron-photon scattering. [17] The second decay is governed by the tunneling of carriers into surface states or recombination.

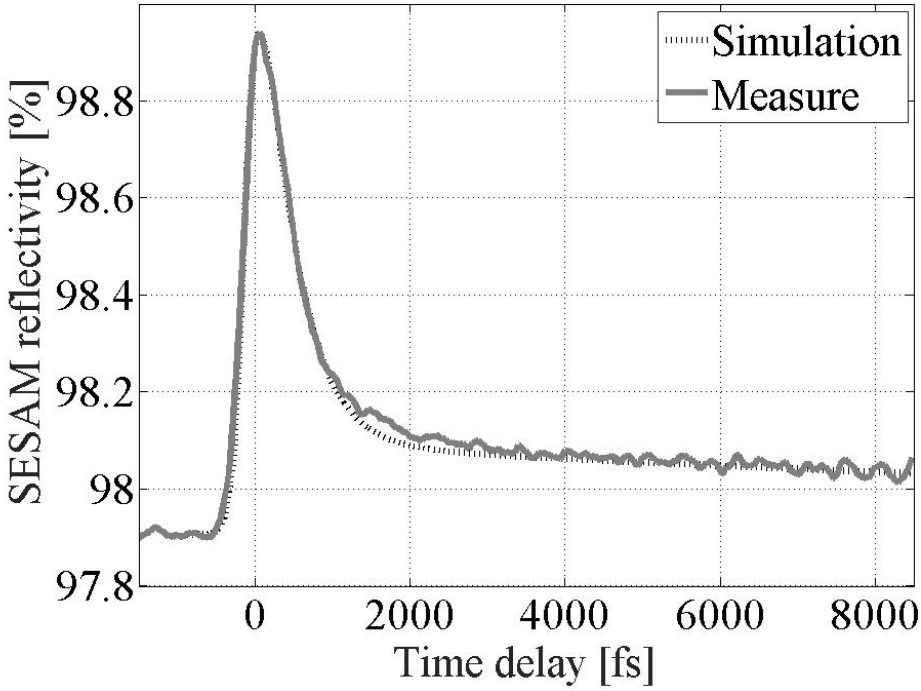

Figure 3.14 : Recovery-time measurements carried out using pump probe setup. It clearly shows the existence of two different recovery mechanisms (from [25])

3.8 GDD measurements

The GDD for the QW-based SESAM around the wavelength of interest (1030nm) is measured before further device testing. The anti-reflection coating reduces the cavity enhancement and flattens the GDD profile as expected. As figure 3.15 shows, the GDD is relatively flat between 1020-1030nm and stays positive.

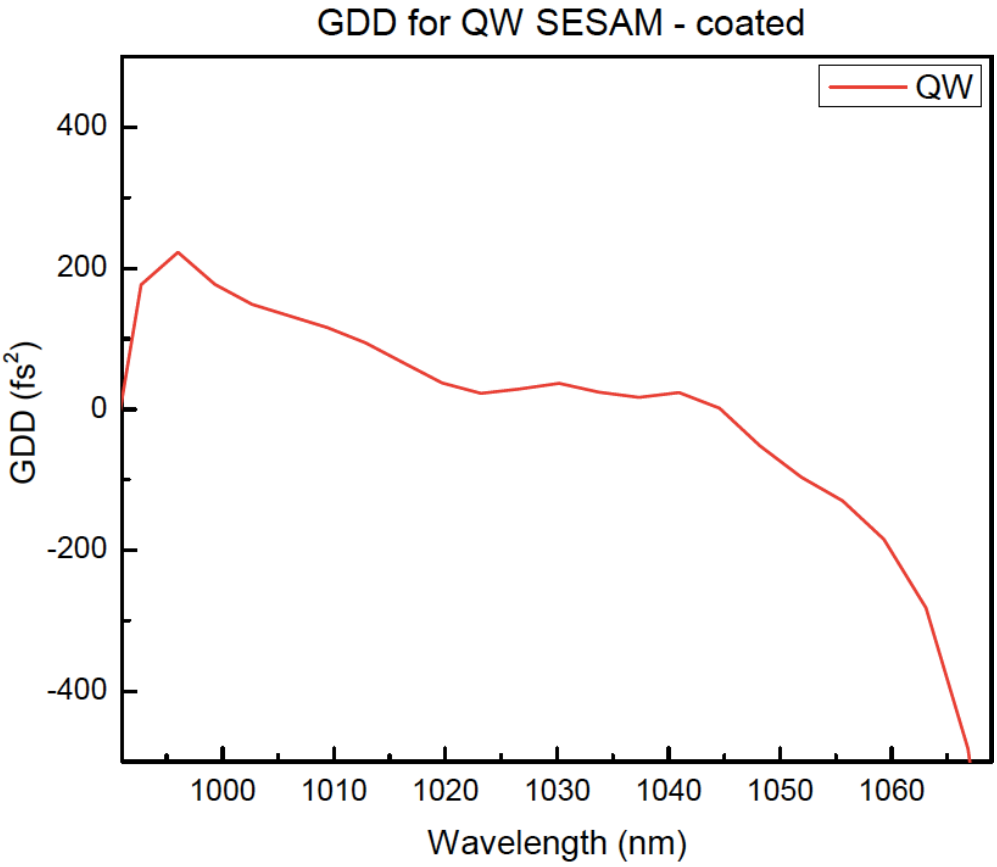

Figure 3.15 : GDD profile for a QW-based SESAM around the absorption wavelength (1030nm)

3.9 Mode-locking results

With the different parameters for the SESAM (recovery time, GDD, reflectivity) verified to be able to support ultra-short pulses, we attempted mode-locking the SESAM in a symmetric ring cavity (as explained in the previous chapter). A minimum pulse duration of 128fs was obtained with the gain element at 25^0C and the SESAM chip at 55^0C with an output power of 90mW per output beam for a pump power of 22W. Figure 3.16 shows the non-collinear SHG autocorrelation trace of the output fitted to a 128fs

$sech^2$ pulse shape. To the best of our knowledge, this is one of the shortest pulse durations reported in literature.

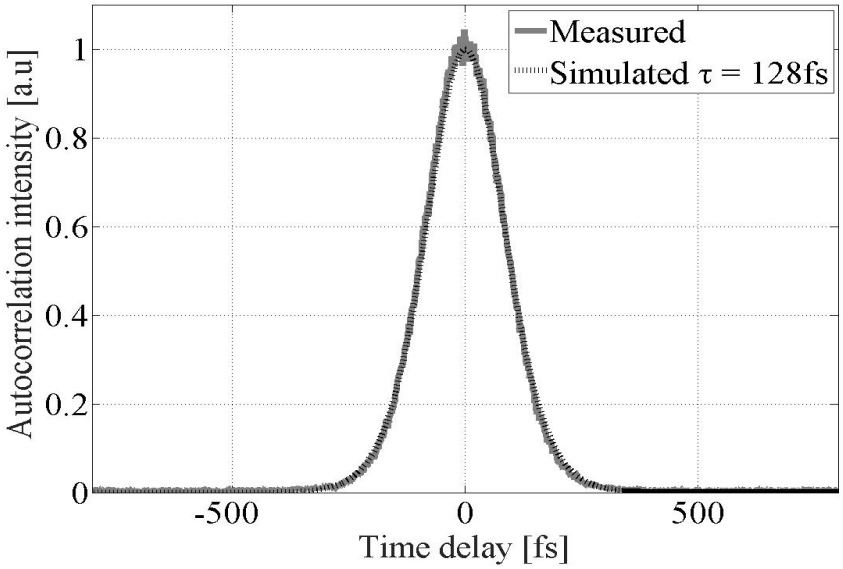

Figure 3.16 : SHG autocorrelation trace of the output of the cavity fitted to a sech2 pulse shape. Pulses as short as 128fs are obtained. (taken from [25])

References:

[1] Waldburger, Dominik, Sandro M. Link, Cesare G. Alfieri, Matthias Golling, and Ursula Keller. "High-power 100-fs SESAM-modelocked VECSEL." In *Advanced Solid State Lasers*, pp. ATu1A-8. Optical Society of America, 2016.

[2] Alfieri, C. G. E., A. Diebold, F. Emaury, E. Gini, C. J. Saraceno, and U. Keller. "Improved SESAMs for femtosecond pulse generation approaching the kW average power regime." *Optics Express* 24, no. 24 (2016): 27587-27599.

[3] Head, C. R., Alexander Hein, Andrew P. Turnbull, Markus Polanik, Edward A. Shaw, Theo Chen Sverre, Peter Unger, and Anne C. Tropper. "High-order dispersion in sub-200-fs pulsed VECSELs." In *SPIE LASE*, pp. 973408-973408. International Society for Optics and Photonics, 2016.

[4] Lauraina, Alexandre, Declan Marahb, Robert Rockmorea, John G. McInerneyb, Jorg Hader, Antje Ruiz Perezc, Stephan W. Kocha, Wolfgang Stolzc, and Jerome V. Moloneya. "High power sub-200fs pulse generation from a colliding pulse modelocked VECSEL." In *Proc. of SPIE Vol*, vol. 10087, pp. 100870E-1. 2017.

[5] Baker, Caleb W., Maik Scheller, Alexandre Laurain, Antje Ruiz-Perez, Wolfgang Stolz, Sadhvikas Addamane, Ganesh Balakrishnan, Stephan W. Koch, R. Jason Jones, and Jerome V. Moloney. "Multi-Angle VECSEL Cavities for Dispersion Control and Peak-Power Scaling." *IEEE Photonics Technology Letters* 29, no. 3 (2017): 326-329.

[6] Lee, Bor-Lin, and Ching-Fuh Lin. "Wide-range tunable semiconductor lasers using asymmetric dual quantum wells." *IEEE Photonics Technology Letters* 10, no. 3 (1998): 322-324.

[7] Hoogland, S., S. Dhanjal, A. C. Tropper, J. S. Roberts, R. Haring, R. Paschotta, F. Morier-Genoud, and U. Keller. "Passively mode-locked diode-pumped surface-emitting semiconductor laser." *IEEE Photonics Technology Letters* 12, no. 9 (2000): 1135-1137.

[8] Garnache, A., S. Hoogland, A. C. Tropper, I. Sagnes, G. Saint-Girons, and J. S. Roberts. "Sub-500-fs soliton-like pulse in a passively mode-locked broadband surface-emitting laser with 100 mW average power." *Applied Physics Letters* 80, no. 21 (2002): 3892-3894.

[9] Klopp, P., U. Griebner, M. Zorn, and M. Weyers. "Pulse repetition rate up to 92 GHz or pulse duration shorter than 110 fs from a mode-locked semiconductor disk laser." *Applied Physics Letters* 98, no. 7 (2011): 071103.

[10] Quarterman, Adrian H., Keith G. Wilcox, Vasilis Apostolopoulos, Zakaria Mihoubi, Stephen P. Elsmere, Ian Farrer, David A. Ritchie, and Anne Tropper. "A passively mode-

locked external-cavity semiconductor laser emitting 60-fs pulses." *Nature Photonics* 3, no. 12 (2009): 729-731.

[11] Gaafar et al., “Mode-locked semiconductor disk lasers”, Advances in Optics and Photonics, Vol. 8 No.3 (Sept. 2016)

[12] Arthur, John R. "Molecular beam epitaxy." *Surface science* 500, no. 1 (2002): 189-217.

[13] Schuler-Sandy, T., S. Myers, B. Klein, N. Gautam, P. Ahirwar, Z-B. Tian, T. Rotter, G. Balakrishnan, E. Plis, and S. Krishna. "Gallium free type II InAs/InAsxSb1-x superlattice photodetectors." *Applied Physics Letters* 101, no. 7 (2012): 071111.

[14] Ahirwar, Pankaj, Thomas J. Rotter, Darryl Shima, Nahid A. Jahan, Stephen PR Clark, Sadhvikas J. Addamane, Ganesh Balakrishnan et al. "Growth and optimization of 2-μm InGaSb/AlGaSb quantum-well-based VECSELs on GaAs/AlGaAs DBRs." *IEEE Journal of Selected Topics in Quantum Electronics* 19, no. 4 (2013): 1700611-1700611.

[15] Keller, Ursula, Kurt J. Weingarten, Franz X. Kartner, Daniel Kopf, Bernd Braun, Isabella D. Jung, Regula Fluck, Clements Honninger, Nicolai Matuschek, and J. Aus Der Au. "Semiconductor saturable absorber mirrors (SESAM's) for femtosecond to nanosecond pulse generation in solid-state lasers." *IEEE Journal of selected topics in QUANTUM ELECTRONICS* 2, no. 3 (1996): 435-453.
.
[16] Cotal, Hector, Chris Fetzer, Joseph Boisvert, Geoffrey Kinsey, Richard King, Peter Hebert, Hojun Yoon, and Nasser Karam. "III–V multijunction solar cells for concentrating photovoltaics." *Energy & Environmental Science* 2, no. 2 (2009): 174-192.

[17] Selvig, Espen. "Molecular beam epitaxial growth and characterization of GaInAsSb/AlGaAsSb mid-infrared laser structures." PhD diss., Fakultet for informasjonsteknologi, matematikk og elektroteknikk, 2004.

[18] Charpentier, Christophe. "Molecular beam epitaxial growth of high-quality Sb-based III/V semiconductor heterostructures." PhD diss., 2014.

[19] RHEED ; World Heritage Encyclopedia Edition.

[20] Ahirwar, Pankaj. "Design, growth and optimization of 2-μm InGaSb/AlGaSb quantum well based VECSELs on GaAs/AlGaAs DBRs." PhD diss., 2013.

[21] Rinaldi, Fernando. "MBE growth and characterization of multilayer structures for vertically emitting laser devices." PhD diss., Universität Ulm, 2009.

[22] Ungier, L., J. R. Arthur, H. M. Yoo, and T. G. Stoebe. "Aluminum-oven emergency power supply for molecular-beam epitaxy system." *Journal of Vacuum Science & Technology B* 10, no. 3 (1992): 1226-1227.

[23] Beere, H. E., J. R. Freeman, O. P. Marshall, C. H. Worrall, and D. A. Ritchie. "The reproducibility and transferability of a THz quantum cascade laser design between two MBE growth manufacturers' platforms." *Journal of Crystal Growth* 311, no. 7 (2009): 1923-1928.

[24] Cymru, Ptifysgol. "Round-Up." *Phys. World* 11, no. 6 (1998): 54.

[25] Laurain, Alexandre, Robert Rockmore, Hsiu-Ting Chan, Jorg Hader, Stephan W. Koch, Antje Ruiz Perez, Wolfgang Stolz, and Jerome V. Moloney. "Pulse interactions in a colliding pulse mode-locked vertical external cavity surface emitting laser." *JOSA B* 34, no. 2 (2017): 329-337.

[26] Hader, Jorg, H-J. Yang, M. Scheller, Jerome V. Moloney, and Stephan W. Koch. "Microscopic analysis of saturable absorbers: Semiconductor saturable absorber mirrors versus graphene." *Journal of Applied Physics* 119, no. 5 (2016): 053102.

Chapter 4 : Lifetime of QW-based SESAMs

As described in Chapter 3, we were able to successfully realize the growth and characterization of InGaAs QW-based SESAMs able to support pulses as short as 128fs. Although this is one of the shortest pulse durations realized from a mode-locked VECSEL system, for this system to be commercially relevant in high-power technologies using SESAMs, the temporal stability of the mode-locked state is significant. For the sustainability of short pulses in the femtosecond regime, a robust SESAM design that can tolerate high intracavity peak powers is required. Moreover, the power scalability of thin-disk lasers by increasing the spot size on the gain region places more restrictions on an appropriate SESAM design. Therefore, it is critical that SESAMs that can support ultra-short pulse durations also have long lifetimes and low nonsaturable losses to avoid thermal effects. This chapter focuses on quantifying the mode-locking lifetime of InGaAs QW-based SESAMs in the femtosecond regime.

4.1 Degradation of output power in QW-based SESAMs

Although the SESAMs characterized in the previous chapter were able to support some of the shortest pulse durations reported to date, it is found that they exhibit extremely poor power stabilities over time. Figure 4.1 shows the gradual degradation of an InGaAs-QW based SESAM mode-locked with a 128fs pulse in a symmetric ring cavity. The average output power decreases continuously for ~30min before the mode-locking state is lost altogether. Also, the degradation is specific to pulses with shorter durations (<500fs) and does not occur when the pulse duration is longer (even with higher average powers).

Another interesting aspect is that when this process occurs, the decay in output power is always accompanied by a visible green emission from the SESAM chip. It is to be noted that the degradation data shown below is for an InGaAs-QW based SESAM with a 29-pair DBR, 22m GaAs spacer between the DBR and the absorber and a 7nm GaAs cap. The initial rate of degradation in the output power can be calculated to be 6.5%/min which gradually decreases to 0.8% after 10min. These are rather high degradation rates and the effective lifetime is substantially shorter than required for commercial technologies. [1] Therefore, it is critical to understand the decay mechanism in play here and potentially propose a solution to increase SESAM lifetimes. Before performing any further studies to determine the decay mechanism, we decided to investigate any past work that has been done towards solving this issue. This is summarized in the following section.

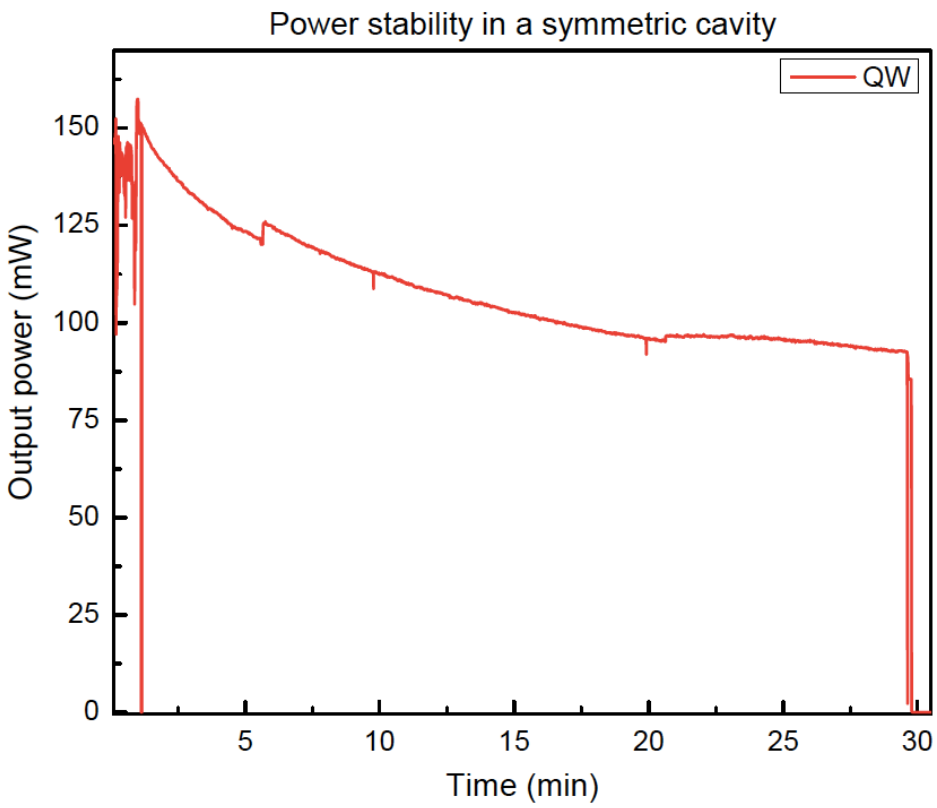

Figure 4.1 : Output power stability for a InGaAs QW-based SESAM mode-locked with a 128fs pulse in a ring cavity

4.2 Possible mechanism causing SESAM degradation

As the use of mode-locked systems has become more technologically viable in the recent years, there has been an increased interest in studying degradation and damage thresholds in SESAMs. [2-9]. Among all the studies carried out to measure the damage threshold of InGaAs QW-based SESAMs, it is fairly widely accepted that the damage mechanism is dominated by two-photon absorption (TPA), especially in the case of femtosecond pulses. TPA is a non-linear process by which an atom is excited by two photons, the sum of whose energies corresponds to an excited state of the atom [10]. This phenomenon occurs with significant rates only at high optical intensities- for instance in

mode-locked systems with femtosecond pulses - because the absorption coefficient is proportional to the optical intensity.

The theory of TPA causing the damage certainly explains the observation of visible green emission from the SESAMs during the process of degradation. However, although most studies on SESAM damage agree on the mechanism being TPA, there is still a debate on a few other aspects of the degradation process. While some results show TPA is more dominant in the DBR region [2,3], some report that it is the QW that is being affected [6]. Moreover, regardless of the location of damage, there hasn't been a comprehensive study conducted to investigate the physical damage that TPA causes. Therefore, the rest of this chapter focuses on studying the effect of different SESAM parameters on the damage threshold and examining the physical damage caused by TPA.

4.3 Pulsed Photoluminescence to measure SESAM degradation

In order to quantify and optimize the lifetime of SESAMs and study the effect of various cavity conditions such as the incident fluence and the dielectric coating, the output power stability measurement shown in the figure 4.1 would have to be repeated on a number of samples. This is inherently time-consuming as it takes a substantial amount of time to optimize the mode-locking state in the cavity for each sample. Therefore, we have used a pulsed PL experiment using femtosecond pulses (~100fs @ 780nm) from a mode-locked laser setup to characterize the damage mechanism on various samples in a timely manner. Moreover, this setup offers the flexibility of easily changing the incident fluence on the

SESAMs to find the damage threshold for each sample. It also closely simulates the conditions for the SESAM in a mode-locked state in the femtosecond regime. For these measurements, we define "damage" of a SESAM as an irreversible decrease in the PL intensity over time. It is to be noted that a decrease in PL intensity over time does not necessarily imply a damage to the saturable absorber (QW here) as the PL is heavily modulated by the DBR layers and this contributes to the PL intensity. The incident fluence is measured using a power meter before the measurement is started and changed when required by controlling the driver current to the laser. Once the pulses are incident on the sample, the PL measurement is repeated every 30sec (each measurement takes ~1sec) over 5min and each measurement is recorded to analyze the effect on PL intensity. Once a spot on the sample is damaged, the SESAM stage is moved either in the x- or the y-direction to an undamaged spot for the next measurement.

4.4 Dependence of SESAM degradation on incident fluence

Figure 4.2 shows the PL degradation of an InGaAs-QW based SESAM (same structures used as in output power stability measurements) for different incident average fluences of 10mW, 50mW and 90mW. The degradation is non-existent with an incident fluence of 10mW but as the fluence was increased to ~30mW, there was substantial PL degradation (~10% of original intensity for 2^{nd} measurement) between each measurement. It is evident from the measurements at 50 and 90mW that the PL intensity decay is faster with higher incident fluence. Also, it is interesting to note that the trend in degradation is not linear and slows down over time. This is identical to the trend in output power decay as seen in the previous measurement in a mode-locked cavity.

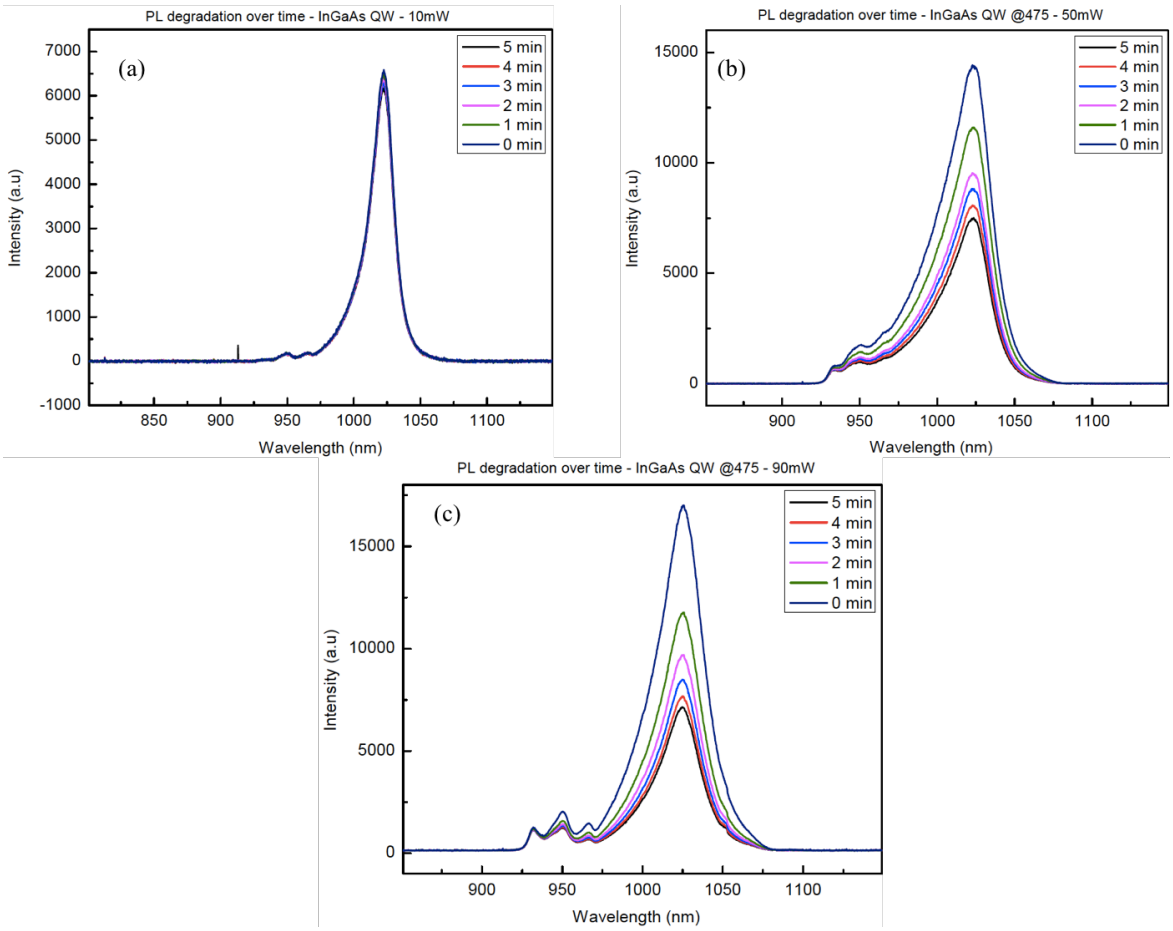

Figure 4.2 : Degradation in PL intensity for InGaAs QW-based SESAMs for different incident fluences – 10mW (a) ; 50mW (b) ; 90mW (c).

In order quantify the decay in PL intensity observed in the previous figure, the PL peak intensities for each measurement are determined, normalized to the original intensity (intensity at t=0 min) and plotted as a function of time in figure 4.3.

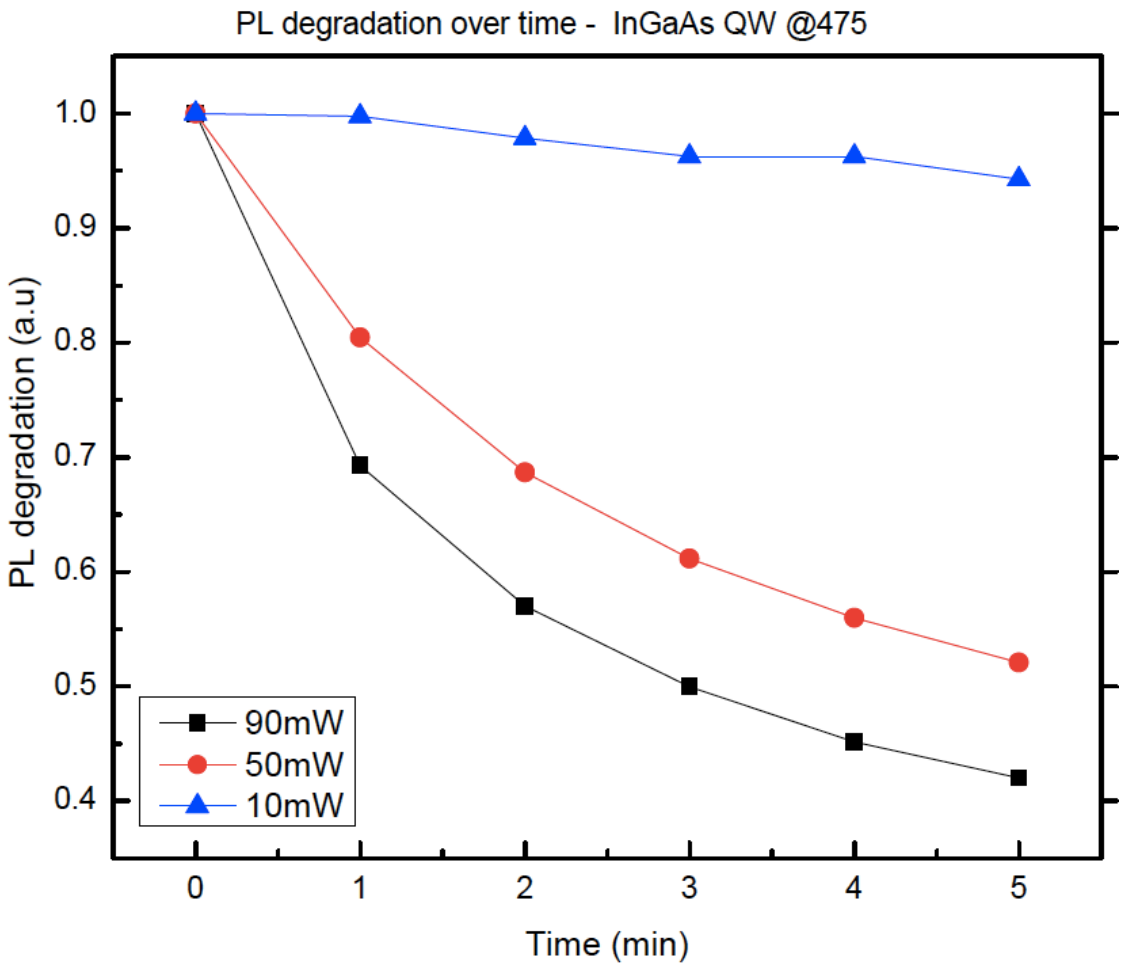

Figure 4.3 : Degradation in PL peak intensities (normalized to the first measurement) over time for different incident fluences.

The decay in PL peak intensities can be fit (not shown) to an exponential decay function (with an offset)

$$y = y_0 + A_1 e^{-\frac{(x-x_0)}{\tau}} \tag{4.1}$$

where y_0 is the y-offset ; x_0 is the center ; A_1 is the amplitude and τ is the decay time constant. The relevant parameter for the PL degradation is τ which would be the time taken for the PL peak intensity to reduce to 1/e (36.8%) of the original value. At 10mW, the trend in

degradation is not a good fit for the equation above. However, the time constants (τ) for incident fluences of 50mW and 90mW can be shown to be 2.27 min and 1.47 min respectively. Therefore, the rate of degradation increases by a factor of ~1.5 for an increase in incident fluence from 50 to 90mW.

4.5 Dependence of SESAM degradation on cap thickness

At this point in the study, we suspected that the PL decay and consequently, the decay in SESAM output power was based on degradation of the InGaAs QW by oxidation, due to its close proximity to the semiconductor-air interface(7nm). This mechanism has been known to cause catastrophic optical damage in InGaAs QW lasers through facet oxidation or defect formation under high-power operation [11-14]. To test this hypothesis, we wanted to examine if the rate of degradation would depend on the proximity of the InGaAs QW to the semiconductor-air interface. Therefore, we performed the PL decay test with 3 different SESAM structures with identical GaAs/AlAs DBRs, 22nm GaAs spacer layers and InGaAs QW absorber but varying cap thicknesses. (3nm, 5nm and 7nm). Figure 4.4 shows the summary of results from this measurement. The top and bottom rows of plots are essentially the same data presented in two different ways. The top row shows three plots – 1(a), 1(b) and 1(c) - one for each cap thickness (3nm, 5nm and 7nm) and within each plot, the incident fluence is varied from 20mW to 50mW. On the other hand, the bottom row shows three plots – 2(a), 2(b) and 2(c) - one for each incident fluence (20, 30 and 50mW) and within each plot, the cap thickness is varied between 3nm, 5nm and 7nm. As in the previous experiment, the normalized PL peak intensity is tracked over time for different cap

thicknesses and different incident fluences. In general, the trend in the PL decay shows that the degradation rate indeed increases with decreasing cap thickness and increasing incident fluence. This supports our hypothesis that the damage mechanism is related to the distance between the InGaAs QW and the air-semiconductor interface.

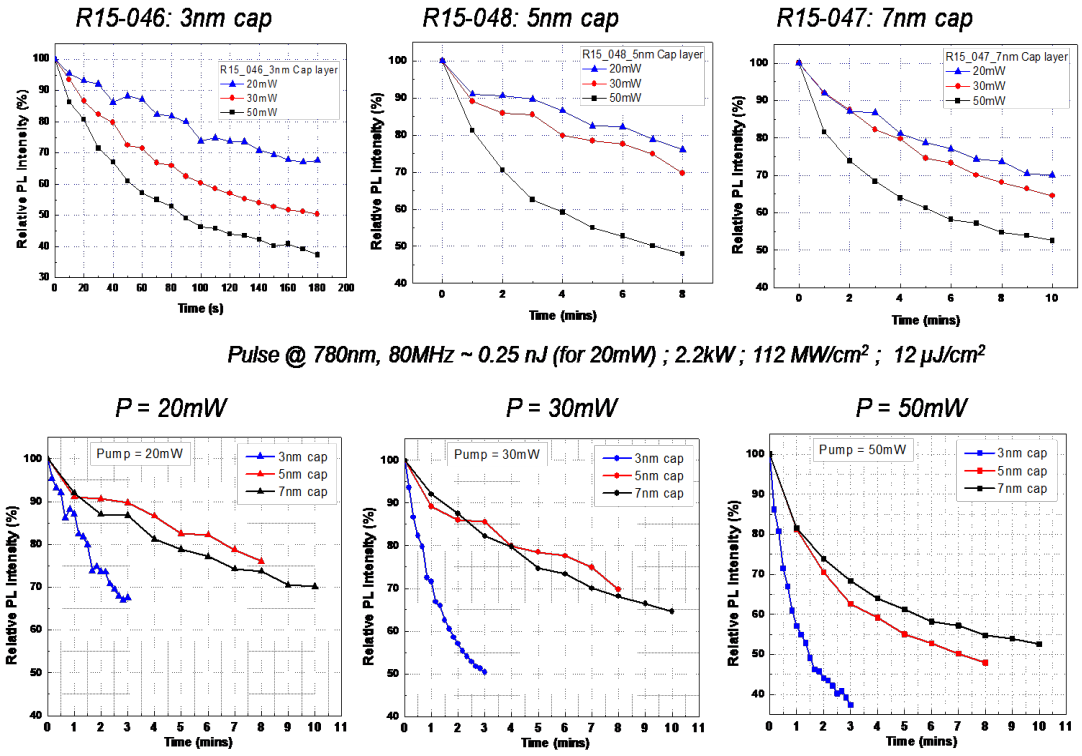

Figure 4.4 : PL decay test is performed on InGaAs QW-based SESAMs with different GaAs cap thicknesses (3nm, 5nm and 7nm). Row (1) shows 3 plots (a, b, c), each for a specific cap thickness, and the incident fluence is varied within each plot. Row (2) shows 3 plots (a,b,c) each for a specific incident fluence and all three caps thicknesses are tested with the same incident fluence.

In order to quantify the effect of the GaAs cap thickness on the rate of degradation, we chose the results for the three different cap thicknesses (3, 5 and 7nm) with the highest incident fluence of 50mW (shown in Fig 2(c) above). This data is fitted to the exponential decay function described above to compute the dependence of the decay time constant (τ)

on the cap thickness. The exponential decay fit is shown in figure 4.5 for a GaAs cap thickness of 3nm (a), 5nm(b) and 7nm(c). From the fitting parameters, the decay time constant (τ) can be calculated to be 0.927, 2.536 and 2.682 min for 3,5 and 7nm caps respectively. From this, it is evident that the rate of degradation decreases as the distance between the absorber and the semiconductor-air interface increases. It is also interesting to note that the decrease in the decay time constant with decreasing cap thickness is not linear but rather exponential in nature.

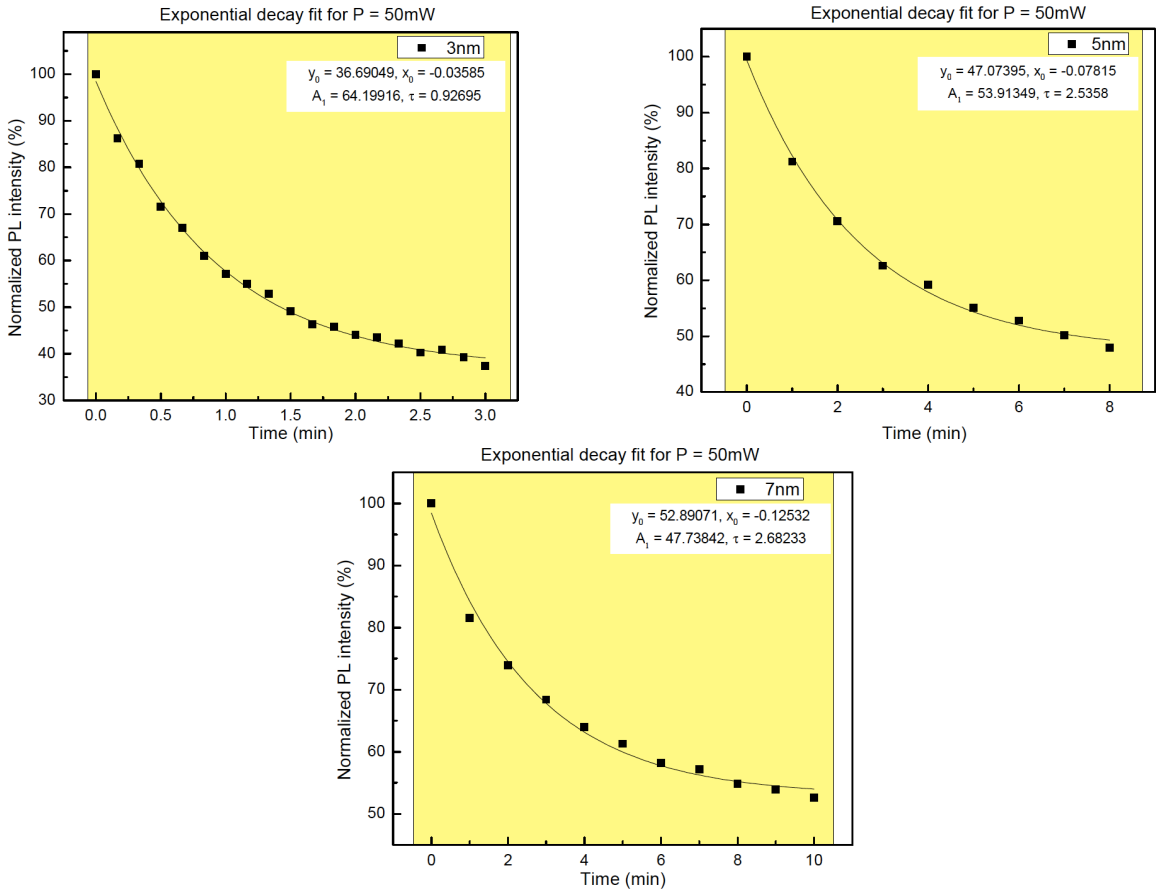

Figure 4.5 : Exponential decay (with offset) fit for InGaAs QW-based SESAMs with varying cap thickness – 3nm(a) ; 5nm(b) and 7nm (c).

4.6 Effect of dielectric coating on SESAM degradation

The effect of the GaAs cap thickness on the degradation rate of SESAMs (as shown in the study above) certainly seems to support the theory that SESAM degradation is related to a certain extent to damage caused to the absorber layer. Assuming that high fluences cause oxidation of the absorber, it becomes critical to understand the effect of the dielectric coating (Ta_2O_5/SiO_2) that is deposited to help flatten the GDD profile on the degradation of the SESAM. The presence of an oxide layer close to the QW might potentially provide more or less access to oxygen and consequently modify the degradation rate. In order to confirm this, the PL degradation test is performed on coated and uncoated InGaAs-QW based SESAMs. To avoid the effects of growth drifts, the devices chosen for this study are from the same wafer and both devices were located at identical distances from the center of the wafer. Before measuring the degradation rates, the effect of the coating on the original PL is studied. Figure 4.6 shows PL measurements at room temperature for coated and uncoated QW SESAMs at the highest fluence allowed by our setup (90mW). As mentioned before, multiple peaks observed between 930-950nm are effects of PL modulation by the DBR. The QW peak is observed at ~1030nm and the PL intensity for the coated SESAM is 2.5 times higher than the uncoated SESAM. The increase in PL intensity is also accompanied by a corresponding substantial increase in the FWHM by ~17nm. The increase in PL intensity could be attributed to an increased optical confinement by deposition of the coating. The probability of carriers being lost to surface states is effectively lowered leading to increased recombination rate in the QW.

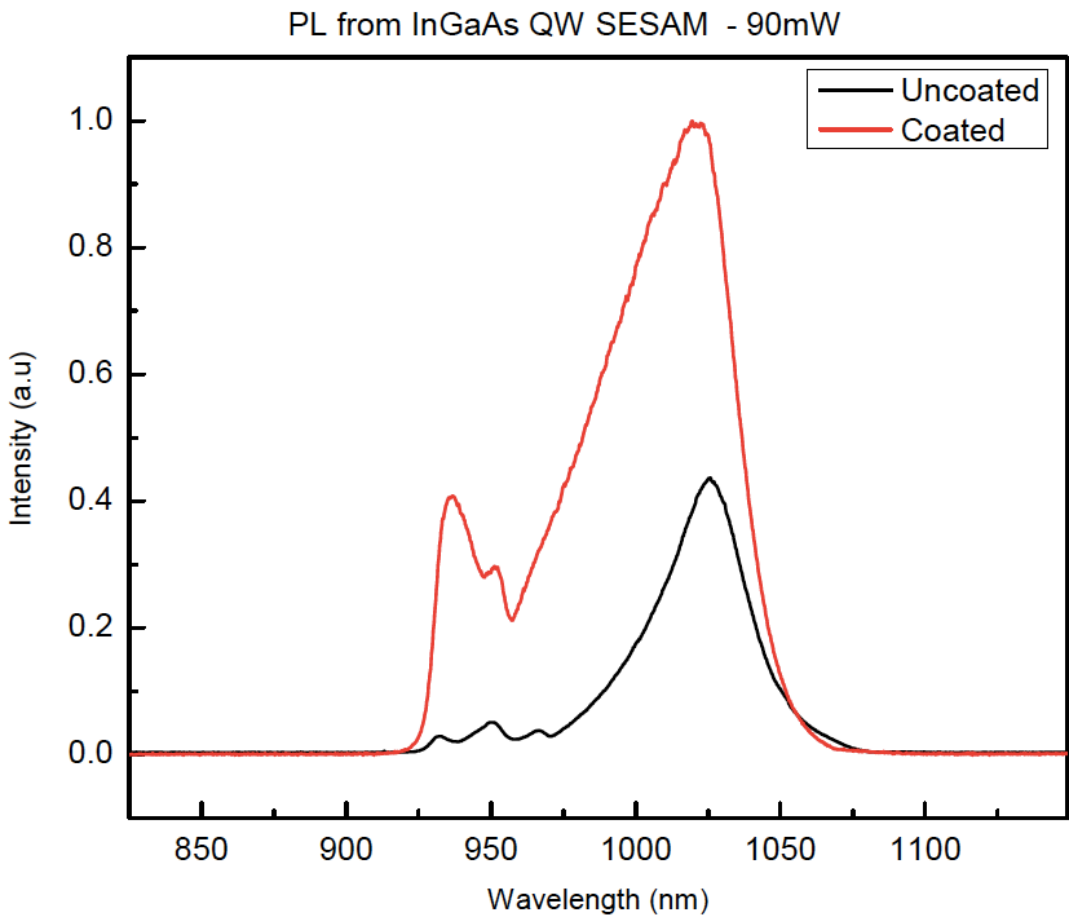

Figure 4.6 : PL measurements on coated vs uncoated InGaAs QW-based SESAM at a fluence of 90mW. The PL intensity increases substantially after the coating is deposited.

Figure 4.7 shows the decay in PL peak intensity at a fluence of 90mW for both coated and uncoated SESAM samples. The peak intensity values are again normalized to the peak intensity at 0 min. It is found that the rate of degradation is higher with the coated SESAMs when compared to the uncoated SESAMs. From the slopes of the lines connecting each measurement, a substantial difference can be observed in the initial degradation rate between the two samples. When fit to a exponential decay function (refer to equation (1) above), the decay constant (τ) is found to decrease from 1.47 min for a uncoated sample to 0.85 min for

a coated one. This result also seemed to substantiate the claim that the degradation of SESAMs might be caused by a damage (possibly oxidation) of the QW.

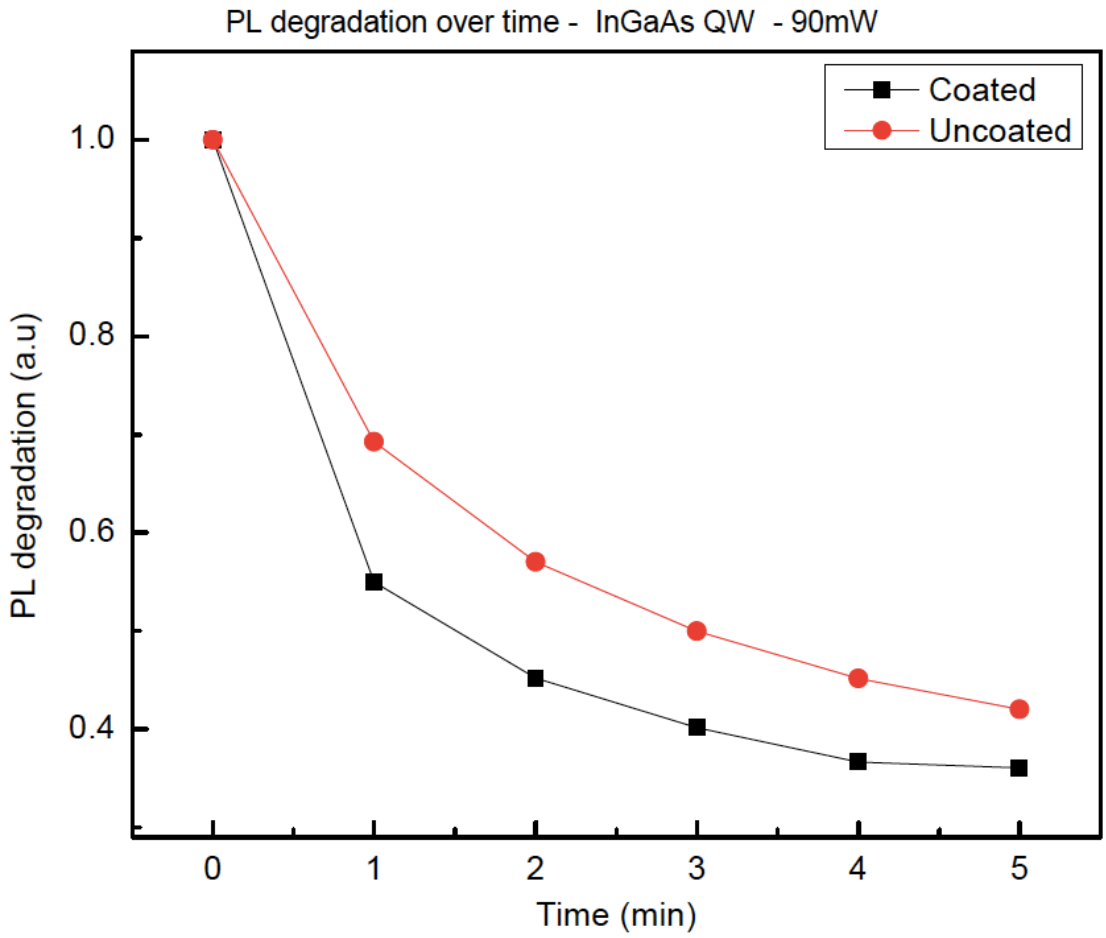

Figure 4.7 : PL peak intensity degradation values compared between coated and uncoated samples. The degradation rate seems to be higher for a coated device.

4.7 TEM analysis of SESAM damage

Damage threshold measurements described earlier in this chapter based on incident fluence, cap thickness and presence of dielectric coating layer seem to suggest that the damage mechanism is related to degradation of the absorber. In order to confirm this

hypothesis and to observe the physical damage to the SESAMs, we have performed a cross-sectional transmission electron microscopy (TEM) analysis of "damaged" versus as-grown samples. The "damaged" devices are standard InGaAs QW-based SESAMs described in the previous chapter (29.5 pair AlAs-GaAs DBR/22nm GaAs spacer/7nm GaAs cap) used in a ring cavity to mode-lock a 1030nm VECSEL with ~100fs pulses for long periods of time. Once a certain spot on the sample is degraded i.e. the output power decays and the mode-locking state is unrecoverable, the sample is moved in the x- or y- direction to a different spot. This process is repeated until the entire area of the sample is used. This ensures that any random cross-section of the sample observed would show the effects of the damage mechanism. The damaged and as-grown SESAMs are cross-sectioned with a focused ion beam (FIB) lift out using a FEI Helios 450 DIB system. The TEM images were taken using an FEI Tecnai F20 equipped with HAADF STEM detector. Furthermore, to detect any possible oxidation, the different epitaxial layers are also analyzed using electron dispersive spectroscopy (EDS) to determine the composition of various regions.

Figure 4.8 shows a comparison of cross-sectional TEM images of the as-grown and damaged SESAMs. The DBR and absorber layers are appropriately labeled on the figure. At this lower magnification, the effects of the damage are seen mainly in the DBR section. Within the DBR itself, particularly the top-section of the GaAs/AlAs layers (close to the air-semiconductor interface) appear damaged. It is interesting to observe that the overall damage profile seen in (b) appears similar to laser-induced damage and resembles a typical laser-beam profile. However, since the absorber layers (GaAs spacer/InGaAs QW/GaAs cap) are not visible, we cannot comment on any degradation in these layers at this point.

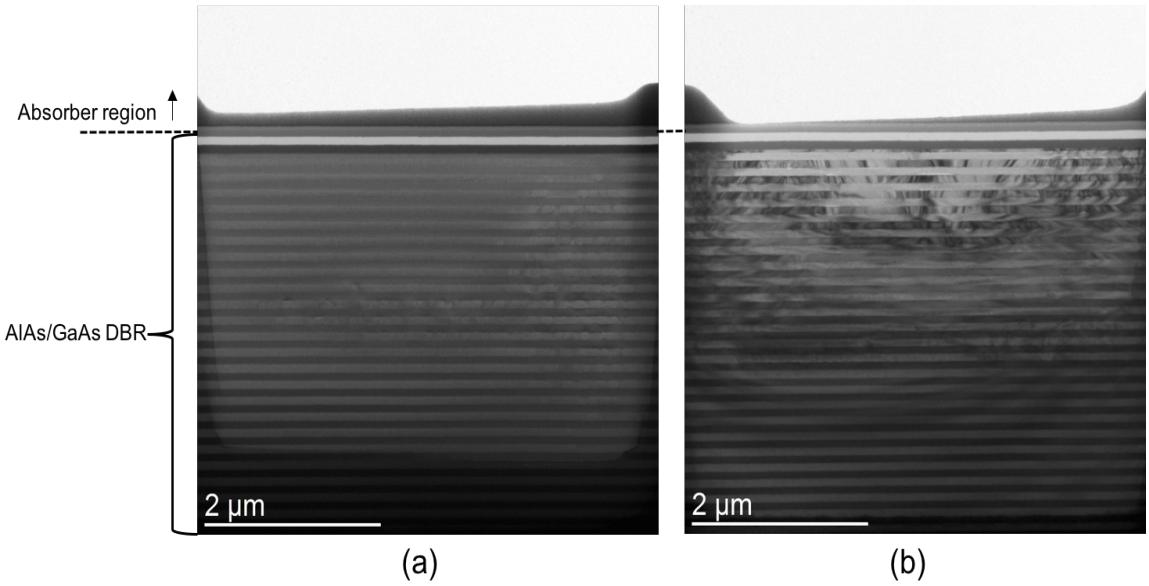

Figure 4.8 : Cross-sectional TEM images of as-grown and "damaged" SESAMs. The degradation observed in the damaged SESAM is confined to the top DBR layers.

In order to study the damage profile in more detail, TEM images at a higher magnification focusing on the top-section of the DBR and the absorber layers are analyzed. Although the absorber region is still not resolved, the last few pairs of the DBR are clearly disfigured and the extent of damage decreases going away from the air-semiconductor interface in figure 4.9. At the outset, it seems like the damage could be confined to one of the layers of the DBR. However, this would have to be confirmed by a comprehensive elemental analysis using EDS for both layers. Using higher magnification images, the extent of damage, if any, in the absorber region and the damage profile are studied in more detail in the following sections.

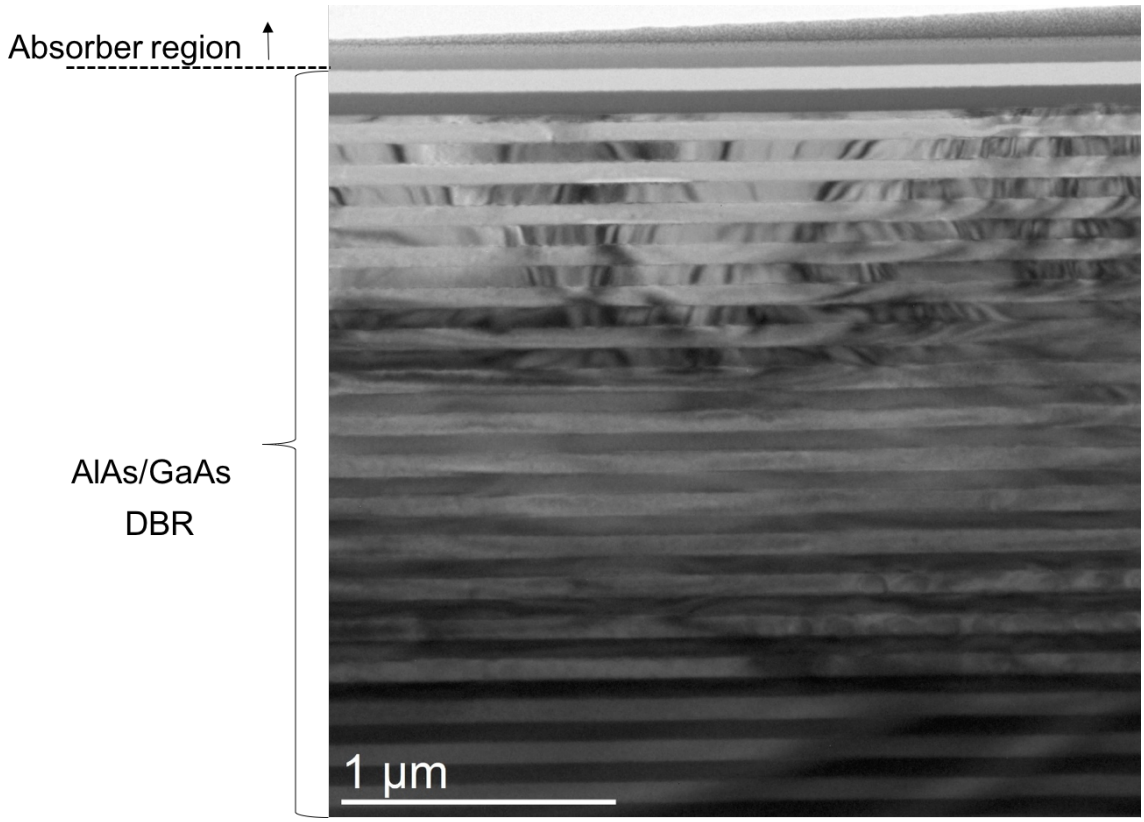

Figure 4.9 : Cross-sectional TEM image at high-magnification showing "damaged" SESAM. The extend of degradation in the DBR layers decreases going away from the semiconductor-air interface.

Figure 4.10 below shows DF-STEM images of the absorber region (spacer, QW and cap) with the topmost GaAs/AlAs pair of the 29.5 pair DBR for both the as-grown and the damaged SESAM. Contrary to our previous assumptions, the absorber region, including the InGaAs QW is unaffected by the SESAM degradation and seems to be in pristine condition. It is also interesting to note that the GaAs layers on either sides of the QW appear to be free of any damage. On the other hand, the damaged SESAM distinctly shows some material degradation in the final AlAs layer of the DBR. In order to determine if this appearance of

damage leads to any compositional variation, an EDS analysis of the different layers shown in figure 4.10 is performed.

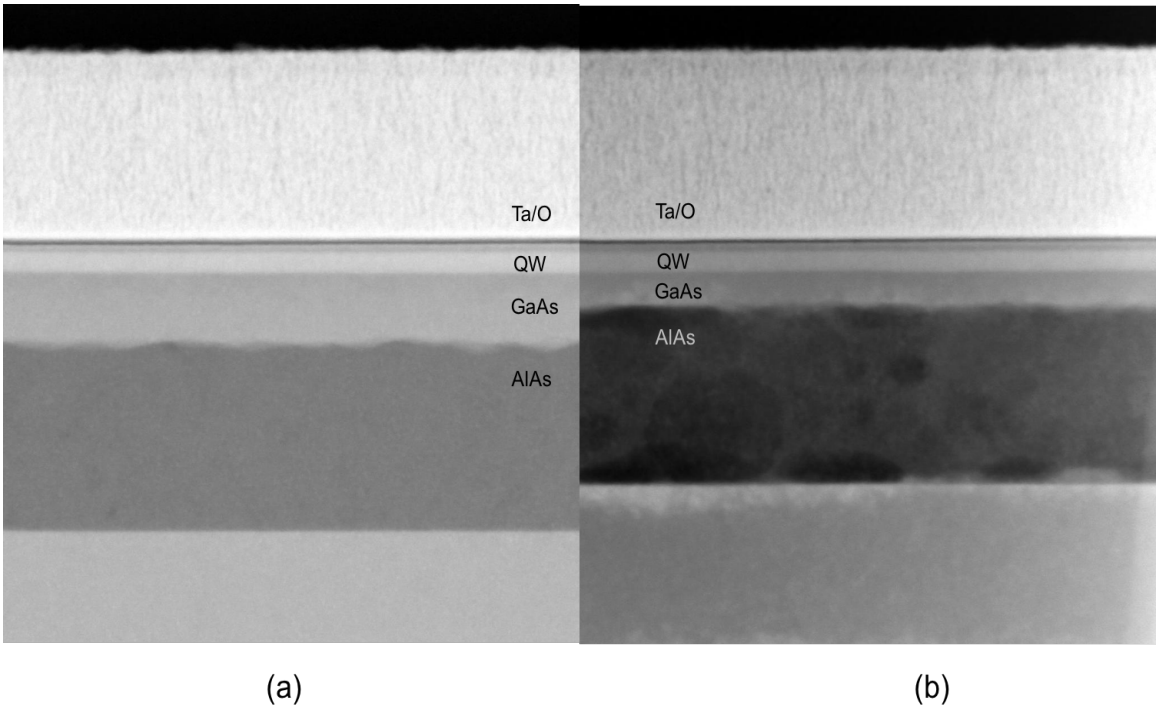

Figure 4.10 : DF-STEM images of the absorber region and last DBR-pair of the as-grown and damaged SESAM. While the absorber region seems unaffected, distinct damage is observed in the AlAs region of the damaged SESAM.

Figure 4.11 shows EDS analysis of the DF-STEM images above along a line through the absorber region up to the first DBR pair. The Ta_2O_5 anti-reflection coating, GaAs cap layer, InGaAs QW, GaAs spacer layer (in that order moving down from the air-semiconductor interface) are identical between the two samples. However, the first AlAs layer under the absorber region on the damaged SESAM shows traces of oxygen (red trace on figure) hinting towards oxidation of the AlAs layer. This result clearly confirms that

SESAM degradation in a mode-locked state using ultra-short pulse durations are caused by damage to the AlAs layers in the DBR through oxidation of these layers. It also explains the visible damage observed in the GaAs layers in the low-magnification TEM images (figure 4.8(b) and 4.9). Post-oxidation of the AlAs layers, the lattice-parameters of these layers change and this induces a strain-field in the DBR. This leads to the visible damage observed in the GaAs layers.

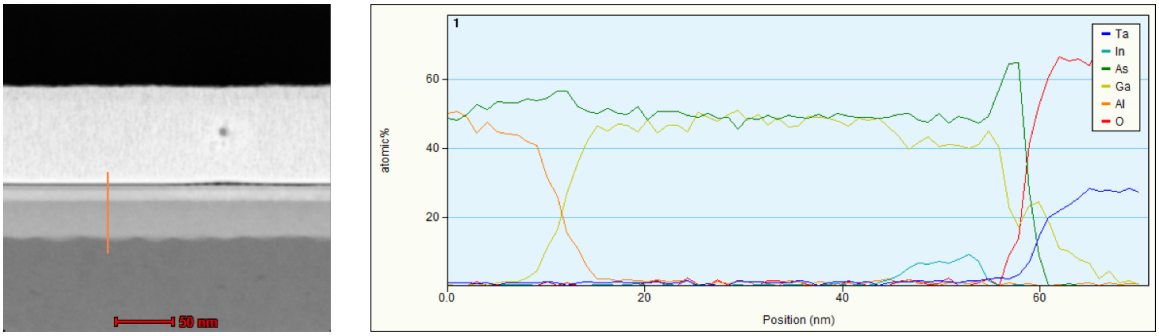

(a)

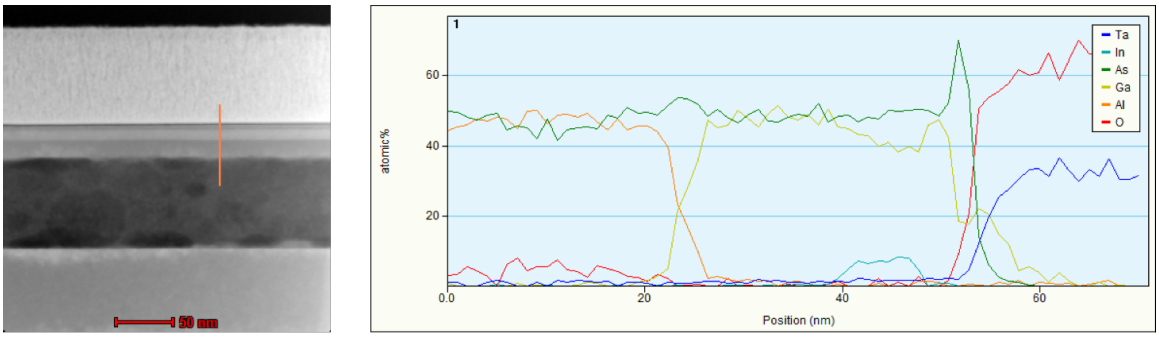

(b)

Figure 4.11 : EDS analysis of the DF-STEM images of the absorber region for both the "as-grown" and the damaged SESAM. The damaged sample shows slight traces of oxidation in the AlAs layer under the absorber region.

4.8 Explanation for SESAM damage observed from pulsed PL and TEM

Assuming TPA as the dominant mechanism, the two main factors that need to be explained from the degradation studies are:

- The physical parameter (incident power, field intensity, temperature etc) causing TPA
- The location of damage

From the TEM results, it is found that the damage profile closely resembles a laser beam-induced damage. Also, as mentioned earlier, the degradation process only occurs with ultra-short pulse durations (<300fs) and does not occur with longer pulse durations even with higher average powers. These two factors seem to suggest that the damage mechanism is related more to the field intensity than the incident average power (and consequently, thermal effects). This relation between the damage threshold and the field intensity explains the dependence of the SESAM degradation on incident fluence, cap thickness and the AR coating. As explained in previous sections, these three parameters have a distinct effect on the degradation. In order to explain their effect on degradation, it is critical to understand the effect of varying these three parameters on the field strength in the DBR region. On closer investigation, it is found that the increase in fluence, decrease in cap thickness and the presence of the AR coating effectively increase the field intensity in the DBR region, thus accelerating the SESAM damage.

The second result to be explained is the location of the damage i.e. oxidation of the AlAs layers as revealed by EDS analysis. Assuming TPA as the dominant mechanism, the effect of TPA on any material can be quantified based on its TPA co-efficient β. Higher the value of β, higher the effect of TPA on any given material [2]. The TPA co-efficient, in turn, is a function of the band gap of the material and materials with higher band gap energies are less susceptible to TPA [15]. Based on this, the effect of TPA should be considerably higher in the GaAs layer than in the AlAs or the dielectric coating layers [2,6]. However, the TEM images show that the damage might be initiated in the AlAs layer. To explain this, we suspect that the effect of TPA in the GaAs layer causes lattice heating which, in turn, leads to the oxidation of the AlAs layer. The other unknown for this explanation would be the access point for atmospheric oxygen to reach the underlying AlAs layer. Although the pulsed PL experiments seem to be explained by the TEM analysis for degradation, there is still work to be done to understand the mechanism of damage.

References:

[1] K. Weingarten, “private communication,” Time Bandwidth Products, Zurich, Switzerland, 2010

[2] Saraceno, Clara J., Cinia Schriber, Mario Mangold, Martin Hoffmann, Oliver H. Heckl, Cyrill RE Baer, Matthias Golling, Thomas Südmeyer, and Ursula Keller. "SESAMs for high-power oscillators: design guidelines and damage thresholds." *IEEE Journal of Selected Topics in Quantum Electronics* 18, no. 1 (2012): 29-41.

[3] Grange, R., M. Haiml, R. Paschotta, G. J. Spühler, L. Krainer, M. Golling, O. Ostinelli, and U. Keller. "New regime of inverse saturable absorption for self-stabilizing passively mode-locked lasers." *Applied Physics B: Lasers and Optics* 80, no. 2 (2005): 151-158.

[4] Saraceno, Clara J., Oliver H. Heckl, Cyrill RE Baer, Matthias Golling, Thomas Südmeyer, Kolja Beil, Christian Kränkel, Klaus Petermann, Günter Huber, and Ursula Keller. "SESAMs for high-power femtosecond modelocking: power scaling of an Yb: LuScO 3 thin disk laser to 23 W and 235 fs." *Optics express* 19, no. 21 (2011): 20288-20300.

[5] Baer, Cyrill RE, Oliver H. Heckl, Clara J. Saraceno, Cinia Schriber, Christian Kränkel, Thomas Südmeyer, and Ursula Keller. "Frontiers in passively mode-locked high-power thin disk laser oscillators." *Optics express* 20, no. 7 (2012): 7054-7065.

[6]Viskontas, K., K. Regelskis, and N. Rusteika. "Slow and fast optical degradation of the SESAM for fiber laser mode-locking at 1 μm." *Lithuanian Journal of Physics* 54, no. 3 (2014).

[7] Diebold, A., T. Zengerle, C. G. E. Alfieri, C. Schriber, F. Emaury, M. Mangold, M. Hoffmann et al. "Optimized SESAMs for kilowatt-level ultrafast lasers." *Optics express* 24, no. 10 (2016): 10512-10526.

[8] Haiml, M., R. Grange, and U. Keller. "Optical characterization of semiconductor saturable absorbers." *Applied Physics B: Lasers and Optics* 79, no. 3 (2004): 331-339.

[9] Alfieri, C. G. E., A. Diebold, F. Emaury, E. Gini, C. J. Saraceno, and U. Keller. "Improved SESAMs for femtosecond pulse generation approaching the kW average power regime." *Optics Express* 24, no. 24 (2016): 27587-27599.

[10] Kaiser, W., and C. G. B. Garrett. "Two-photon excitation in Ca F 2: Eu 2+." *Physical review letters* 7, no. 6 (1961): 229.

[11] Sin, Yongkun, Nathan Presser, Brendan Foran, Neil Ives, and Steven C. Moss. "Catastrophic facet and bulk degradation in high power multi-mode InGaAs strained

quantum well single emitters." In *SPIE LASE: Lasers and Applications in Science and Engineering*, pp. 719818-719818. International Society for Optics and Photonics, 2009.

[12] Fukuda, Mitsuo, Masanobu Okayasu, Jiro Temmyo, and J. Nakand. "Degradation behavior of 0.98-/spl mu/m strained quantum well InGaAs/AlGaAs lasers under high-power operation." *IEEE Journal of quantum electronics* 30, no. 2 (1994): 471-476.

[13] Sin, Yongkun, Nathan Presser, Brendan Foran, and Steven C. Moss. "Investigation of catastrophic degradation in high power multi-mode InGaAs strained quantum well single emitters." In *Lasers and Applications in Science and Engineering*, pp. 68760R-68760R. International Society for Optics and Photonics, 2008.

[14] Okayasu, Masanobu, Mitsuo Fukuda, Tatsuya Takeshita, Shingo Uehara, and Katsuhiko Kurumada. "Facet oxidation of InGaAs/GaAs strained quantum-well lasers." *Journal of applied physics* 69, no. 12 (1991): 8346-8351.

[15] Van Stryland, Eric W., M. A. Woodall, H. Vanherzeele, and M. J. Soileau. "Energy band-gap dependence of two-photon absorption." *Optics letters* 10, no. 10 (1985): 490-492.

Chapter 5 : InAs submonolayer quantum dot-based SESAMs

The previous chapter showed that in the femtosecond regime, InGaAs QW-based SESAMs exhibit poor temporal stability of the mode-locking state. On investigating the effect of several SESAM characteristics on the degradation, it was found that the damage mechanism seemed to be extremely sensitive to field intensity in the DBR structure. However, prior to the extensive TEM analysis carried out, we suspected that the SESAM degradation could be caused by damage to the QW absorber. Therefore, one approach we took towards solving this problem was to explore different absorbers at 1030nm. Compared to QWs as absorbers, QDots are known to have a number of advantages. Furthermore, the variation in dot sizes causes homogenous broadening which leads to a broadband absorption spectrum. This makes QDot-based SESAMs more probable to be able to support shorter pulses. Therefore, in this chapter, we have explored the use of QDot-based absorber regions to alleviate the degradation of SESAMs at 1030nm and to increase their effective mode-locking lifetimes.

5.1 QDot-based SESAMs for a design wavelength of 1µm

SESAMs with InAs quantum dot absorber regions offer considerably more design freedom than standard QW-based SESAMs. The zero-dimensional nature of QDots leads to a strong localization of the wave function and gives rise to an atom-like density of states. Moreover, control over the density of QDots allows for independent optimization of saturation fluence and modulation depth. For stable modelocking, the SESAM absorber has

to saturate at lower pulse energies than the gain region. In conventional QW SESAMs, this is achieved by strong focusing onto the SESAM (10-40 times smaller area) which introduces restrictions in geometrical size and maximum achievable repetition rate [1]. These limitations can be overcome by employing QDot SESAMs with lower saturation fluence which allow mode-locking with similar mode areas on SESAM and VECSEL. [2,3] This, in turn, allows the integration of the saturable absorber in the gain structure to form what is referred to as the mode-locked integrated external cavity surface-emitting laser (MIXSEL). InAs QDot-based absorbers have been used previously in SESAMs to achieve modelocking at ~960nm and 1250nm. [1-3] However, for a lasing wavelength of 1030nm, the traditional Stranski-Krastonov (SK) QDots would require the use of an AlGaAs matrix which decreases the optical confinement factor. As an alternative to SK QDots, InAs submonolayer (SML) QDots have been of particular interest for high-speed electronic devices including edge-emitting lasers, vertical cavity surface emitting lasers, QDot photodetectors and solar cells in the recent years. [4, 5, 6-12] The emission wavelength for SML QDots can be easily tailored to anywhere in the range of 950-1300nm. They combine high excitonic gain, fast gain recovery and low temperature-stable lasing thresholds (characteristic features of QDots) with the high modal gain of QWs. Given these advantages of SML QDots over the SK QDots, in this chapter we explore the use of submonolayer InAs QDots as saturable absorbers for SESAMs at 1030nm.

5.2 Submonolayer QDots

Self-organized InAs QDots can be realized by either growing in the traditional SK mode or via submonolayer deposition. In the SK growth mode, the QDots are formed by growing a strained epilayer such as 2-3ML of InAs on lattice mismatched GaAs substrates (7.16%lattice mismatch). The initial growth occurs in a layer-by-layer mode and forms a thin wetting layer (1ML or so). However, further InAs deposition past a certain critical thickness causes a large strain accumulation in the epilayer. This, in turn initiates the formation of three-dimensional coherently strained (dislocation-free) islands with the appearance of crystalline facets which help relieve the surface energy of the island. [4,13] On the other hand, SML QDots are realized by a cycled deposition of submonolayer InAs surrounded by a GaAs matrix (usually 2-4ML). The surface distribution of InAs is initially extremely non-uniform forming InAs-rich islands [6]. However, after the GaAs overgrowth is deposited, the following InAs SML growth is impacted by the non-uniform strain caused by the underlying InAs islands and this leads to a vertical alignment of the SML InAs layers.[14]

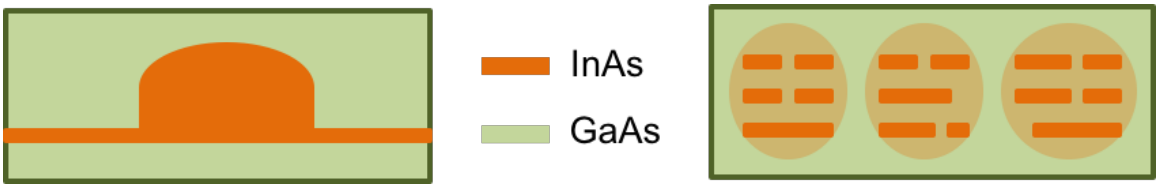

(a) (b)

Figure 5.1: Schematic illustrating the structural difference between SK QDots (with a distinct wetting layer) and a stack of SML QDots.

The structural and optical properties of InAs SML QDots have been well-researched and understood to a large extent. [14-17] For a nominal deposition of cycled 0.5ML InAs / 4ML of GaAs, one would expect InAs islands with monolayer heights separated by pure GaAs layers. However, it has been shown that a vertical segregation of InAs occurs during the capping of the islands by GaAs with a segregation co-efficient of ~0.73 (the segregation co-efficient is found to be fairly independent of the spacer thickness, suggesting a more general mechanism for the formation of SML QDots). This effectively produces agglomerations of InAs that are vertically connected throughout the entire stack. The agglomerations are found to have lateral widths of ~5nm and are separated by a 2nm spacing. With these lateral dimensions, the areal density of the SML QDots can be calculated to be in the 10 ^{12}cm^{-2} range. This is an extremely high areal density when compared to typical SK QDot densities of high 10^{10} to low 10^{11} cm^{-2}. The high areal density implies a higher fraction of the surface area covered by the QDots and this in turn leads to a high probability capture of charge carriers. Unlike SK QDots, submonolayer QDots do not exhibit a wetting layer and this aids high-speed relaxation of carriers as they have to relax directly into the QDots. [15] The PL emission from SML QDots shows narrow linewidths well below 10meV which is extraordinarily lower than linewidths for emission from SK QDots and is more typical for QW emission. Compared to QWs with equivalent InAs composition and thickness, the emission from SML QDots is redshifted and can be well-fitted with a model for rough quantum wells. Consequentially, it has been shown that the excitonic emission from SML QDots is a result of mixed contribution of zero-dimensional (due to InAs-rich islands) and 2-dimensional quantum well (due to the strong lateral coupling) states. [14]

5.3 Epitaxial growth process for SML QDot-based SESAMs

The initial growth details for the QDot samples (substrate preparation, oxide desorption and smoothing layers) are similar to the QW ones as described in Chapter 4. Before growing the SESAM wafers, PL calibration samples are grown to align the emission wavelength. For these samples, the absorber region consisting of nominal 0.5ML InAs / 2.3ML GaAs layers is grown at ~475^{0}C following the growth of the smoothing layer. The QDots are then capped with 1.5nm cold GaAs before the substrate temperature is raised back to 580^{0}C to grow the rest of the GaAs cap. The total GaAs cap thickness is kept at 7nm to be consistent with the QW samples. Different number of InAs/GaAs periods are attempted and the PL emission is measured. For the SESAM samples, the absorber region (along with the 7nm GaAs cap) is incorporated on top of a 29.5 pair AlAs/GaAs DBR with a 22nm GaAs spacer layer. The InAs/GaAs thicknesses are chosen to be 0.5/2.3ML as this combination has previously been used to realize a high power semiconductor disk laser with a lasing wavelength of ~1030nm [6]. The growth rates of In and Ga (calibrated by RHEED oscillations) were 0.03ML/sec and 0.3ML/sec respectively and a constant As:Ga BEP ratio of 13 is maintained.

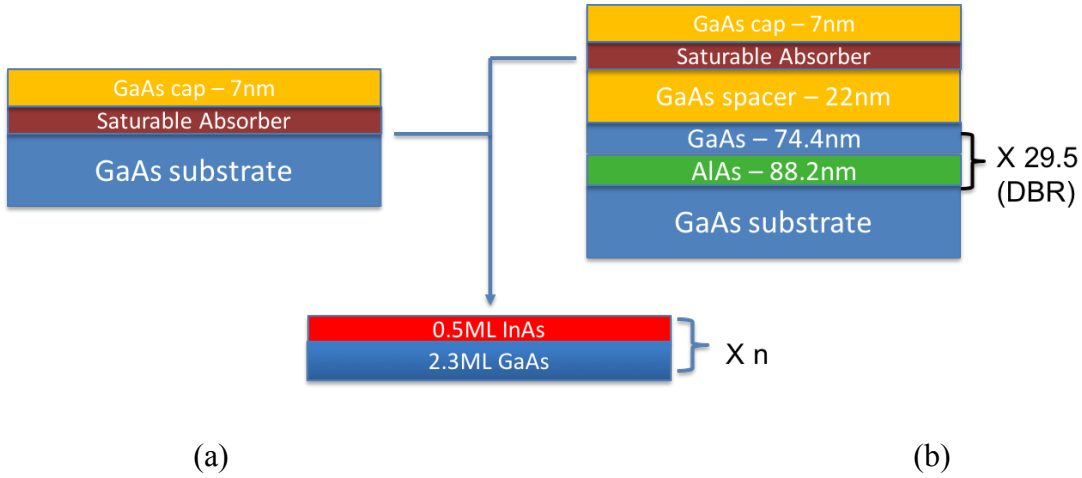

Figure 5.2 : Schematic illustrating the PL calibration (a) and SESAM (b) structures for SML QDot absorber

5.4 Alignment of SML QDot absorber wavelength using PL

Figure 5.3 shows room temperature PL spectra for InAs/GaAs SML QDots with 10,13 and 15 periods. As the number of stacks increases, the effective size of the SML QDot increases. This results in the observed redshift of the emission wavelength from 980nm (10 periods) to 1020nm (15 periods). This is analogous to increase in emission wavelength for SK QDots as the size of the QDot increases. [18-20] The increase in PL intensity with increasing number of periods can be attributed to a deeper confining potential. However, it is to be noted that the wavelength redshift and the increase in PL intensity is also accompanied by an increase in the FHWM of the PL emission. The FWHM increases from 20nm for 10 periods to 30nm for 15 InAs/GaAs periods. With a higher number of stacks, the probability of a wider distribution in QDot size is higher resulting in an increase in the FWHM of the PL peak. Based on these results, the number of stacks is chosen to be 15 for the SESAM samples. (n=15)

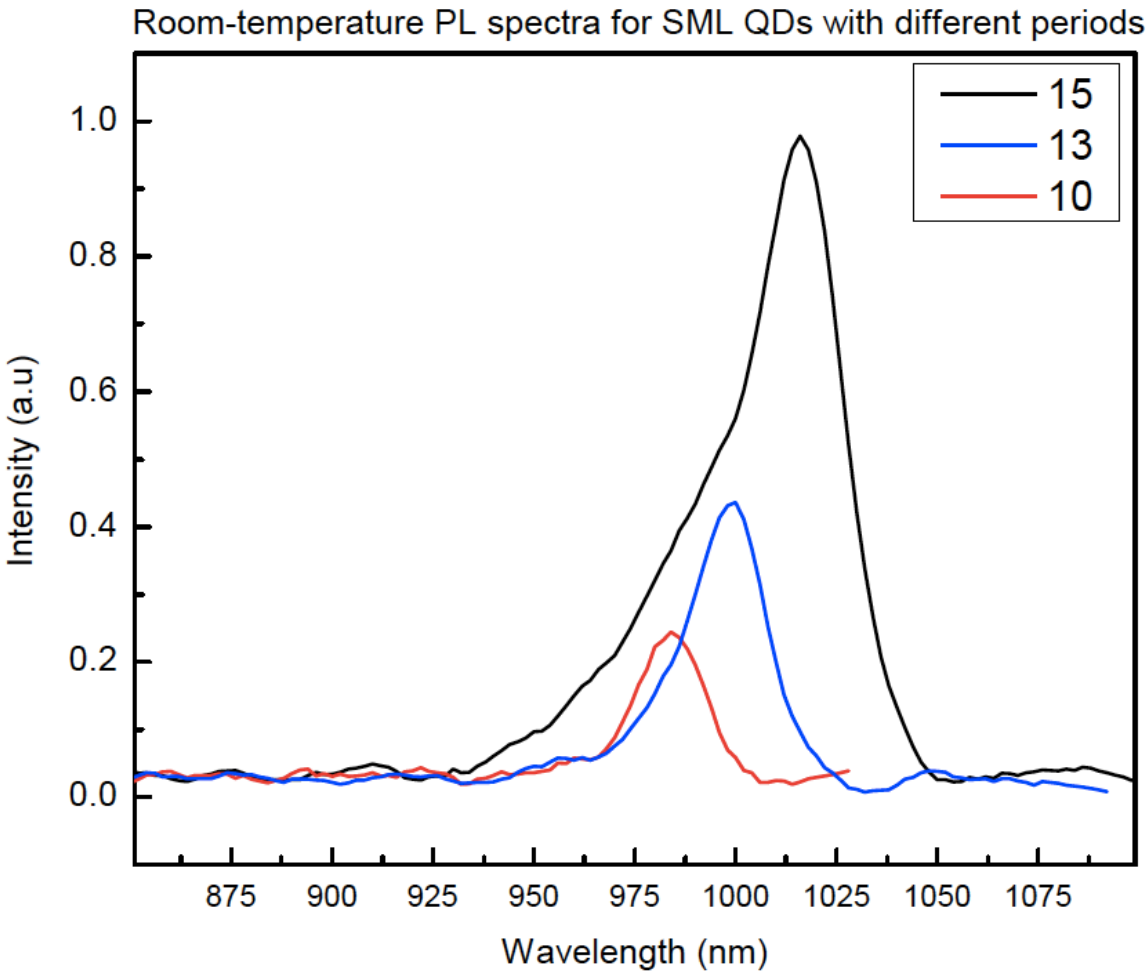

Figure 5.3 : Variation of PL emission wavelength with increasing number o stacks. The emission wavelength redshift is accompanied by an increase in PL intensity and FWHM.

5.5 Spectral reflectivity measurements

Based on the structure described in the previous section and using 15 SML QDot stacks, the SESAM is grown. With 15 periods of 0.5ML InAs/ 2.3ML GaAs, the total thickness of the absorber is ~11nm, as opposed to an absorber thickness of ~8nm with the InGaAs QWs. Therefore, the GaAs spacer between the 29.5 pair DBR and the absorber is modified (22nm to 19nm) accordingly to keep the placement of the absorber with respect to

the field antinode consistent between the QW and QDot SESAMs. Figure 5.4 shows the room-temperature reflectivity spectrum for the SML QDot SESAMs.

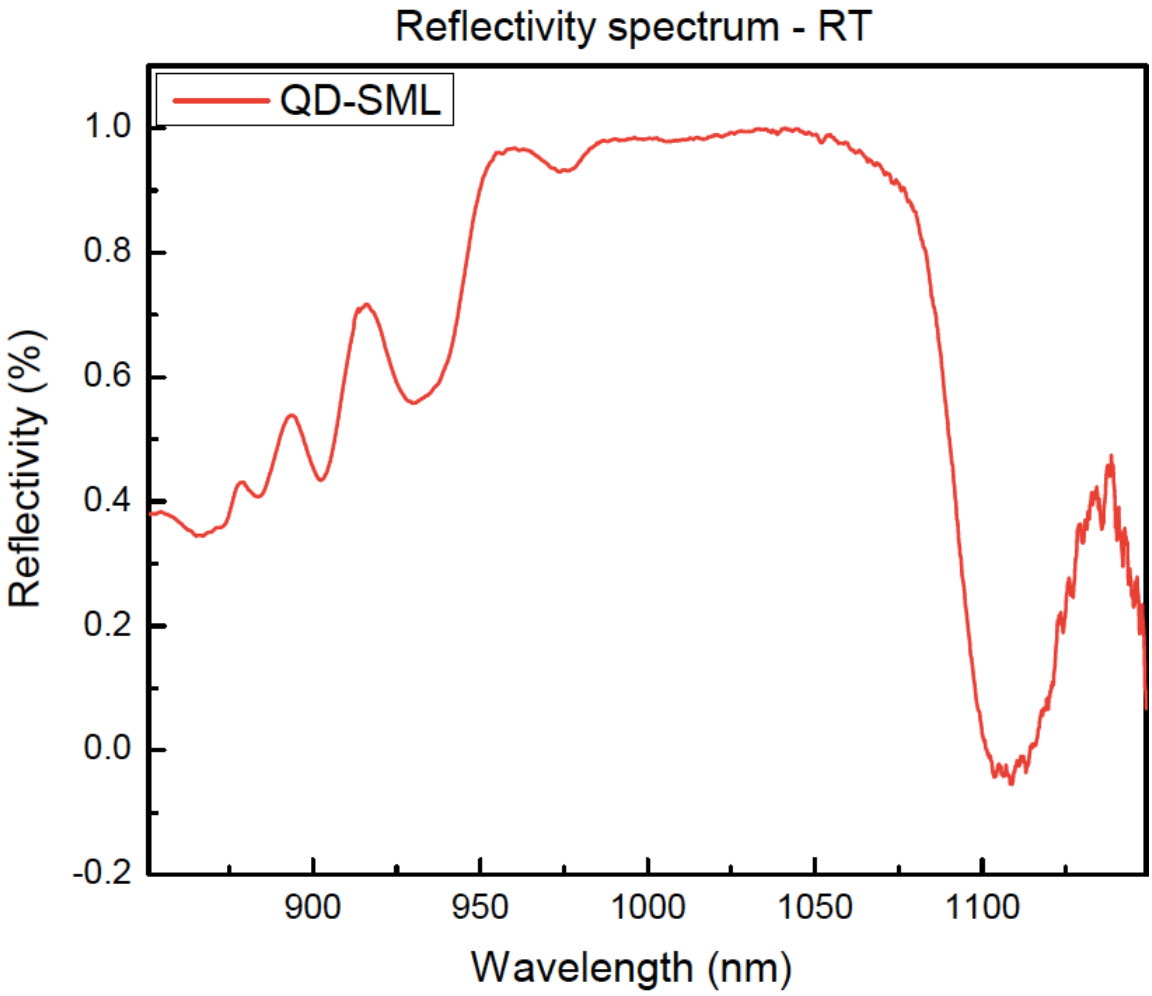

Figure 5.4 : Room-temperature reflectivity measurements for the SML QDot SESAM. The stopband is centered at ~1030nm.

The DBR stopband extends from ~980nm to 1110nm and is centered at 1030nm. The skewed oscillations on the lower wavelength side and the dip in reflectivity at ~975nm can be attributed to a drift in the Ga or Al growth rate. As explained in Chapter 4, this is a result of slowly decreasing growth rates over the growth of the DBR region. In addition to

the alignment of the DBR stopband, it is critical to align the absorption wavelength of the QDot. The reflectivity spectrum shown above in figure is magnified around ~1020nm to be able to observe the absorption from the SML QDot absorber on the stopband.

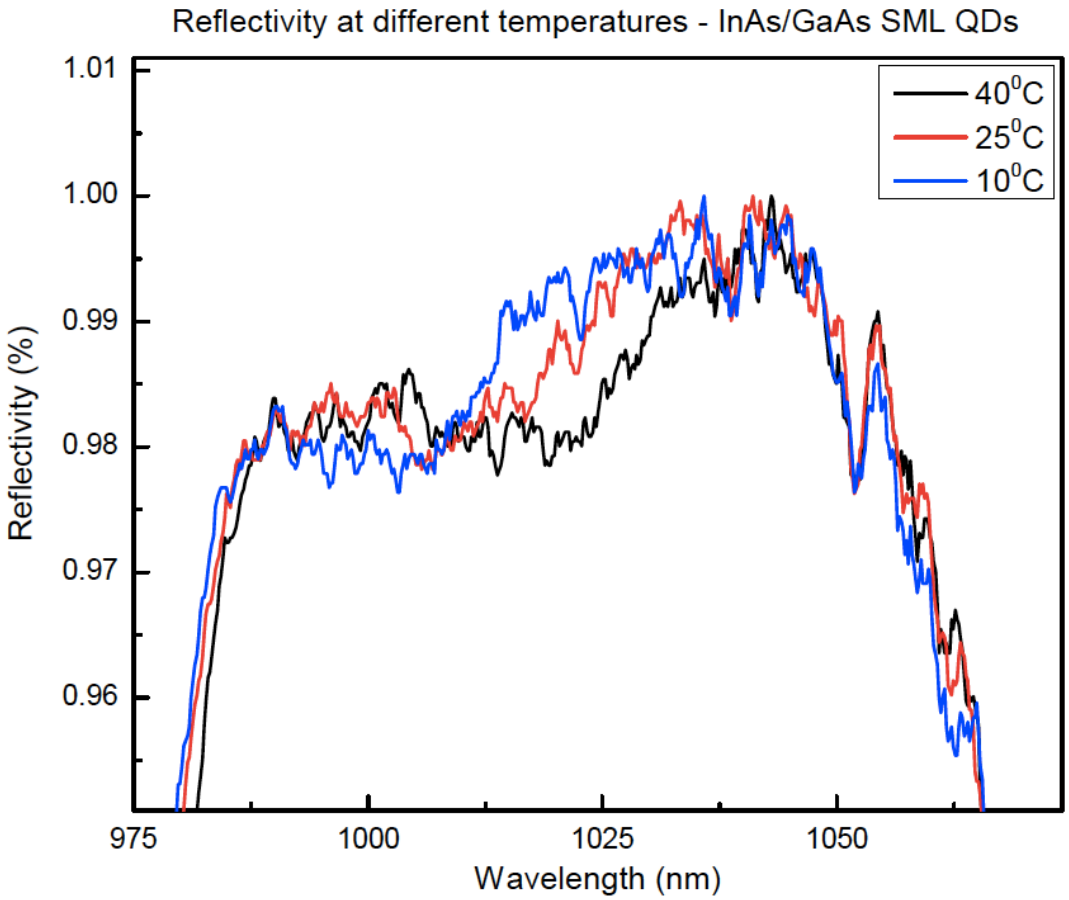

Figure 5.5 : Fig: A magnified view of the room-temperature reflectivity measurements on the SML QDot SESAM. The dip in reflectivity around 1020nm is caused by absorption from the SML QDot layer and it redshifts slowly with an increase in temperature.

Figure above shows the magnified reflectivity spectra from the SML QDot SESAM measured at different temperatures. The absorption from the SML QDots can be observed as a dip in reflectivity. As the temperature increases, the absorption moves to longer

wavelengths in accordance with the emission wavelength shift of the QDots. However, as expected, the InAs SML QDots are more temperature-stable when compared to the QWs. The shift in the absorption as a function of temperature can be calculated to be 0.1nm/^{0}C (lower compared to 0.303nm/^{0}C for the InGaAs QWs). In addition to the shift in the absorption, a redshift in the DBR stopband is observed. This redshift can be attributed to the slight variation of the refractive indices of the materials comprising the DBR (GaAs and AlAs). Based on the reflectivity spectra, the anti-reflection coating (TaO_2) is designed and deposited as described in the previous chapters. The results discussed from this point onwards for the rest of this chapter refer to coated QDot SESAMs

5.6 Recovery time measurements

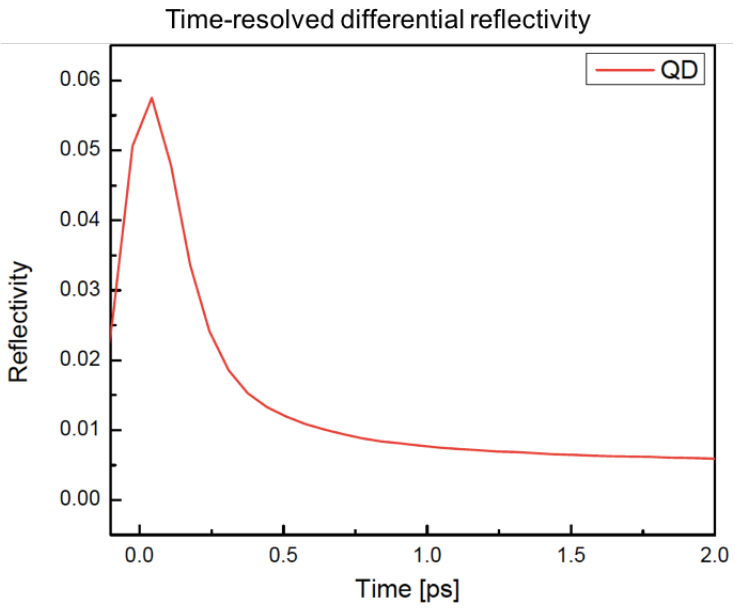

Figure 5.6 : Time-resolved differential reflectivity measurements for SML QDot-based SESAMs.

Figure 5.6 above shows the recovery times for QDot-based SESAMs measured using a pump probe setup. As seen with the QWs, the QD SESAMs clearly show (as seen in figure above) two distinguishable recovery processes – a fast component which causes a sudden drop in reflectivity followed by a slow component (setting in at ~200fs). The pump probe response can be fitted well with two time constants:

$$\Delta R_{pp}(\tau) = Ae^{\frac{-\tau}{\tau_{slow}}} + (1 - A)e^{\frac{-\tau}{\tau_{fast}}} \qquad (5.1)$$

The two time constants deduced from the fit are in table 5.1

Time constant (τ)	(fs)
$\boldsymbol{\tau}_{\text{fast}}$	120
$\boldsymbol{\tau}_{\text{slow}}$	1.75ps

Table 5.1: Fast and slow components of the recovery time for QDot-based SESAMs

Both time constants measured are lower than recovery times measured for QW samples (refer to table 3.2). The fast component of the recovery is suspected to be due to absorption bleaching of the photocarriers followed by intradot or interdot transition. The ultrahigh density of the SML QDots is advantageous here as the high density of QDots leads to a higher probability of higher interdot transfer. The slow component of the recovery time is due to recombination of carriers back to the ground state.

5.7 GDD measurements:

The GDD for the QDot SESAM around the wavelength of interest (1030nm) is measured before further device testing. The anti-reflection coating reduces the cavity enhancement and flattens the GDD profile as expected. As the figure shows, the GDD is relatively flat between 1020-1030nm and stays positive.

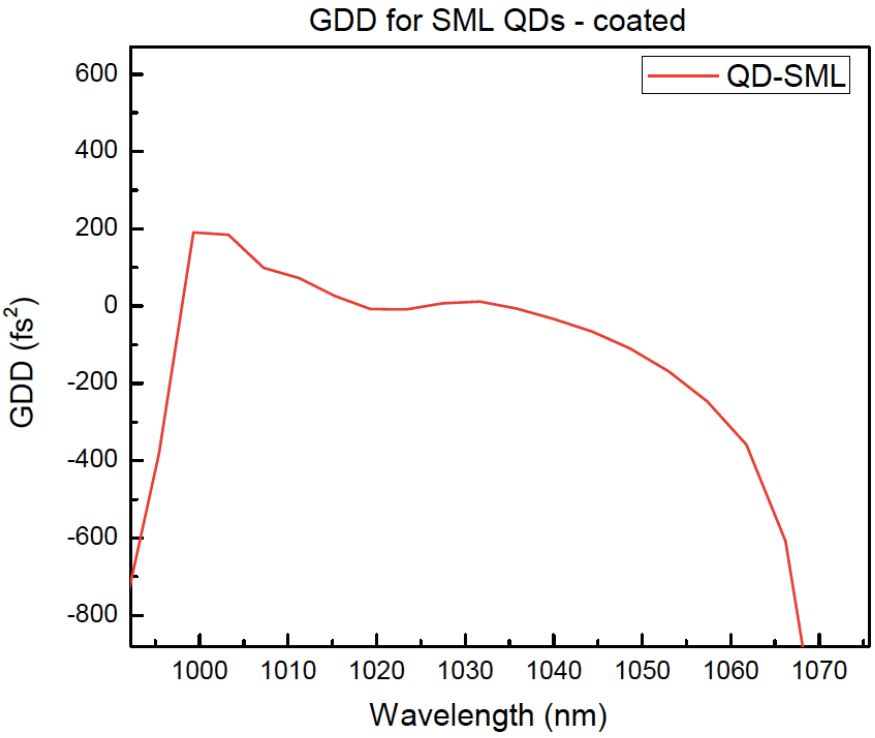

Figure 5.7 : GDD measurements for the SML QDot-based SESAM. It is relatively flat around 1030nm and is on the positive side.

5.8 Degradation of SML QD-based SESAMs

Before attempting to mode-lock using the QDot SESAM, the damage threshold of the SESAM is measured. Since the effect of the anti-reflection coating has been measured with the QW SESAMs, all studies on QDot SESAMs are carried out only on coated devices.

The results are shown in figures 5.8. Unlike the QW SESAMs (compared further in chapter), there is no significant damage to the QDot SESAM observed until the incident average power is 90mW (peak power - 112MW/cm^2). In the PL spectra shown below, the emission peak of interest is the one positioned at ~1020nm. As in QW SESAMs, the other peaks observed in the spectra can be attributed to cavity effects. The PL emission is measured at the end of each minute of SESAM exposure to the incident laser. As shown in the figure below, even at high incident power, the PL degradation is minimal for the QDot SESAMs. It is also important to note that the FWHM of the emission (peak at 1020nm considered) stays constant throughout the measurement even with an associated decrease in PL intensity.

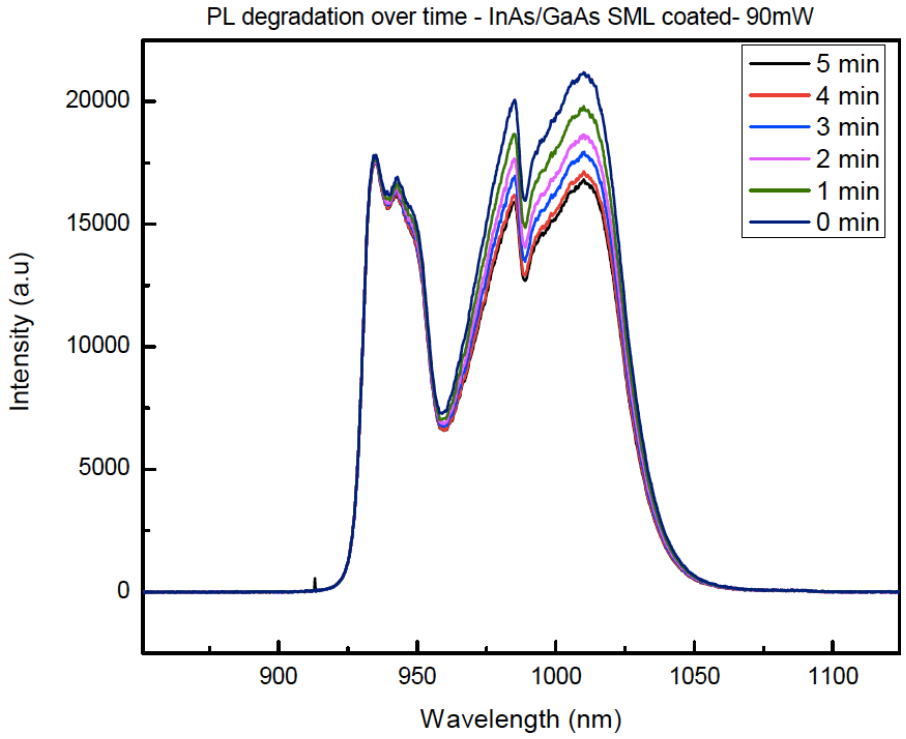

Figure 5.8 : Variation of PL emission over time when QDot SESAM is exposed to a modelocked femtosecond laser @ 780nm. The degradation over a period of 5 min is minimal when compared to the QW SESAMs.

To quantify the degradation in PL, the peak PL intensity is also tracked over the 5 minute-measurement and is shown in figure 5.9. The peak intensities for each spectrum are normalized to the peak intensity at the beginning of the measurement (t=0 min) and it is found that over a 5 min period, the peak intensity decreases by ~18%. This indicates that SESAMs with QDot absorbers have a higher damage threshold when compared to QW SESAMs. (PL peak intensity decreased by over 50%) The following section focuses on a comparison between the QW and QDot-based SESAMs with regards to damage threshold.

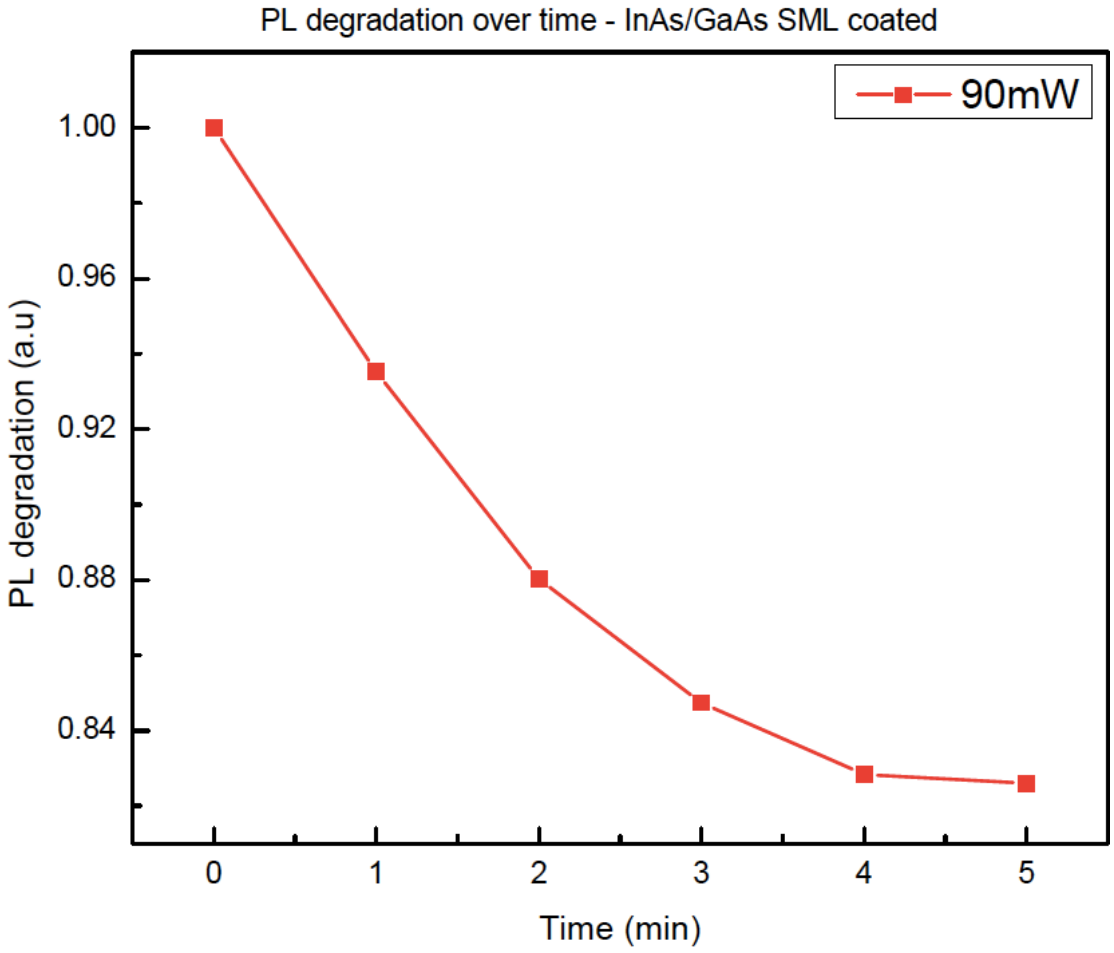

Figure 5.9 : Variation of PL peak intensity at the end of each minute over a 5 min period for a QDot SESAM. The peak intensity decreases by ~18%.

5.9 Mode-locking results

With the different parameters for the SESAM (recovery time, GDD, reflectivity) verified to be able to support ultra-short pulses and the recovery time found to be lower than QWs, we attempted mode-locking the QDot-based SESAM in a ring cavity. A minimum pulse duration of 185fs was obtained with the gain element at 25^0C and the SESAM chip at 40^0C. Figure 5.10 shows the non-collinear SHG autocorrelation trace of the output fitted to a 185fs $sech^2$ pulse shape. To the best of our knowledge, this is the first reported mode-locking result for a SML QDot absorber SESAM at 1030nm.

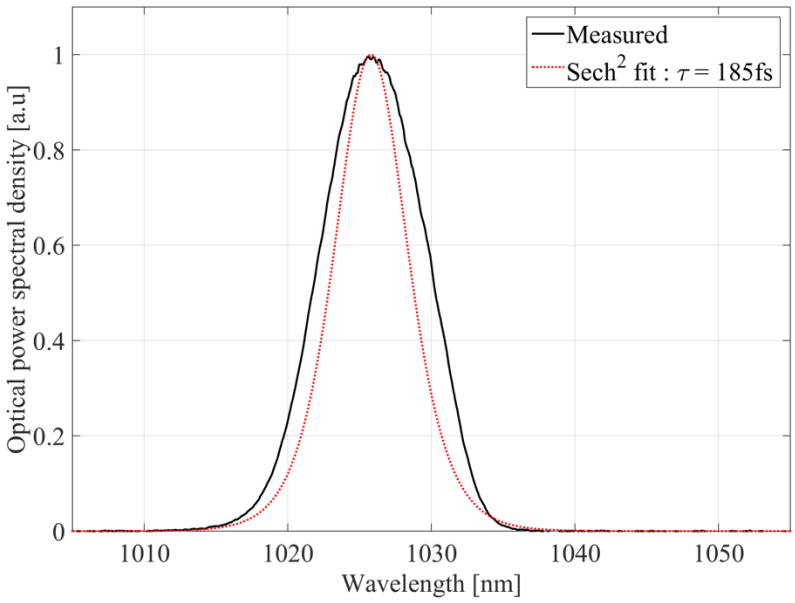

Figure 5.10 : SHG autocorrelation trace of the output of the cavity fitted to a sech2 pulse shape. Pulses as short as 185fs are obtained

5.10 Degradation of SML QDot-based SESAMs vs QW SESAMs

Figure 5.11 shows PL spectra measured for InGaAs QW and InAs/GaAs SML QDot-based SESAMs. As mentioned before, the emission peak of interest is at ~1020nm for both

spectra and the additional peaks can be attributed to cavity effects. However, compared to the QW spectrum, the QDot SESAM shows an extra peak at ~985nm. Referring to reflectivity measurements for the QDot SESAM (shown in one of the earlier sections of this chapter), this PL peak corresponds with a dip in reflectivity of the DBR which is suspected to be caused by a drift in growth rates. It is found that the PL intensity for the QW is ~40% less then the QDot SESAM under similar conditions. This increased emission from the QDots compared to the QWs can be explained based on the difference in the density of states for the zero-dimensional QDots. This also indicates that the SML QDot SESAMs are expected to have substantially lower saturation fluences when compared to the QW SESAMs.

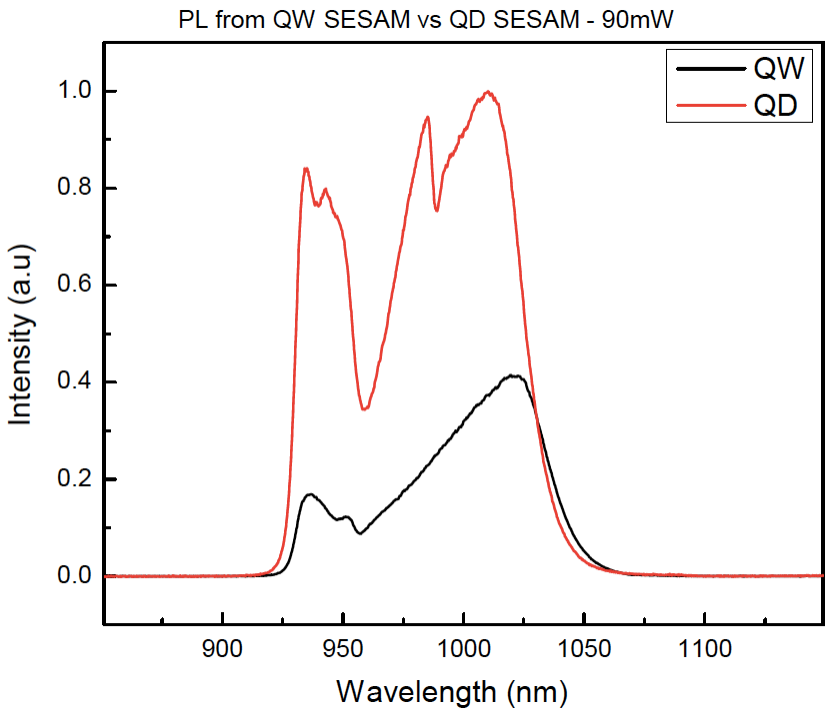

Figure 5.11 : PL spectra for QW and QD-based SESAMs. The QD SESAMs have a higher peak intensity when compared to the QW-based SESAMs.

The decay in the PL peak intensity at 1min intervals over a 5 min period is compared for QW and QDot SESAMs in figure 5.12. While the QW SESAMs show a PL decay of ~65%, the QDot-based SESAM decays only by ~18%. Therefore, it is apparent that the damage threshold for the QDot SESAM is substantially higher when compared to the QW SESAM. This higher threshold is a direct result of the lower saturation fluence and shorter relaxation time for the QDot-based SESAMs.

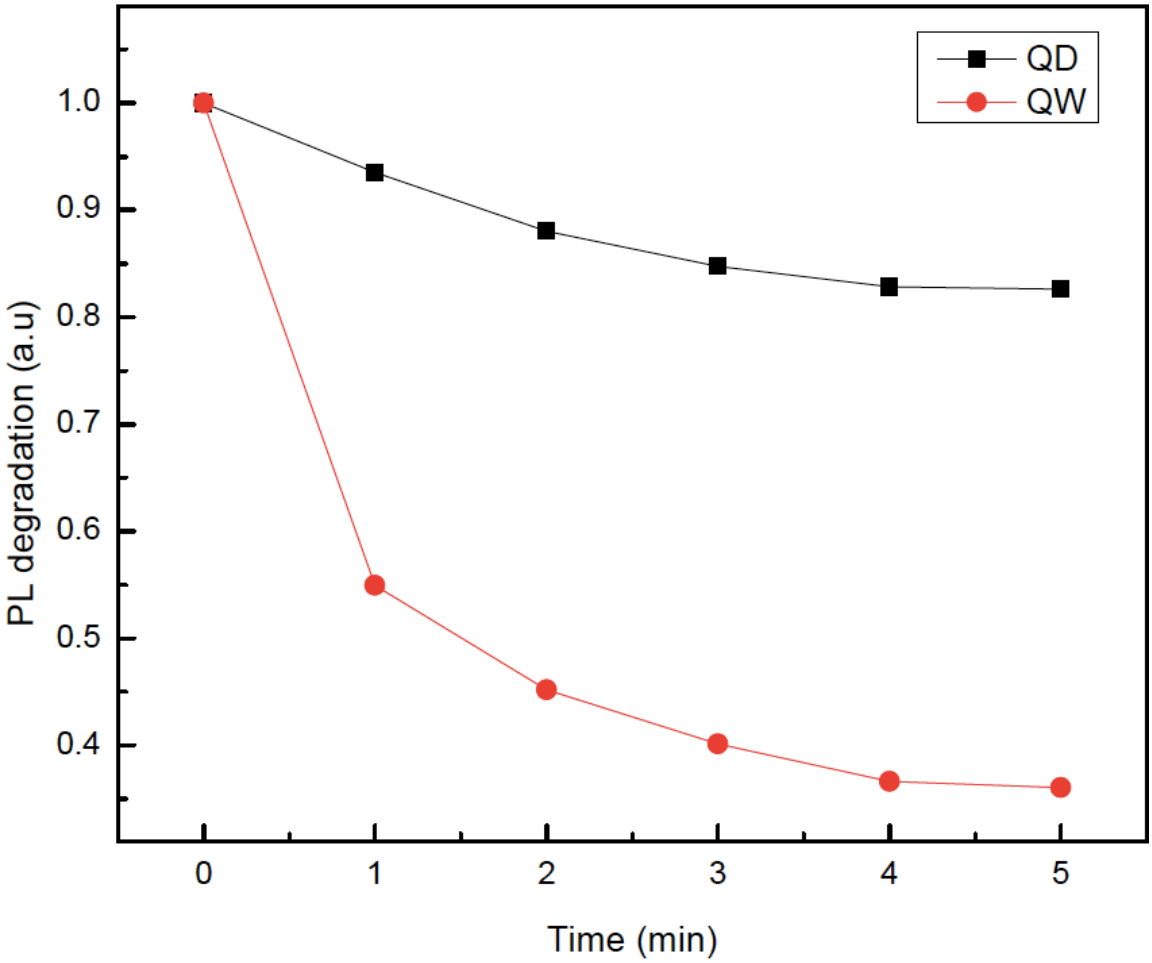

Figure 5.12 : Variation of PL peak intensity at the end of each minute over a 5 min period for a QW SESAM vs QDot-based SESAM. The peak intensity decay is more pronounced for the QW-based SESAM, thus indicating a higher damage threshold for the QDot SESAMs.

5.11 Stability in mode-locking state over time (SML QDots vs QWs)

Figure 5.13 shows mode-locking stability data for QW and QDot-based SESAMs in a symmetric ring cavity. At the outset, it is apparent that the QDot-based SESAMs have a longer lifetime than the QW-based SESAMs. The QW SESAM (shown in red) shows an initial degradation rate of 6.5% which reduces eventually to 0.8% after 10min. On the other hand, the SML QDot SESAM only shows an initial degradation of 1.4% which drops to 0.2% after 10 min and the effective lifetime is substantially longer for the QDot-based SESAM. This increase in modelocking lifetime for QDot-based SESAMs compared to QW-based SESAMs can be explained based on two different factors: the increase in effective cap thickness and the difference in macroscopic properties. The thickness of the QDot-based absorber region (12nm) is thicker than the InGaAs QW(8nm). This means that the effective separation between the AlAs layer and the air-semiconductor interface increases and this could be leading to the increase in SESAM lifetime. On the other hand, the macroscopic properties of the QDot-based SESAMs are different compared to the QW-based SESAMS. For instance, the recovery time components are both smaller with the QDot-based SESAMs and we suspect that this could be contributing towards the increase in SESAM lifetime.

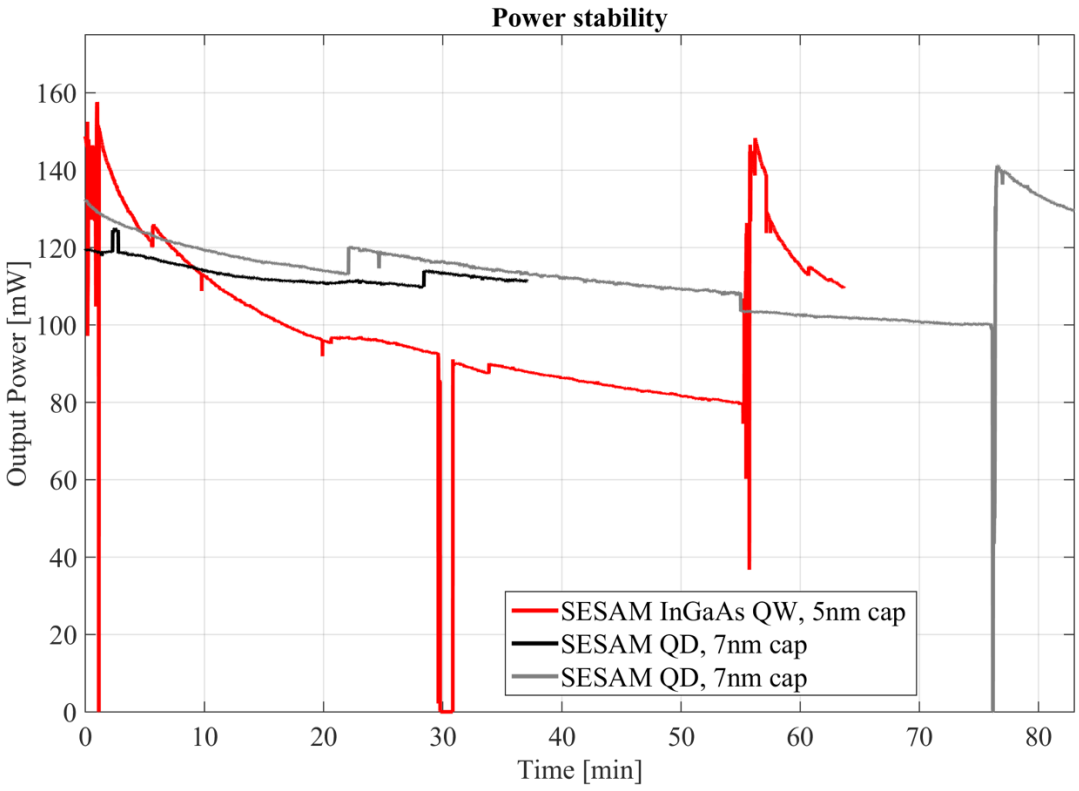

Figure 5.13 : Output power stability in a mode-locked state compared between QW and QDot-based SESAM.

References:

[1] Bellancourt, Aude-Reine, Yohan Barbarin, Deran JHC Maas, Mohammad Shafiei, Martin Hoffmann, Matthias Golling, Thomas Südmeyer, and Ursula Keller. "Low saturation fluence antiresonant quantum dot SESAMs for MIXSEL integration." *Optics express* 17, no. 12 (2009): 9704-9711.

[2] Maas, D. J. H. C., A-R. Bellancourt, M. Hoffmann, B. Rudin, Y. Barbarin, M. Golling, T. Südmeyer, and U. Keller. "Growth parameter optimization for fast quantum dot SESAMs." *Optics express* 16, no. 23 (2008): 18646-18656.

[3] McWilliam, Alan, A. A. Lagatsky, C. T. A. Brown, W. Sibbett, A. E. Zhukov, V. M. Ustinov, A. P. Vasil'Ev, and E. U. Rafailov. "Quantum-dot-based saturable absorber for femtosecond mode-locked operation of a solid-state laser." *Optics letters* 31, no. 10 (2006): 1444-1446.

[4] Ledentsov, Nikolai N., Dieter Bimberg, and Zh I. Alferov. "Progress in epitaxial growth and performance of quantum dot and quantum wire lasers." *Journal of lightwave technology* 26, no. 11 (2008): 1540-1555.

[5] Zhukov, A. E., A. R. Kovsh, S. S. Mikhrin, N. A. Maleev, V. M. Ustinov, D. A. Livshits, I. S. Tarasov et al. "3.9 W CW power from sub-monolayer quantum dot diode laser." *Electronics Letters* 35, no. 21 (1999): 1845-1847.

[6] Germann, T. D., A. Strittmatter, J. Pohl, U. W. Pohl, D. Bimberg, J. Rautiainen, M. Guina, and O. G. Okhotnikov. "High-power semiconductor disk laser based on In As⁄ Ga As submonolayer quantum dots." *Applied Physics Letters* 92, no. 10 (2008): 101123.

[7] Hopfer, F., A. Mutig, M. Kuntz, G. Fiol, D. Bimberg, N. N. Ledentsov, V. A. Shchukin et al. "Single-mode submonolayer quantum-dot vertical-cavity surface-emitting lasers with high modulation bandwidth." *Applied physics letters* 89, no. 14 (2006): 141106.

[8] Herzog, Bastian, Nina Owschimikow, Jan-Hindrik Schulze, Ricardo Rosales, Yücel Kaptan, Mirco Kolarczik, Thomas Switaiski et al. "Fast gain and phase recovery of semiconductor optical amplifiers based on submonolayer quantum dots." *Applied Physics Letters* 107, no. 20 (2015): 201102.

[9] Ledentsov, N. N., A. F. Tsatsul'nikov, A. Yu Egorov, P. S. Kop'ev, A. R. Kovsh, M. V. Maximov, V. M. Ustinov et al. "Intrinsic optical confinement and lasing in InAs–AlGaAs submonolayer superlattices." *Applied physics letters* 74, no. 2 (1999): 161-163.

[10] Ting, David Z-Y., Sumith V. Bandara, Sarath D. Gunapala, Jason M. Mumolo, Sam A. Keo, Cory J. Hill, John K. Liu, Edward R. Blazejewski, Sir B. Rafol, and Yia-Chung

Chang. "Submonolayer quantum dot infrared photodetector." *Applied Physics Letters* 94, no. 11 (2009): 111107.

[11] Mikhrin, S. S., A. E. Zhukov, A. R. Kovsh, N. A. Maleev, V. M. Ustinov, Yu M. Shernyakov, I. P. Soshnikov et al. "0.94 μm diode lasers based on Stranski-Krastanow and sub-monolayer quantum dots." *Semiconductor science and technology* 15, no. 11 (2000): 1061.

[12] Lam, Phu, Jiang Wu, Mingchu Tang, Qi Jiang, Sabina Hatch, Richard Beanland, James Wilson, Rebecca Allison, and Huiyun Liu. "Submonolayer InGaAs/GaAs quantum dot solar cells." *Solar Energy Materials and Solar Cells* 126 (2014): 83-87.

[13] Shchukin, Vitaliy A., and Dieter Bimberg. "Spontaneous ordering of nanostructures on crystal surfaces." *Reviews of Modern Physics* 71, no. 4 (1999): 1125.

[14] Lenz, Andrea, Holger Eisele, Jonas Becker, Jan-Hindrik Schulze, Tim D. Germann, Franziska Luckert, Konstantin Pötschke et al. "Atomic structure and optical properties of InAs submonolayer depositions in GaAs." *Journal of Vacuum Science & Technology B, Nanotechnology and Microelectronics: Materials, Processing, Measurement, and Phenomena* 29, no. 4 (2011): 04D104.

[15] Lenz, Andrea, Holger Eisele, Jonas Becker, Lena Ivanova, Ernst Lenz, Franziska Luckert, Konstantin Pötschke et al. "Atomic Structure of Buried InAs Sub-Monolayer Depositions in GaAs." *Applied physics express* 3, no. 10 (2010): 105602.

[16] Brandt, O., H. Lage, G. C. La Rocca, A. Heberle, and K. Ploog. "Role of broken translational invariance for the optical response of excitons in low-dimensional semiconductors." *Surface science* 267, no. 1-3 (1992): 319-322.

[17] Bimberg, Dieter, Marius Grundmann, and Nikolai N. Ledentsov. *Quantum dot heterostructures*. John Wiley & Sons, 1999.

[18] Murray, Ray, David Childs, Surama Malik, Philip Siverns, Christine Roberts, Jean-Michel Hartmann, and Paul Stavrinou. "1.3 μm room temperature emission from InAs/GaAs self-assembled quantum dots." *Japanese journal of applied physics* 38, no. 1S (1999): 528.

[19] Schmidt, K. H., Gilberto Medeiros-Ribeiro, J. Garcia, and Pierre M. Petroff. "Size quantization effects in InAs self-assembled quantum dots." *Applied physics letters* 70, no. 13 (1997): 1727-1729.

[20] Fuster, David, Luisa González, Yolanda González, María Ujué González, and Juan Martínez-Pastor. "Size and emission wavelength control of In As⁄ In P quantum wires." *Journal of applied physics* 98, no. 3 (2005): 033502.

Chapter 6 : Conclusions

Mode-locked VECSEL systems using SESAMs have proven to be a worthy alternative to state-of-the-art solid-state ultrafast lasers. In this dissertation, we have developed epitaxial strategies to realize a mode-locked VECSEL system using QW or QDot-based SESAM that is capable of supporting ultra-short (~100fs) pulses. In particular, we have focused on optimizing growth strategies for the SESAM, using a standard VECSEL structure.

We first investigated design considerations for both the gain chip and the SESAM. This included designing the active region, the DBR for both gain and SESAM and the absorber region for the SESAM. Based on design considerations, a standard gain chip containing 12 InGaAs QWs non-uniformly distributed at the standing electric field antinodes is grown. For the SESAM, we decided to use GaAs/AlAs DBRs with a single InGaAs QW forming the absorber region at a design wavelength of 1030nm.

For the growth of the SESAM, we independently optimized the growth of the DBR and the absorber. In order to be able to grow the DBR region with the stop-band aligned at the laser emission wavelength, we had to overcome two main challenges with regard to growth rate stability: over time and over the wafer area. We were able to achieve this by making minor modifications to the Al effusion cell in our reactor. The growth of the absorber is optimized based on PL. Finally, the growth process for the SESAM as a whole is optimized based on a number of macroscopic SESAM parameters: GDD, reflectivity and

recovery time. After going through a few iterations of optimizing the growth process to obtain optimum SESAM characteristics, we were able to realize InGaAs QW-based SESAMs that could be used to mode-lock a VECSEL in a ring cavity. Pulse durations as short as 128fs with an output power of up to 90mW were realized.

Using the InGaAs QW-based SESAM, we were able to achieve mode-locking with one of the shortest pulse durations reported in literature. However, we also found that these SESAMs exhibit poor temporal stability with very low effective mode-locking lifetimes. TPA is recognized to be the damage mechanism which causes a decay in output power over time. In order to observe the physical damage caused by TPA, we also conducted a thorough TEM analysis of the damaged SESAM compared to an "as-grown" SESAM. Through the TEM study, we were able to conclude that the SESAM damage is mainly caused by the oxidation of the AlAs layer in the DBR. The damage profile resembles the profile of a laser beam-induced damage with the top of the DBR being more affected than the bottom. We also studied the effect of various SESAM parameters such as cap thickness, presence of AR coating and incident fluence on the damage threshold of the SESAM. From these experiments, it was found that the damage in the DBR region seems to be extremely sensitive to the field intensity of the standing electric field. In order to alleviate the damage mechanism of the SESAMs, we explored the use of QDot-based absorbers.

For the QDot-based SESAMs, we decided to use InAs/GaAs SML QDot regions instead of SK QDots as they are more suitable for the design wavelength. The DBR region is kept the same between the two systems. As in the case of QWs, the growth of the absorber

region is aligned based on the number of periods of SML QDots using PL. Again, the SESAMs are optimized based on their macroscopic parameters. When introduced into a cavity we were able to achieve mode-locking with pulses as short as 185 fs. Also, the lifetime of the QDot-based SESAMs were increased by a factor of ~3.

Summarizing, in the first part of this thesis we were able to realize an InGaAs QW-based SESAM which could mode-lock a VECSEL with one of the shortest pulse durations reported. However, the lifetimes of the QW-based SESAMs were found to be poor in the femtosecond regime. To alleviate this, we explored the use of QDot-based SESAMs with lower recovery times compared to QW SESAMs and were successfully able to extend the lifetime of the mode-locking state.